

ISSN 1450-7404

Journal of Research in Physics

Volume 29
Number 1
2002



INSTITUTE OF PHYSICS

Faculty of Sciences
University of Novi Sad - Novi Sad - Yugoslavia

Journal of Research in Physics

Editor
Mario Škrinjar

Editor-in-Chief
Ištvan Bikit

INTERNATIONAL EDITORIAL BOARD

Lajos Bata
Research Institute for
Solid State Physics
Budapest, Hungary

Nikos Flytzanis
Physics Department
University of Crete
Iraklion, Greece

Kazuo Tanaka
Institute of Laser
Engineering
Osaka, Japan

Emilio Marquez Navarro
Departamento de Física
de la Materia Condensada
Universidad de Cadiz
Cadiz, Spain

Padma Shukla
Ruhr - Universität Bochum
Bochum, Germany

Stevica Djurović
Svetlana Lukić
Zoran Mijatović
Jaroslav Slivka
Jovan Šetrajić
Department of Physics
University of Novi Sad
Novi Sad
Serbia

Ivan Aničin
Jaroslav Labat
Jagoš Purić
Physical Faculty
University of Belgrade
Belgrade
Serbia

Milan Dimitrijević
Astronomical Observatory
Belgrade
Serbia

Zoran Popović
Institute of Physics
Belgrade
Serbia

Published by: Department of Physics, Faculty of Sciences, University of Novi Sad,
Trg Dositeja Obradovića 4, 21000 Novi Sad, Serbia

Phone: +381-21-455318

Fax: +381-21-459367
<http://www.if.ns.ac.yu>

E-mail: fizika@uns.ns.ac.yu

The ($0\nu + 2\nu$) Double Beta Decay of ^{50}Cr

N. Žikić-Todorović, I. Bikit, J. Slivka, M. Vesković, M. Krmar and Lj. Čonkić
*Institute of Physics, Faculty of Sciences and Mathematics, University of Novi Sad,
Trg Dositeja Obradovića 4, 21000 Novi Sad, Yugoslavia*

Received: March 9, 1998

Abstract

The coincidence measurements of annihilation radiation from a sample of CrO_3 containing 4.72 g of ^{50}Cr were performed using a horizontal HPGe detector shielded by a NaI annulus with a NaI plug. The whole setup was within a heavy iron shielding. The signature of both the two neutrino and the neutrinoless positron-electron capture decay of ^{50}Cr is considered to be the 511–511 keV coincidence from the HPGe detector and the NaI plug, with no signal from the NaI annulus. No such events were observed during the twelve days measurement which yields an upper limit for the half-life of ^{50}Cr against the positron-electron capture decay of $2.6 \cdot 10^{18}$ y (at the 68% CL), what is an order of magnitude improvement over existing results.

Key words: Double-beta decay, low-level gamma spectroscopy

1. Introduction

Unanswered questions on the properties of the neutrino and the nature of weak interaction are strongly related to the existence of the 0ν double beta decay.

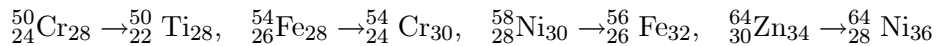
While the most experimental efforts have been cast on the double - β^- decays, the β^+ side is also important. Since the electron capture (EC) and the positron emission (β^+) are possible in a single - GT^+ transition, there are three cases in the double - GT^+ transitions; EC/EC, β^+/EC and $\beta^+\beta^+$ [1]. It has been pointed out that, in the 0ν mode, they seem to yield quite a different constraint on the neutrino masses and right-handed weak-current parameters, although the double - GT^+ transitions are more difficult to be observed than the double - β^- cases [2].

Because of the possible implications for lepton-number conservation and the mass of the neutrino, it is important to search for evidence of the β^+/EC decay. If a β^+/EC decay occurred within a thick sample of material, almost all of the positrons would stop and annihilate within the sample. Subsequently, either two or four strongly correlated coincident 511-keV annihilation gamma rays would be emitted and carry off the full decay energy. The comparatively low-energy x-rays that would also be emitted in the process of β^+/EC decay would be severely attenuated in the sample [3].

Double beta decay is the slowest nuclear transmutation observed. The experimental half-lives are $10^{19} - 10^{21}$ years. The detection of such a rare process demands extreme

care in the suppression of all possible forms of background. The first consequence is that no direct detection of $\beta\beta$ decay is possible on nuclei that are not stable with respect to other types of decay. This restricts the list of $\beta\beta$ candidates to those even-even nuclei in which the pairing interaction forbids the single β decay. In all candidates, both the parent and the daughter nuclei have a 0^+ ground state [4]. The 0ν decay mode as well as the 2ν one is strongly influenced by the generally not well-known nuclear matrix element. Therefore, experimental data on 0ν and 2ν mode half-lives on a large number of nuclides are needed.

Some time ago we started a systematic study of four double positron beta decay involving nuclei around the magic number 28, either as parents or as daughters. These four cases are:



The first of the decay is seen to complete the $N=28$ magic number, the second one destroys the $N=28$ magic number, the third destroys the $Z=28$ magic number while the fourth one completes the $Z=28$ magic number. It is to be expected that the decay which completes this magic number should be enhanced as compared to those which destroy it. Up to now we measured the second [5-7] and the fourth [8] of these cases and the hint that it indeed may be so came from the case of ${}^{64}\text{Zn}$ which gave the non-zero result, suggesting a strong structure effect. The case of the positron-electron capture double beta decay of ${}^{50}\text{Cr}$ should be similar in this respect, though the sensitivity of existing measurements of this decay [5] is by far too low to check this conjecture. We thus set to measure this decay again aiming at raising the sensitivity and eventually resolving this question.

2. Experimental details

Our previous study [9] of the electron-positron conversion decay of ${}^{64}\text{Zn}$ yielded a positive result for the $(0\nu + 2\nu)$ half-life; thus, we decided to measure the ${}^{50}\text{Cr}$ decay with a similar technique. The mass difference between the nuclei ${}^{50}\text{Cr}$ and ${}^{50}\text{Ti}$ $\Delta mc^2 = 1173.3(1.2)$ keV, (besides the (K,K) process which proceeded without positron emission) allows the β^+/EC decay with the transition energy of 144 keV. This value is more than two times bigger than the ${}^{64}\text{Zn}$ transition energy, enhancing thus the right-handed interaction amplitude contribution to the probability of the 0ν decay mode. The ${}^{50}\text{Cr}$ transition energy is far from the 1554 keV energy of the first excited state of ${}^{50}\text{Ti}$, so the β^+/EC decay can lead only to the ${}^{50}\text{Ti}$ ground state. The abundance of ${}^{50}\text{Cr}$ in natural Cr is 4.345% [10]. The enhancement of this decay might be due to the fact that the daughter nucleus here is a Z magic one.

We measured the number 511 keV γ -rays from positron annihilation in CrO_3 , aiming to investigate the $(0\nu + 2\nu)$ half-life. An event of possible interest was defined to be one for which there were coincident signals in the two inner detectors (HPGe and NaI(Tl) plug) and no signals in the annular shield.

In the experiment, the cylindrical samples with the diameter of $\phi = 70$ mm and thickness of $h = 25$ mm were sandwiched between a $7.6 \text{ cm} \times 7.6 \text{ cm}$ NaI(Tl) and a 25% efficiency HPGe detector. The CrO_3 sample contained 4.72 g of ${}^{50}\text{Cr}$. The positron creation in the sample from cosmic and environmental γ -rays was simulated by Fe and Cu "blank" samples. The detectors were connected to a coincidence circuit, presented in Fig. 1. The 511 keV SCA window was set on the more stable HPGe spectrum, and the NaI(Tl) spectrum was accumulated in the MCA gated with coincident slow signals. Due

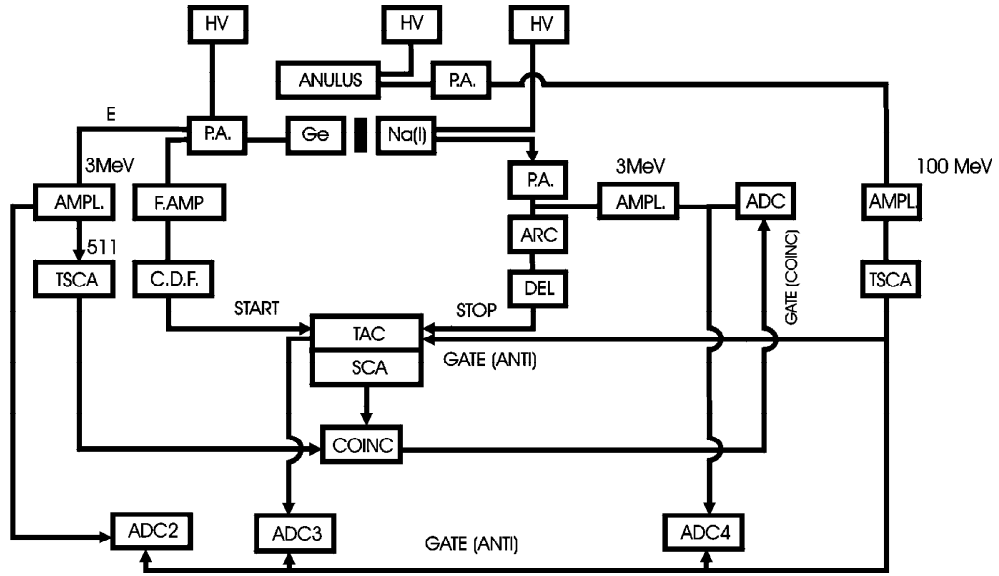


Figure 1. The setup for measuring β^+/EC decay of ^{50}Cr .

to the excellent time resolution of the fast circuit, the number of random coincidences was negligible. Both the NaI(Tl) and the HPGe detectors were actively shielded by the $23\text{ cm} \times 23\text{ cm}$ NaI(Tl) guard detector. The whole assembly was operated inside a 25 cm wall thickness 4π passive iron shield. The coincidence efficiency of the system $\varepsilon = R_C/A$ (R_C - true coincidence count rate, A - positron source activity) is determined by the Monte Carlo simulation and direct measurements with a calibrated ^{22}Na source has the value of $\varepsilon = 1.9\%$ [9].

3. Results and discussion

The results obtained by integration in the 511 keV region are summarized in Table 1. Thus in the coincidence spectrum the net 511 keV intensity was not found.

Table 1. The results obtained by integration in the 511 keV region.

	Cr	background
511-511 coinc.count rate $[(\text{ks})^{-1}]$	53(11)	57(12)
measurement time [ks]	1040	926

In the experiment for the $209\text{ g Cr}_2\text{O}_3$, which contains $4.7\text{ g }^{50}\text{Cr}$, we derived the upper limit of the half-life $T(0\nu + 2\nu) \geq 2.6 \cdot 10^{18}\text{ y}$ (at 68% CL). Our limit is by an order of magnitude more stringent than the value $T(0\nu + 2\nu) \geq 1.8 \cdot 10^{17}\text{ y}$ derived by Norman [3].

Acknowledgments

The authors acknowledge the financial support of the Ministry of Science and Technology of Serbia in the frame of the project Nuclear Spectroscopy and Rare Processes (No.1859).

References

1. M. Doi and T. Kotani, Prog. Theor. Phys. **89**, 139 (1993).
2. M. Kirsch et al., Z. Phys. **A 347**, 151 (1994).
3. E. B. Norman, Phys. Rev. **C 31**, 1937 (1985).
4. G. Gervasio et al., in *Double Beta Decay and Related Topics*, ed. H. V. Klapdor-Kleingrothaus and S. Stoica, p. 475, (World Scientific, Singapore, 1995).
5. I. Bikit, J. Slivka, Ž. Djurčić, N. Žikić, M. Vesković, M. Krmar, Lj. Čonkić, Double Beta Decay Experiments in Novi Sad, 3rd International Symposium, Interdisciplinary Regional Research, Novi Sad, 1998., Federal Ministry for Development, Science and Environment and University of Novi Sad.
6. I. Bikit, M. Krmar, J. Slivka, M. Vesković, Lj. Čonkić, I. Aničin, New Results on the Double Beta Decay of Iron, Phys. Rev. **C 58**, 2566 (1998).
7. Ž. Djurčić, I. Bikit, N. Žikić, M. Vesković, J. Slivka, M. Krmar, Lj. Čonkić, I. Aničin, Shell Effect in Some Weak Nuclear Processes, Journal of Research in Phys. **27**, 3 (1998).
8. I. Bikit, M. Krmar, J. Slivka, I. Aničin, M. Vesković, Lj. Čonkić, Electron-positron Conversion Decay of ^{64}Zn , Appl. Radiat. Isotop. **46**, 455 (1995).
9. I. Bikit, M. Krmar, J. Slivka, M. Vesković, Lj. Čonkić, I. Aničin, Proc. of 28 ICHEP, 1255 (World Scientific, Singapore, 1997).
10. V. I. Tretyak and Yu. G. Zdesenko, Tables of Double Beta Decay Data, (preprint CRN 95-0, Strasbourg, 1995).

Evaluating the Dispersion Relation of Surface Electron Plasma Waves by the Fixed-Point Method

V. Babović and M. Kovačević

Faculty of Science, University of Kragujevac, R. Domanovića 12,

34000 Kragujevac, Yugoslavia

E-mail: vukot@knez.uis.kg.ac.yu

Received: June 16, 1999

Abstract

Analysis of different formulas for surface electron plasma waves has shown the necessity for evaluating the dispersion relation. Since this equation is very complex and implicit, the calculations are not clearly seen. In this paper an attempt has been made in order to overcome the difficulties, by applying the fast convergent iteration algorithm.

Key words: Electromagnetic propagation, surface electron plasma waves, fixed-point method

1. Definition of the surface function

The dispersion relation of surface electron plasma waves can be written down in a form which immediately points to the existence of a guiding surface crucial for the wave:

$$-\varepsilon_p = \varepsilon_g F[X, Y(X)] . \quad (1)$$

The function $F[X, Y(X)]$, which appears in the above equation, can be named as the surface function. The surface function traces the way how the resonance condition of a surface mode $-\varepsilon_p = \varepsilon_g$ is modified for limited values of wave wavelengths and, in the case of vanishing small wavelengths, it approaches unity, i.e.

$$\lim_{X \rightarrow \infty} F[X, Y(X)] = 1 . \quad (2)$$

Here X stands for the wavenumber of the surface wave, normalized by means of a suitable geometrical variable (e.g. the radius of the plasma column), whereas Y is the normalized angular frequency: $Y = \frac{\omega}{\omega_p}$, with ω_p as the angular plasma frequency. In this paper we treat only cold homogeneous plasmas which could be conceived as dielectrics of permittivity $\varepsilon_p = 1 - \frac{1}{Y^2}$. This is a simple and very frequent case which imposes no principle limitations on the procedure we will propose. The plasma is in contact with an ordinary dielectric, having permittivity ε_g , in accordance to the model of a sharp boundary.

We will now concretize the relation (1) i.e. the surface function for several important specific configurations.

A) For a plasma half-space we have

$$F[X, Y(X)] \equiv F_- = \frac{\sqrt{X^2 + p_0^2(1 - Y^2)}}{\sqrt{X^2 - Y^2 p^2}} \quad (3)$$

where $p = \frac{\omega_p R}{c}$ and $p_0 = \frac{\omega_p R}{c_0}$, c_0 being the speed of light in the vacuum and $c = \frac{c_0}{\sqrt{\epsilon_g}}$ the speed of light in the surrounding glass. Parametres p , or p_0 , give the level of electron concentrations in the plasma and will be referred to as the electron density parametres. The normalizing length R is the height of a slot-antenna arrangement (or an analogous quantity for other launchers).

B) For a plasma layer of half-width a it holds that

$$F[X, Y(X)] \equiv F_+ = \frac{\sqrt{X^2 + p_0^2(1 - Y^2)}}{\sqrt{X^2 - Y^2 p_0^2 \epsilon_g}} \coth \sqrt{X^2 + p_0^2(1 - Y^2)}. \quad (4)$$

Here $X = \frac{2\pi a}{\lambda}$ and the expression is valid for the anti-symmetric mode of surface waves.

C) As long as we have in mind a plasma cylinder placed in an infinitely thick glass it must be

$$F[X, Y(X)] \equiv F_0 = \frac{ua I_0(ua) K_1(\nu a)}{\nu a I_1(ua) K_0(\nu a)}. \quad (5)$$

The expression contains various modified Bessel functions of orders 0 and 1 and arguments

$$ua = \sqrt{X^2 - p^2 Y^2 \frac{\epsilon_p}{\epsilon_g}}, \quad (6)$$

$$\nu a = \sqrt{X^2 - p^2 Y^2}. \quad (7)$$

D) Finally, in the most realistic case describing a plasma column in a cylindrical vessel of a wall thickness $\delta = b - a \equiv a(d - 1)$ and permittivity ϵ_g we can put

$$F[X, Y(X)] \equiv F_{\oplus} = \frac{r_{31} m_1}{r_{32} m_2 - r_{33} m_3}. \quad (8)$$

The coefficients r_{ij} are derivatives of the type $\frac{d}{dz}[zZ(z)]$, i.e.

$$r_{31} = [u_1 a I_1(u_1 a)]'; \quad (9)$$

$$r_{32} = [u_2 a I_1(u_2 a)]'; \quad (10)$$

$$r_{33} = [u_2 a K_1(u_2 a)]'. \quad (11)$$

The structure of the matrices m_i is as follows

$$m_1 = \begin{bmatrix} -I_1(u_2 a) & -K_1(u_2 a) & 0 \\ I_1(u_2 b) & K_1(u_2 b) & -K_1(u_3 b) \\ [u_2 b I_1(u_2 b)]' & [u_2 b K_1(u_2 b)]' & -\epsilon_g [u_3 b I_1(u_3 b)]' \end{bmatrix}; \quad (12)$$

$$m_2 = \begin{bmatrix} I_1(u_1a) & -K_1(u_2a) & 0 \\ 0 & K_1(u_2b) & -K_1(u_3b) \\ 0 & [u_2bK_1(u_2b)]' & -\varepsilon_g [u_3bI_1(u_3b)]' \end{bmatrix}; \quad (13)$$

$$m_3 = \begin{bmatrix} I_1(u_1a) & -I_1(u_2a) & 0 \\ 0 & I_1(u_2b) & -K_1(u_3b) \\ 0 & [u_2bI_1(u_2b)]' & -\varepsilon_g [u_3bK_1(u_3b)]' \end{bmatrix}. \quad (14)$$

The transverse wavenumbers u_i are defined in the standard way

$$u_1 = \sqrt{\beta^2 - k_0^2 \varepsilon_p}; \quad u_2 = \sqrt{\beta^2 - k_0^2 \varepsilon_g}; \quad u_3 = \sqrt{\beta^2 - k_0^2}. \quad (15)$$

Here $k_0 = \frac{\omega}{c_0}$ is the free space wavenumber, and $\beta = 2\pi/\lambda$.

2. On the necessity of approximation of the dispersion relation

The D) model of a surface wave guiding medium, though fairly complicated, is the most important one, being closely related to many experimental arrangements, particularly in the area of gas discharge plasmas. In applications, when we have to implement the dispersion relation into a formula, it should be very convenient to manipulate with an expression of the type $Y = f(X)$, instead of an implicit equation $D(X, Y(X)) = 0$ in accordance with (1). In order to overcome this difficulty one often uses the quasistatic approximative expression of the dispersion relation; it formally follows from eqs. (1) and (8) considering the limiting process $c_0 \rightarrow \infty$. Having in mind that such a treatment leads to the reduction $u_i \rightarrow \beta = \frac{2\pi}{\lambda}$ (s. eq. (15)), the function F_{\oplus} loses the term containing the angular frequency ω . Unfortunately, the quasistatic dispersion relation appears to be useless in the region of small wavenumbers.

In papers [1], [2] we stressed that an interesting approximative expression can be achieved by means of the concept of an equivalent dielectric. The basic idea is in the application of a layer model in the hierarchy of various guiding structures. So, one treats the plasma column as an unbounded homogeneous dielectric and replaces the permittivity ε_g with the effective permittivity like this:

$$\varepsilon_g^{eff} = 1 + (\varepsilon_g - 1) \tanh[(d - 1)X]. \quad (16)$$

Here d is the width parameter of the glass tube surrounding the plasma cylinder, in fact the quotient of radii, $d = \frac{b}{a}$. In that way, the dispersion relation follows from eqs. (1) and (5) and reads

$$Y = \frac{1}{\sqrt{1 + \varepsilon_g^{eff} F_0}}. \quad (17)$$

This approximation can in many cases successfully replace the full dispersion relation of the more complicated model (D), eq. (8).

In paper [3] the authors tested the validity of a square-root approximation in the initial part of the dispersion relation (the important region $X \sim 0.5$ characterized by an increased power of the wave). A good agreement with experimental results has been established. In addition to this, a square-root function can be proved to be an analytical reduction of the expression consisting of many Bessel functions regularly existing in the full wave dispersion relation. Otherwise, dispersion relations of the type $\omega = const \cdot \sqrt{k}$ are known

in some wave propagation theories and the reduction to such an investigated class could serve as a source of additional useful analogies. Unfortunately, this type of approximation leads to unacceptable deviations already for wavenumbers $X \sim 1$. During the last decade, the practical possibilities of a numerical processing of complicated formulas have been radically improved. In this context, it is interesting to consider the efficiency of the fixed-point method in connection with the mentioned dispersion relation. As far as we know, the existing literature has not reported about this topic and we are here going to say in some details more on the iteration procedure.

3. Iterative process

Starting from eq. (1) we can write the dispersion relation in the form

$$Y = f(X, Y(X)) , \quad (18)$$

where

$$f(X, Y(X)) = \frac{1}{\sqrt{1 + \varepsilon_g F(X, Y(X))}} . \quad (19)$$

Let $Y_0(X)$ be an initial, or zero order approximation (deduced via the method of an equivalent dielectric, or in any other way). Putting Y_0 into the right-hand side of eq. (18) we formally get the first-order approximation

$$Y_1 = f(X, Y_0(X)) . \quad (20)$$

Continuing the iterative process, we can now use the above result as a starting value in order to get the second-order approximation, i. e.

$$Y_2 = f(X, f(X, Y_1(X))) . \quad (21)$$

Of course, we can also perform any of the higher-order approximations according to the algorithm

$$Y_i = f(X, f(X, Y_{i-1}(X))) \quad (22)$$

although there is no true need for solutions with $i > 2$, as we are going to confirm in this paper.

By the fixed point method one can easily control the desired precision. Up-to-date PC packets, such as various *Mathematica* programs, contain developed algorithms in full agreement with our idea. For example, by means of the command

$$\text{FixedPointList}[Y, Y_0, \text{SameTest} \rightarrow (\text{Abs}[\#1-\#2] < 10^{-3} \ \&)]$$

the iterative action (22) is activated and it stops after two successive results differing by less than 0.001. This shows how fast the Y function converges to its fixed point.

The fixed-point method noticeably simplifies software manipulations, computations are faster and programming more clear.

4. Our results

Let us now present several results of our computations based on the fixed-point method. We have chosen the zero-order approximation in accordance with the equivalent dielectric

model, i. e.

$$Y_0 = \frac{1}{\sqrt{1 + (1 + (\varepsilon_g - 1) \tanh[(d - 1)X]) \frac{I_0(X) K_1(X)}{I_1(X) K_0(X)}}}. \quad (23)$$

Following eq. (20), we can construct the expression for the first-order approximation Y_1 , having in mind eq. (19), too. This function is graphically represented in Fig. 1, for the following set of parameters: $d = 1.2$, $p = 0.5$ and $\varepsilon_g = 4.8$.

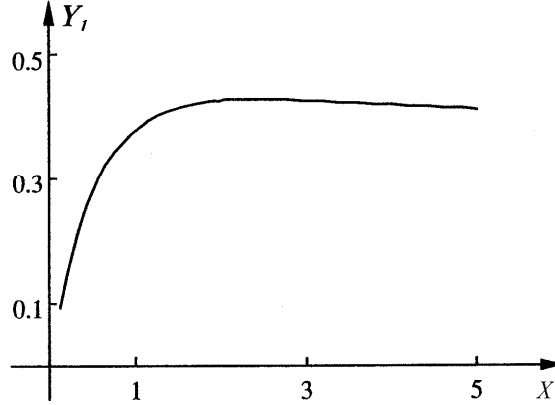


Figure 1. The first-order approximation of the dispersion relation; the reduced angular frequency as a function of the normalized wave number for the following set of parameters: $d = 1.2$, $p = 0.5$ and $\varepsilon_g = 4.8$.

We have proved that practically the same graphic is obtained when the starting function Y_0 is the known quasistatic approximation

$$Y_0 = (1 + \varepsilon_g M)^{-1/2} \quad (24)$$

where

$$M = \frac{I_0(X) (\varepsilon_g - 1) I_1(X) K_0(Z) K_1(Z) + K_1(X) S(Z)}{I_1(X) (1 - \varepsilon_g) I_0(X) K_0(Z) K_1(Z) + K_0(X) S(Z)}, \quad (25)$$

with the abbreviation

$$S(Z) = I_0(Z) K_1(Z) + \varepsilon_g K_0(Z) I_1(Z), \quad (26)$$

having the value $Z = Xd$ as the argument of Bessel functions.

In the Table 1 we have given a comparative survey of various approximations of the dispersion relation, for several values of the wave number of the axially symmetric surface electron wave where we have defined δ_1 as the relative difference between Y_1 and Y_0 , δ_2 between Y_2 and Y_1 and δ between true value Y and Y_0 . All the results stated in the Table hold for the following set of parameters: $d = 1.2$, $p = 0.5$ and $\varepsilon_g = 4.8$.

One can easily prove that the iterative process rapidly converges. The approximations Y_2 and Y_1 differ by less than one percent, even for the wave numbers much less than unity. The results are more convincing for low values of the density parameter p , for example in the region $p \sim 0.1$ (gas discharge plasmas). It is important that the approximation Y_1 almost entirely cancels the known defects innate to the quasistatic function in the region of small wave numbers. Of course, in the region of small wave lengths the errors δ_i are negligible.

Table 1. Approximations of the dispersion relation and related errors for several values of the wave number of the axially symmetric surface wave.

X	0.2	0.3	0.5	0.7	1	1.5	2	3
Y	0.161735	0.214277	0.288741	0.336827	0.380444	0.413968	0.424977	0.424323
Y_0	0.175879	0.228176	0.300517	0.346542	0.387934	0.419213	0.428857	0.426639
Y_1	0.159431	0.212742	0.288055	0.336491	0.380307	0.413924	0.424957	0.424317
Y_2	0.162088	0.214439	0.28878	0.336838	0.380446	0.413968	0.424977	0.424323
δ	8.74517	6.48646	4.0784	2.88427	1.96875	1.26701	0.91299	0.54581
δ_1	10.31669	7.254797	4.326257	2.987004	2.005485	1.277771	0.91774	0.547232
δ_2	1.639233	0.791367	0.251056	0.103017	0.036536	0.010629	0.004706	0.001414

In Fig.2 we see the dependence of δ_1 on X for various values of p . The necessary corrections in regard to the zero-order approximation gives Y_1 for small wave numbers, especially if plasmas are sufficiently dense (when $\omega_p a$ tends to the velocity of light).

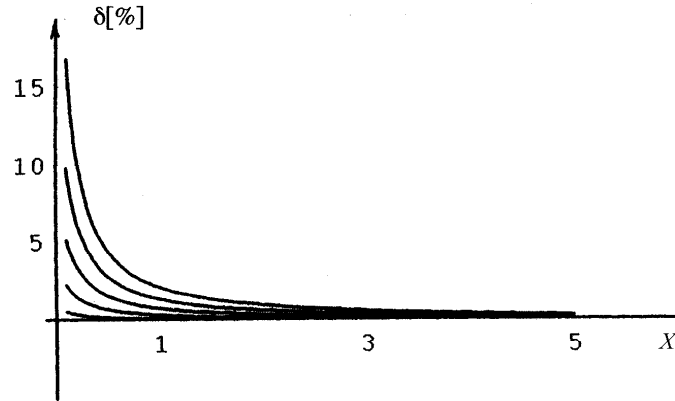


Figure 2. Percentage error as a function of the normalized wave number of the surface waves for various values of electron density.

The dependence of δ_1 on p for various values of X is shown in Fig. 3.

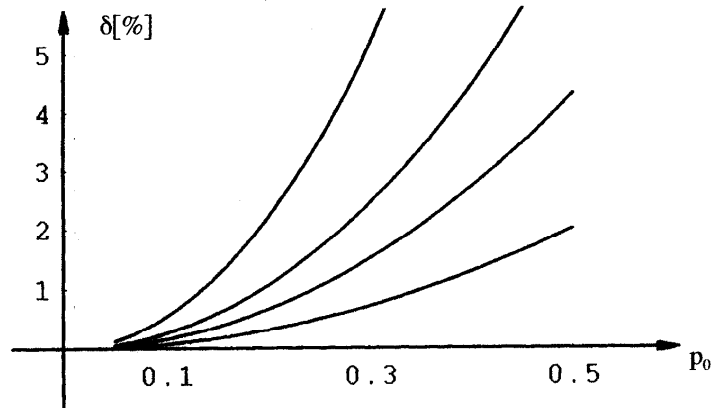


Figure 3. Percentage error as a function of electron density for several relevant values of surface wave numbers.

If the parameter of electron density p is not greater than 0.5 and the wave number is not greater than 0.3, the deviation of the first-order approximation from the zero-order one is not greater than 5%. At the beginning, the dependence $\delta_1 = f(p_0)$ goes as $\delta_1 = C(X)p_0^2$, the function $C(X)$ decreases as the wave number increases and, in fact, can be approximated as $C(X) \approx \frac{C_0}{X^n}$, if the exponent n is adequately chosen (s. Fig. 2, our guess is $n = 2$).

5. Conclusion

In conclusion we stress the following. In problems connected with surface electron plasma waves one always faces the need to implement the dispersion relation. Nevertheless, the dependence $D(X, Y(X)) = 0$ is (as a rule) unusually complicated and in fact implicitly defined, so, computations can be somewhat inconvenient and the results often fairly opaque.

As far as we know, in literature has not yet been reported that the mentioned difficulties could be efficiently overcome by applying the iterative procedure. We have shown that the fixed point method offers indeed an adequate treatment of the dispersion relation; the method is especially effective if one has to compute the frequency from the equation of the type $D(X, Y(X)) = 0$ in the scope of a general problem connected with surface electron plasma waves. The axially symmetric wave has the dispersion relation which can be put into the form (1). The plasma permittivity depends on the wave number via a set of expressions and, implicitly, via the frequency in several transverse wave numbers of the type $X_{T_i}^2 = X^2 - Y^2 p_0^2 \varepsilon_i$. The second term in this expression is usually much less than the first one; the permittivity ε_p is almost entirely insensitive to the term $X_p^2 = Y^2 p_0^2 \varepsilon_i$, unless $X \sim \frac{\omega}{c_0} \sqrt{\varepsilon_g}$. So, it is important that we can retain the term X_p^2 and, at the same time, it is unessential whether X_p^2 has its true value or an approximative one. This means that we can successively compute more and more precise approximations, the convergence being achieved and the iteration process short. The zero-order approximation can be chosen by many possible means, each of them will lead to a correct result after some definite number of iterations. We have tried starting with the approximation based on our method of an equivalent dielectric. The good zero-order approximation is also the quasistatic approximation. One can also try starting with a constant term $X_p = const$, for example putting initially $Y_0 = \frac{1}{\sqrt{1+\varepsilon_g}}$ (the resonant frequency of surface waves).

For $p_0 \leq 0.1$ (gas-discharge plasmas, in various gases and vapors), the solution Y_1 is quite satisfactory, the errors cannot be greater than one percent for any reasonable value of wave numbers.

It is important that the short iterative procedure offers the useful way of explication of a dispersion relation, which is fully compatible with up-to-date computational abilities.

In this paper we have treated only the axially symmetric surface electron wave. We believe a similar procedure could be applied to higher-order modes, too. In addition, it seems that the fixed-point method could be powerful for plasma media and guiding structures more complicated than treated here. The investigations directed toward such problems are in progress and the results will be reported elsewhere.

References

1. V. M. Babović, Electron plasma waves on cylindrical structures and the concept of an equivalent dielectric, *Zeitschrift fur Naturforschung* **50a**, 897 (1995).
2. V. M. Babović, The dipole mode dispersion relation of the electron waves on an equivalent plasma/dielectric interface, *Facta Universitatis* **1**, 127 (1995).
3. V. M. Babović, B. A. Aničin, D. M. Davidović, The square root approximation to the dispersion relation of the axially symmetric electron wave on a cylindrical plasma, *Zeitschrift fur Naturforschung* **52a**, 709 (1997).
4. V. Babović, S. Milojević, M. Kovačević, Axially symmetric electron plasma surface waves on equivalent cylindrical guiding structures, *Collec. of Scien. Papers of the Fac. of Sci. Kragujevac* **17**, 107 (1995).
5. B. A. Aničin, Excitation of surface waves on plasmas, *Fizika* **2**, 45 (1970); IBK - 480, Beograd - Vinča, Oct. 1969.
6. B. A. Aničin, V. M. Babović, K. E. Lonngern, Excitation of nanosecond waves on positive columns, *Journal of Plasma Physics* **7**, 403 (1972).
7. V. M. Babović, B. A. Aničin, D. M. Davidović, The tide-rip effect as a common wave phenomenon, *Collec. of Scien. Papers of the Fac. of Sci. Kragujevac* **13**, 45 (1992).
8. V. M. Babović, B. A. Aničin, D. M. Davidović, On the axial variation of the electron density in a plasma column of the surfatron type, *Physica Scripta* **55**, 86 (1997).

A Three-Particle Cluster and the Problem of Binding Energies

Ljubisav Novaković

*Department of Physics, Svetozar Marković University,
34000 Kragujevac, Radoje Domanović 12, P. O. Box 60, Yugoslavia
E-mail: ljnovak@knez.uis.kg.ac.yu*

Received: November 15, 1999

Abstract

Using quite general terms, the cold - fusion research programme can be developed from three physically independent approaches, one classical, another quantum - mechanical, yet another electrodynamical. Equations of motion are applied to a specific model of three - particle clusters, e^-pe^- , or e^-de^- . Here the heavy particle (proton p , deuteron d) is assumed to perform a rotation with respect to the axis which joins these two motionless electrons. The binding energies and separation distances are evaluated by employing classical as well as quantum - mechanical approaches. One should emphasize that the former two approaches, classical as well as quantum - mechanical, agree fairly well within the geometric - structural model of the clusters about the order of magnitude for the mentioned physical quantities. In particular,

$$|E(e^-p(d)e^-)| \approx 22(44) \text{ keV}; \quad r_0 \approx 30(15) \text{ fm};$$

$$|E(e^-p(d)e^-)| \approx 19(38) \text{ keV}; \quad r_0 \approx 70(35) \text{ fm}.$$

Here r_0 designates a separation distance of the proton (deuteron) from the axis of rotation. The above cited figures are associated with the classical and quantum - mechanical approximations, respectively. At the end of the paper we consider a simple idea, by studying the action of combined electric and magnetic induction fields within the third physical approach, of how to introduce a possible mechanism to materialize the predicted states of the particle clusters. This would depend on many technical details within the specific experimental arrangement.

Key words: Cold-fusion research, tightly bound states, Niels Bohr's third postulate, Lorentz force

1. Statement of the problem

Recently observed "excess heat", in a cold-fusion research programme, requires a more fundamental approach to the problem of the binding energies of a non-nuclear origin. Here obviously we are dealing with a research field which is somewhere between atomic physics, on one side, and nuclear physics, on the other. Energies and classical distances in atomic

physics are expressed by the order of magnitude 10 eV and $1 \text{ \AA} = 10^{-10} \text{ m}$, respectively. Here by definition, $1 \text{ eV} = 1.60210 \cdot 10^{-19} \text{ J}$, where J designates one joule, m is one metre. However, these two quantities in nuclear physics are approximately five orders of magnitude greater (10^6 eV , binding energies; $1 \text{ fm} = 10^{-15} \text{ m}$, separation distances). In the present report we start with the idea of a deeply bound state for a three - particle cluster, e.g. the system $e^-pe^- = \text{H}^-$, or an electrically equivalent system $e^-de^- = \text{D}^-$, where $p(d)$ designates the proton (deuteron). Our present study is directed towards three various approaches, classical, quantum - mechanical, and electrodynamic. First, we look at the system of three bound particles under the classical action of various Coulomb forces (attractive as well as repulsive), where the heavy particle (proton, deuteron) has an angular momentum about the axis which passes through the two motionless electrons, Section 2. Second, there is a general quantum - mechanical approach which is based on a series of algebraic transformations of the operators that are associated with the kinetic and potential energies of the constituents of any three - particle cluster, Section 3. Furthermore, the motion of the heavy particle (p, d) under the action of the Coulomb forces as generated by two separate sources is studied quantum - mechanically in Section 4.

There is finally an electrodynamic approach. Just how the two kinds of particle (electrons on one side, the heavy particles on the other) behave under the action of an applied Lorentz force, which might lead to the collapse of the three - particle cluster to deep bound states, as imagined in the present research paper, is considered in Section 5. The order of magnitude of a few physical quantities (e.g. binding energies, separation distances, magnetic induction fields) are discussed in Section 6.

2. A classical approach to the three - particle cluster

This is one of the important problems in contemporary physics. It involves the atomic clusters which consist of three particles, as follows: H^- , He , Li^+ , Be^{++} , etc. The present problem is different from that in celestial mechanics. However, in atomic mechanics (whether classical or quantum - mechanical) we deal with all kinds of forces, attractive as well as repulsive, of a short as well as long range. On the contrary, in celestial mechanics we consider only the exclusively long - range attractive forces, so that the methods in one mechanics are not any more available in the other mechanics.

Having studied a three - particle cluster, which is characterized by 9 degrees of freedom, we must end up with a solution which has 9 constants of motion. Let us enumerate all the constants of motion by studying a very specific atomic model. In fact, with three particles in mind we can develop two different geometric - structural models, whose distinctions will come solely from the electrostatic arguments.

- (i) There is a model where one particle stays almost still all the time while the other two are moving around, the model usually associated with the helium - atom problem.
- (ii) Another model is materialized where two particles stay almost motionless all the time while the third particle is moving around their joining line, the model similar to a hydrogen molecular ion, H_2^+ .

We shall consider the model under (ii) in more detail, but with the nucleus playing the role of the electron, while the electrons would stay almost motionless. Here we have

to introduce 9 constants of motion as a consequence of having a physical system with 9 degrees of freedom. Three degrees of freedom are associated with the centre of mass of the entire cluster, as illustrated by the point C in Figure 1. Additional three degrees of freedom are associated with the identical particles A_1 and A_2 (a fixed separation distance R , plus the fixed line A_1A_2 , making three degrees of freedom altogether), Figure 1.

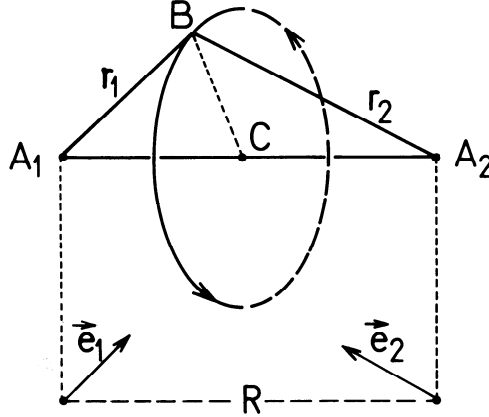


Figure 1. Two identical particles (A_1, A_2) are placed a distance R apart with a centre of mass C , while the third particle B is orbiting around the common centre C in a plane which is perpendicular to the A_1A_2 line. The unit vectors \vec{e}_1 and \vec{e}_2 are parallel with A_1B and A_2B , respectively.

Finally, the problem is reduced to the consideration of another set of three degrees of freedom, i. e. three constants of motion left available for the third particle. Clearly and obviously, this particle may move in a plane which is perpendicular to a line which joins A_1 with A_2 , so that there are two constants of motion materialized by the angular momentum of the third particle. (An angular momentum being a vector is defined by two elements, one scalar quantity and the direction of the vector). Lastly the ninth constant of motion is just the energy of the third particle, which at the same time is the energy of the entire cluster. Hence, there are three degrees of freedom, or equivalently three constants of motion, associated with the third particle (angular momentum, plane of the motion, total energy).

Actually we have to prove that such a geometric - structural model, as illustrated in Figure 1, can be materialized to have the angular momentum as the true constant of motion. Suppose that the third particle B has to move under the influence of two various forces, \vec{F}_1 and \vec{F}_2 , whose origins come from the identical particles placed at the points A_1 and A_2 , respectively. Then an angular momentum \vec{L} of the third particle is defined by a sum of two terms, each term coming from an appropriate vector product, as follows

$$\vec{L} = \vec{r}_1 \times \vec{p} + \vec{r}_2 \times \vec{p}, \quad (1)$$

where \vec{p} designates a linear momentum associated with the B particle. It is just a product over the mass of the particle (m_3) and its velocity. The equation of motion for the vector \vec{L} is given by

$$\frac{d\vec{L}}{dt} = \frac{d}{dt}(\vec{r}_1 + \vec{r}_2) \times \vec{p} + (\vec{r}_1 + \vec{r}_2) \times \frac{d\vec{p}}{dt}, \quad (2)$$

where t is a local laboratory time. Writing,

$$\vec{F}_1 + \vec{F}_2 = \frac{d\vec{p}}{dt}; \quad \vec{p} = m_3 \frac{d}{dt}(\vec{r}_1 + \vec{r}_2) = \vec{p}_1 + \vec{p}_2, \quad (3)$$

we obtain,

$$\frac{d\vec{L}}{dt} = \frac{1}{m_3}(\vec{p}_1 + \vec{p}_2) \times (\vec{p}_1 + \vec{p}_2) + (\vec{r}_1 + \vec{r}_2) \times (\vec{F}_1 + \vec{F}_2). \quad (4)$$

It should be emphasized that a vector sum $\vec{r}_1 + \vec{r}_2$ in equations (2) to (4) appears as a single vector in a plane which is perpendicular to the A_1A_2 line, hence the angular momentum vector \vec{L} is parallel with the above mentioned line, Figure 1. Having in mind that central forces act simultaneously on the particle B , i. e. \vec{F}_1 is parallel to \vec{r}_1 while \vec{F}_2 is parallel to \vec{r}_2 , and taking into account that a vector product of parallel vectors vanishes, we can write equation (4) as follows,

$$\frac{d\vec{L}}{dt} = \frac{1}{m_3}(\vec{p}_1 \times \vec{p}_2 + \vec{p}_2 \times \vec{p}_1) + (\vec{r}_1 \times \vec{F}_2 + \vec{r}_2 \times \vec{F}_1). \quad (5)$$

The first term in equation (5) is obviously equal to zero. As to the second term in brackets, it can be transformed to a specific form appropriate for the equation of motion for \vec{L} . Hence,

$$\frac{d\vec{L}}{dt} = -Ze^2\left(\frac{1}{r_1^3} - \frac{1}{r_2^3}\right)\vec{r}_1 \times \vec{r}_2. \quad (6a)$$

We know that the vector product $\vec{r}_1 \times \vec{r}_2$, due to the geometric - structural model, cannot vanish and yet the angular momentum must be one of the constants of motion associated with the B particle, Figure 1. Hence,

$$\frac{d\vec{L}}{dt} = 0. \quad (6b)$$

Therefore, it follows that a scalar equation $r_1 = r_2$ must hold all the time.

It should be emphasized that this proof holds if and only if the particles A_1 and A_2 are identical so long as we are concerned with electrostatic forces.

Suppose, we have to study an atomic cluster which consists of two electrons and the nucleus, as a binding particle. This model might be materialized in simple atomic clusters, like H^- , He, etc. Here two electrons are separated by a distance R , while the ground state is either symmetric or antisymmetric, according to the arguments of quantum mechanics. However, by employing classical arguments, the energy of the B particle, with the mass m_3 of the heavy particle, will be composed of the potential and kinetic terms,

$$E(R, r_1) = -2Z\frac{e^2}{r_1} + \frac{e^2}{R} + \frac{m_3v^2}{2}, \quad (7a)$$

$$a(R, r_1) = \sqrt{r_1^2 - (R/2)^2}; \quad L = m_3va(R, r_1) = n\hbar. \quad (7b)$$

Here $a(R, r_1)$ designates a classical radius of the orbital motion. The last definition in equation (7b) comes from Niels Bohr's so-called *third postulate*, applied to the orbital motion of the proton (deuteron), $n = 1, 2, \dots$, while $\hbar = 1.05 \cdot 10^{-34}$ Js is Planck's constant divided by 2π . Obviously, the third term in equation (7a) can be transformed accordingly,

$$\frac{m_3v^2}{2} = \frac{2L^2}{m_3(4r_1^2 - R^2)}. \quad (7c)$$

In this case we obtain an equation that can be varied at the same time with respect to both R and r_1 as independent parameters. Therefore, a minimum of the binding energy of such a physical system is obtained from

$$\frac{\partial E}{\partial R} = \frac{\partial E}{\partial r_1} = 0. \quad (8)$$

With m_3 being the B particle, the result is given in a general case,

$$E(R, r_1) \Rightarrow E(Z, L) = Z \left[-16Z + 24(Z/2)^{1/3} - 6(2/Z)^{1/3} + \frac{1}{Z} \right] \frac{m_3 e^4}{8L^2}, \quad (9)$$

$$a(R, r_1) \Rightarrow a(Z, L) = \frac{4L^2}{Zm_3 e^2} \left[4 - (2/Z)^{2/3} \right]^{-3/2}. \quad (10)$$

Notice that the binding energy, according to equation (9), is negative whenever the charge number Z takes the values greater than $Z_0 \approx 0.3$. For $Z = 1$, the binding energy and a radius of the effective orbital motion become,

$$E(1, L) \approx -0.439 \frac{m_3 e^4}{L^2}; \quad a(1, L) \approx 1.067 \frac{L^2}{m_3 e^2}. \quad (11)$$

In all preceding approximations one might insert the value $L = \hbar$ to meet an agreement with Niels Bohr's atomic model. What is more important, we may expect for this model a rather realistic picture as far as the motion of a heavy particle is concerned. However, the limitations of such an approach are discussed in detail by Berry (1989).

These motions are stable in the sense that the binding energy takes a minimum value. In this particular case we can write,

$$R_0 = 2^{1/3} r_{1,0} = 2^{1/3} \left(0.25 R_0^2 + r_0^2 \right)^{1/2}, \quad (12a)$$

$$R_0 = A_1 A_2; \quad r_{1,0} = A_1 B; \quad r_0 = BC; \quad (12b)$$

$$R_0 \approx 1.6216 r_0. \quad (12c)$$

We shall name equations (12a,b,c) the *classical stability condition* which must be satisfied by the three - particle cluster in order to maintain a stable motion of the heavy particle B , Figure 1. This set of equations is to be compared with a similar set (34a,b,c) in the quantum - mechanical case.

3. A quantum-mechanical approach to the three-particle cluster

Consider a system of three particles P_1 , P_2 , and P_3 , with masses m_1 , m_2 , and m_3 , respectively, Figure 2. According to classical mechanics and Figure 2, the position vector of the centre of mass \vec{R} and of the three individual position vectors \vec{r}_i , $i = 1, 2, 3$, can be defined by

$$\vec{R} = \frac{1}{M} \left(m_1 \vec{r}_1 + m_2 \vec{r}_2 + m_3 \vec{r}_3 \right); \quad M = m_1 + m_2 + m_3; \quad (13)$$

$$\vec{r} = \vec{r}_1 - \vec{r}_3; \quad \vec{r}' = \vec{r}_2 - \vec{r}_3. \quad (14)$$

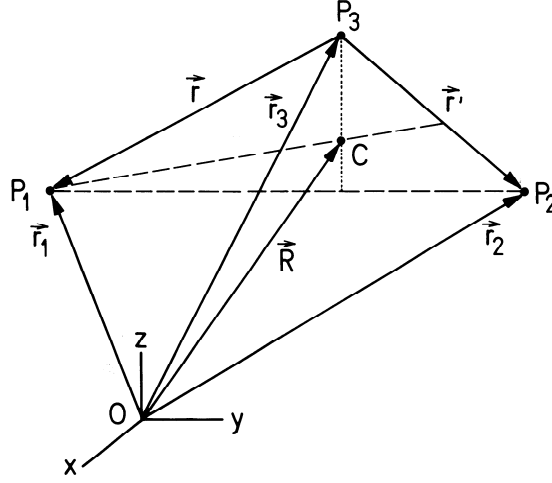


Figure 2. An arbitrary system of rectangular Cartesian axes, $Oxyz$, where three particles (P_1 , P_2 , P_3) and their centre of mass C are depicted at four different points, separated by the vectors \vec{r}_1 , \vec{r}_2 , \vec{r}_3 , and \vec{R} , respectively, from the common origin. Here \vec{r} and \vec{r}' designate relative coordinates, from P_1 to P_3 and P_2 to P_3 , respectively.

We want to transform the operator of the total energy, thus including the kinetic energies as well as all three potential interactions due to the Coulomb forces among the particles, by employing various rectangular Cartesian axes. Hence

$$\mathcal{H} = -\frac{\hbar^2}{2m_1}\Delta_1 - \frac{\hbar^2}{2m_2}\Delta_2 - \frac{\hbar^2}{2m_3}\Delta_3 + V(r_{13}) + V(r_{23}) + V(r_{12}); \quad (15)$$

$$\Delta_1 = \frac{\partial^2}{\partial x_1^2} + \frac{\partial^2}{\partial y_1^2} + \frac{\partial^2}{\partial z_1^2}. \quad (16)$$

Similar definitions hold for the operators Δ_2 and Δ_3 . Let us introduce three additional operators, one associated with the variables (x, y, z) , another with (x', y', z') , and yet another with the centre of mass (X, Y, Z) . Therefore,

$$\Delta = \frac{\partial^2}{\partial x^2} + \frac{\partial^2}{\partial y^2} + \frac{\partial^2}{\partial z^2}; \quad (17)$$

$$\Delta_c = \frac{\partial^2}{\partial X^2} + \frac{\partial^2}{\partial Y^2} + \frac{\partial^2}{\partial Z^2}. \quad (18)$$

A similar definition holds for Δ' .

There are a number of algebraic transformations which involve various derivations, for example,

$$\begin{aligned} \frac{\partial}{\partial x_1} &= \frac{\partial}{\partial x} \frac{\partial x}{\partial x_1} + \frac{\partial}{\partial X} \frac{\partial X}{\partial x_1} = \frac{\partial}{\partial x} + \frac{m_1}{M} \frac{\partial}{\partial X}; \\ \frac{\partial^2}{\partial x_1^2} &= \frac{\partial^2}{\partial x^2} + 2\frac{m_1}{M} \frac{\partial^2}{\partial x \partial X} + \left(\frac{m_1}{M}\right)^2 \frac{\partial^2}{\partial X^2}. \end{aligned} \quad (19)$$

There are similar expressions for the remaining operators. Therefore,

$$\Delta_1 = \Delta + 2\frac{m_1}{M}\mathcal{A} + \left(\frac{m_1}{M}\right)^2 \Delta_c; \quad (20a)$$

$$\Delta_2 = \Delta' + 2\frac{m_2}{M}\mathcal{A}' + \left(\frac{m_2}{M}\right)^2\Delta_c; \quad (20b)$$

$$\mathcal{A} = \vec{\nabla} \cdot \vec{\nabla}_c; \quad \mathcal{A}' = \vec{\nabla}' \cdot \vec{\nabla}_c. \quad (20c)$$

Obviously, the operators \mathcal{A} and \mathcal{A}' are just scalar products between the vector operators $\vec{\nabla}$ and $\vec{\nabla}_c$, and $\vec{\nabla}'$ and $\vec{\nabla}_c$, respectively. Furthermore,

$$\Delta_3 = \Delta + 2\mathcal{B} + \Delta' - 2\frac{m_3}{M}\mathcal{A} - 2\frac{m_3}{M}\mathcal{A}' + \left(\frac{m_3}{M}\right)^2\Delta_c, \quad (21)$$

$$\mathcal{B} = \frac{\partial^2}{\partial x \partial x'} + \frac{\partial^2}{\partial y \partial y'} + \frac{\partial^2}{\partial z \partial z'} = \vec{\nabla} \cdot \vec{\nabla}'. \quad (22)$$

Here equation (22) is just a scalar product between the vector operators $\vec{\nabla}$ and $\vec{\nabla}'$.

Another set of transformations leads to

$$\mu = \frac{m_1 m_3}{m_1 + m_3}; \quad \mu' = \frac{m_2 m_3}{m_2 + m_3}; \quad (23)$$

$$\frac{1}{m_1}\Delta_1 + \frac{1}{m_2}\Delta_2 + \frac{1}{m_3}\Delta_3 = \frac{1}{\mu}\Delta + \frac{1}{\mu'}\Delta' + \frac{2}{m_3}\mathcal{B} + \frac{1}{M}\Delta_c. \quad (24)$$

Here \mathcal{B} is defined in equation (22). Therefore, the total Hamiltonian of a three - particle system has suffered a number of transformations. Its final form is given by

$$\mathcal{H} = -\frac{\hbar^2}{2\mu}\Delta - \frac{\hbar^2}{2\mu'}\Delta' - \frac{\hbar^2}{2M}\Delta_c - \frac{\hbar^2}{m_3}\mathcal{B} + V(r_{13}) + V(r_{23}) + V(r_{12}). \quad (25)$$

The eigenvalue problem is now reduced to the solution of the following equation,

$$\mathcal{H}\phi(\vec{r}, \vec{r}', \vec{R}) = E_t\phi(\vec{r}, \vec{r}', \vec{R}), \quad (26)$$

where one can write the total wave function ϕ as a product of three independent wave functions. Hence the original eigenvalue problem is further reduced to a system of three independent eigenvalue problems, as follows,

$$\phi(\vec{r}, \vec{r}', \vec{R}) = \phi_c(\vec{R}) \cdot \psi(\vec{r}) \cdot \chi(\vec{r}'); \quad (27)$$

$$\left[-\frac{\hbar^2}{2\mu}\Delta + V(r_{13})\right]\psi(\vec{r}) = E\psi(\vec{r}); \quad (28a)$$

$$\left[-\frac{\hbar^2}{2\mu'}\Delta' + V(r_{23})\right]\chi(\vec{r}') = E'\chi(\vec{r}'); \quad (28b)$$

$$-\frac{\hbar^2}{2M}\Delta_c\phi_c(\vec{R}) = E_c\phi_c(\vec{R}); \quad (28c)$$

$$E + E' + E_c = E_t. \quad (28d)$$

Here E_t designates the total energy of the physical system. If we succeed in solving equations (28a,b,c,d), we can treat, at least in principle, the rest of the Hamiltonian \mathcal{H} as a weak perturbation. Actually, this operator can be written as a sum over the unperturbed part \mathcal{H}_0 and a perturbation V' . Hence,

$$\mathcal{H} = \mathcal{H}_0 + V'; \quad (29)$$

$$\mathcal{H}_0 = -\frac{\hbar^2}{2\mu}\Delta - \frac{\hbar^2}{2\mu'}\Delta' - \frac{\hbar^2}{2M}\Delta_c + V(r_{13}) + V(r_{23}); \quad (30a)$$

$$V' = -\frac{\hbar^2}{m_3}\mathcal{B} + V(r_{12}). \quad (30b)$$

For a physical system of three particles in the helium - atom problem (H^- , He , Li^+ , Be^{++}, \dots), we take $m_1 = m_2$ to be the mass of an electron, m_3 the mass of the nucleus. Notice that such a situation is characterized if the ratio $m_1/m_3 = m_2/m_3$ tends to zero. At the same time m_3 tends to infinity. In this case,

$$V(r_{13}) = -Z\frac{e^2}{r_{13}}; \quad V(r_{23}) = -Z\frac{e^2}{r_{23}}; \quad V(r_{12}) = \frac{e^2}{r_{12}}; \quad (31)$$

$$\mathcal{B} = \text{grad}\psi(\vec{r}) \cdot \text{grad}\chi(\vec{r}') = \frac{\partial\psi}{\partial x}\frac{\partial\chi}{\partial x'} + \frac{\partial\psi}{\partial y}\frac{\partial\chi}{\partial y'} + \frac{\partial\psi}{\partial z}\frac{\partial\chi}{\partial z'}, \quad (32)$$

where the introduced wave functions ψ and χ are certain functions of \vec{r} and \vec{r}' , respectively. Furthermore, using the system of spherical coordinates where the origin is placed at the nucleus of the helium atom, we write

$$\psi = f(r, \vartheta, \varphi); \quad \chi = g(r', \vartheta', \varphi'); \quad (33a)$$

$$\text{grad}f(r) = f'(r)\vec{e}_1; \quad \text{grad}g(r') = g'(r')\vec{e}_2. \quad (33b)$$

Here the unit vectors \vec{e} and \vec{e}' are associated with the triangle $P_1P_2P_3$, Figure 2. The symbol f' designates the first derivative of f with respect to r . A similar definition holds for g' with respect to r' . The unit vectors are depicted along the lines P_3P_1 and P_3P_2 , respectively. Similarly, the unit vectors \vec{e}_1 and \vec{e}_2 are associated with the triangle A_1A_2B , along the lines A_1B and A_2B , respectively, Figure 1. A very important situation arises whenever the unit vectors \vec{e}_1 and \vec{e}_2 are mutually perpendicular. Hence, the kinetic part of the perturbation V' would in this case vanish identically, i.e. $\mathcal{B} = 0$. The unit vectors introduced above, close an angle α that can be evaluated by elementary considerations. Indeed, looking at the triangle A_1A_2B , Figure 1, we obtain

$$R^2 = (A_1B)^2 + (A_2B)^2 - 2(A_1B) \cdot (A_2B)\cos\alpha; \quad (34a)$$

$$R = A_1A_2; \quad r_1 = r_2 = A_1B = A_2B; \quad r = BC; \quad (34b)$$

$$R_0 = \sqrt{2}r_{1,0} = 2r_0. \quad (34c)$$

The result of the last equation (34c) implies that α must be a right angle (90°) if the unit vectors \vec{e}_1 , \vec{e}_2 are perpendicular one with respect to the other. This leads to the minimum values for all three introduced distances, R , r_1 , r , as indicated by equation (34c). We shall name equations (34a,b,c) the *quantum - mechanical stability condition* which must be satisfied by the three - particle cluster in order to maintain the stable motion of the heavy mass m_3 at the point B in Figure 1. This set of equations is to be compared with a similar set (12a,b,c) in the classical case.

There are two options as to the general quantum - mechanical solutions of equations (25) to (33b). Those solutions may be specified as follows:

- (i) If $m_1 = m_2$ is small and m_3 is large then the above system of equations may be reduced to the helium - atom problem, where the \mathcal{B} term in equation (32) can be neglected while $V(r_{12})$ remains the only perturbation to be taken into consideration. This problem is already treated in literature, e. g. Baker *et al* (1990), Davis (1963), Novaković (a, 1991; b, 1997);
- (ii) If however we assume the mass ratio as that quoted under item (i), but having the model where the light particles stay still (e. g. the electrons), while the heavy particle moves around the line which joins the two light particles (e. g. the proton, or deuteron), then the model is similar to that of a hydrogen molecular ion, H_2^+ . It could be reduced to a series of various approximations, see Blokhintsev (1976), Pauling and Wilson (1935). It could be treated exactly in terms of elliptic coordinates, see Landau and Lifshitz (a, b, 1987).

In the present paper we adopt a method based on a combination of a classical approach where the angular momentum of the heavy particle L is treated according to Niels Bohr's model with $L = n\hbar$, $n = 1, 2, \dots$. Also we may select the coordinate system r, ϑ, φ in such a way that a z axis coincides with the line A_1A_2 , Figure 1. In this case $\vartheta = \pi/2$ while φ is arbitrary. Here the operator of the angular momentum, according to Dirac (1962), or Edmonds (1960), becomes,

$$\mathcal{L}^2 = -\hbar^2 \frac{d^2\psi}{d\varphi^2}; \quad \psi(\varphi) = \frac{1}{\sqrt{2\pi}} \exp(im\varphi). \quad (35)$$

In equation (35) $m = 0, \pm 1, \pm 2, \dots$ is a magnetic quantum number. In this particular case the quantity $|m|$, for m different from zero, can be identified in Niels Bohr's atomic model with the angular momentum quantum number n , Section 2.

4. Motion of a particle in the potential field $2Ze^2/\sqrt{r^2 + (R/2)^2}$

In the present section we shall consider a quantum - mechanical solution of the following equation,

$$-\frac{\hbar^2}{2m_3} \left(\frac{\partial^2}{\partial x^2} + \frac{\partial^2}{\partial y^2} \right) \Phi + [V(r) - E] \Phi = 0,$$

$$V(r) = -2Z \frac{e^2}{\sqrt{r^2 + (R/2)^2}}. \quad (36)$$

In equation (36) m_3 is the heavy particle (possibly proton), E is the total energy of the particle whose motion is restricted in the xy plane passing through the midpoint between A_1 and A_2 , Figure 1. The solution will be achieved in a series of three computing stages. First, the total wave function will be represented by a product of two wave functions, one depending on r , another on the azimuthal angle φ . We write,

$$\Phi(r, \varphi) = \chi(r) \cdot \psi(\varphi), \quad (37a)$$

$$x = r \cos \varphi; \quad y = r \sin \varphi,$$

$$\frac{\partial^2}{\partial x^2} + \frac{\partial^2}{\partial y^2} = \frac{\partial^2}{\partial r^2} + r^{-2} \frac{\partial^2}{\partial \varphi^2}. \quad (37b)$$

Second, we introduce a dimensionless coordinate ρ and a dimensionless energy ϵ , as follows,

$$\begin{aligned} r &= \eta^{-1} a_0 \rho; & E &= \eta E_a \epsilon; & \eta &= \frac{m_3}{m_1}; \\ a_0 &= \frac{\hbar^2}{m_1 e^2} = 0.5291 \cdot 10^{-8} \text{ cm}; \\ E_a &= \frac{e^2}{a_0} = \frac{m_1 e^4}{\hbar^2} = 27.214 \text{ eV}; & \xi &= \frac{R}{a_0}. \end{aligned} \quad (38)$$

Hence, equation (36) goes over into,

$$\left(\rho^2 \frac{\partial^2}{\partial \rho^2} + \frac{\partial^2}{\partial \varphi^2} \right) \Phi + 2\rho^2 \epsilon \Phi + 4Z \frac{\rho^2}{\sqrt{\rho^2 + (\xi/2)^2}} \Phi = 0. \quad (39)$$

Third, we now separate $\chi(\rho)$ from $\psi(\varphi)$, by introducing a constant C , which leads to

$$\frac{d^2 \psi}{d\varphi^2} = -C \psi(\varphi); \quad C = m^2, \quad (40a)$$

$$\left(\frac{d^2}{d\rho^2} + 2\epsilon + \frac{4Z}{\sqrt{\rho^2 + (\xi/2)^2}} - \frac{C}{\rho^2} \right) \chi(\rho) = 0. \quad (40b)$$

The term involving the potential field in equation (40b) must be transformed according to the quantum - mechanical stability condition derived in equations (34a,b,c), i.e. the condition by which the position vectors \vec{r}_1 and \vec{r}_2 close a right angle, as indicated in Figure 1. This condition leads to

$$R = 2r; \quad \xi = 2\rho; \quad \Rightarrow \frac{4Z}{\sqrt{\rho^2 + (\xi/2)^2}} = \frac{2\sqrt{2}Z}{\rho}. \quad (41)$$

The last equation (40b), if supplemented with the stability condition according to equation (41), can be reduced to the eigenvalue problem whose solution is actually available, see Landau and Lifshitz (b, 1987). Having introduced a substitution,

$$\chi(\rho) = \exp(-\alpha\rho) \rho^k \cdot h(\rho), \quad (42a)$$

$$2\epsilon = -\alpha^2; \quad k = \frac{1}{2} \left(1 + \sqrt{1 + 4m^2} \right), \quad (42b)$$

we arrive at the following equation for $h(z)$, instead of $h(\rho)$,

$$zh''(z) + (c - z)h'(z) - ah(z) = 0; \quad (43a)$$

$$z = 2\alpha\rho; \quad c = 2k; \quad a = \frac{\alpha k - 2\sqrt{2}Z}{\alpha}. \quad (43b)$$

The actual solution of equations (43a,b) is obtained by employing the confluent hypergeometric function,

$$h(z) = N(a, c) \left[1 + \frac{az}{c!} + \frac{a(a+1)z^2}{c(c+1)2!} + \dots \right], \quad (44)$$

where $N(a, c)$ is a normalization factor to be determined from the condition,

$$\int_0^\infty [\chi(\rho)]^2 \rho d\rho = 1. \quad (45)$$

First, we would like to emphasize that the above introduced integration runs over a plane, rather than the entire three-dimensional space as employed in conventional quantum - mechanical problems. Second, the representation (44) for the function $h(z)$ must be interrupted in order to make the expansion series convergent. This will take place whenever the parameter a is a negative integer or zero. Therefore, by writing

$$a = -n_r, \quad n_r = 0, 1, 2, \dots \quad (46a)$$

we obtain,

$$\alpha = \frac{\sqrt{2}Z}{k + n_r}; \quad \epsilon = -\frac{\alpha^2}{2} = -\frac{Z^2}{(k + n_r)^2}. \quad (46b)$$

Here n_r designates the number of nodes, i.e. the number of null - points of the polynomial $h(z)$. It is easy to evaluate the radius r at which the wave function $[\chi(\rho)]^2 \rho$, (it represents a quantum - mechanical distribution associated with a planar motion of the particle), has a maximum. Indeed, assuming the lowest stationary state generated by the quantum number $n_r = 0$, we search for the solution

$$\frac{d}{d\rho} [\exp(-2\alpha\rho)\rho^{2k+1}] = 0 \Rightarrow \rho_0 = \frac{2k + 1}{2\alpha}. \quad (47)$$

5. A three-particle cluster under the action of a time-dependent Lorentz force

Just how the electrons might attain some motionless positions, even for a short time interval, while the heavy particle (p , or d) performs a rotational motion may be gained from the following idea. Suppose, the mentioned composite cluster moves in a linear direction under the action of the crossed electric and magnetic induction fields, E_y and B_x , with an initial velocity \vec{v}_0 , Figure 3. Such a combined field is known under the name of a *Lorentz force*, Burghes and Downs (1975), Feynman *et al* (1964), Yavorsky and Pinsky (1987).

The motion of each particle with the charge q and mass m is compelled by the Lorentz force \vec{F} according to the equations,

$$\vec{F} = q(\vec{E} + \vec{v} \times \vec{B}), \quad (48a)$$

$$\vec{v} \times \vec{B} = \begin{vmatrix} \vec{i} & \vec{j} & \vec{k} \\ v_x & v_y & v_z \\ -B_x & 0 & 0 \end{vmatrix}. \quad (48b)$$

We shall consider specifically the following clusters $e_1^- p e_2^-$, or $e_1^- d e_2^-$, with the following characteristic parameters, electron ($q = -e, m = m_1$), proton ($q = e, m = m_3$), and deuteron ($q = e, m = 2m_3$). Obviously, the three unit vectors $\vec{i}, \vec{j}, \vec{k}$, are oriented along the rectangular Cartesian axes x, y, z , respectively. We write the equations of motion,

$$\begin{aligned} F_x = m\dot{v}_x = 0; \quad F_y = m\dot{v}_y = qE_y - qB_x v_z; \\ F_z = m\dot{v}_z = qB_x v_y. \end{aligned} \quad (49)$$

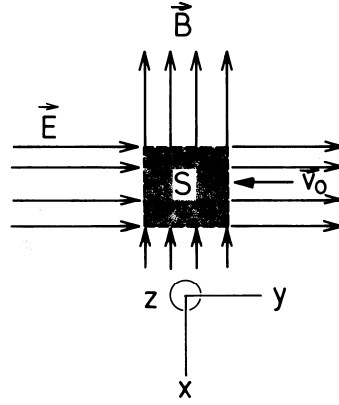


Figure 3. An electric field $\vec{E} = (0, E_y, 0)$, a magnetic induction field $\vec{B} = (-B_x, 0, 0)$, and the initial velocity of the particle \vec{v}_0 , are depicted to represent a Lorentz force acting on a material cluster. A square marked S is the region where the action of the magnetic induction field joins a similar action of the electric field. Notice that an electron will move parallel to the vector \vec{v}_0 whereas heavy particles (p, d) will move in the opposite direction.

Here $e = 1.60210 \cdot 10^{-19}$ C is an elementary electrostatic charge, C designates one coulomb. Dots on the components of the velocity designate the appropriate time derivatives. The solutions to the system of the above linear equations with constant coefficients (m, q, B_x) are some functions of a local laboratory time t , $y(t)$ and $z(t)$, as well as E_y , such that the entire motion, under the action of a Lorentz force, develops in the yz plane. In the first step we write the set of solutions jointly with the initial conditions, C_1 being the integration constant, as follows,

$$\begin{aligned} v_y &= v_0 \cos \omega t + C_1; \\ v_z &= v_0 \sin \omega t + C_1 \omega t; \\ \dot{v}_y &= v_0; \quad v_x = v_z = 0; \quad t = 0; \\ E_y &= B_x C_1 \omega t; \quad m \omega = |q| B_x. \end{aligned} \quad (50)$$

In the second step, another integration with respect to t leads to another set of solutions jointly with the initial conditions,

$$\begin{aligned} y(t) &= R(m, |q|) \sin \omega t + y_0; \\ z(t) &= -R(m, |q|) \cos \omega t + z_0; \\ x(t) &= y(t) = z(t) = 0; \quad t = 0; \\ y_0 &= C_1 t; \quad z_0 = \frac{1}{2} C_1 \omega t^2 + R(m, |q|); \\ R(m, |q|) &= \frac{v_0}{\omega} = \frac{m v_0}{|q| B_x}. \end{aligned} \quad (51)$$

Having studied the above derived equations we come to an important conclusion concerning the shape of the trajectory described by a given particle. Either particle, be it the electron m_1 , or the proton m_3 , or the deuteron with mass $2m_3$, moves in the yz plane along a circle with a radius $R(m, |q|)$ whose centre is placed at the point $(0, y_0, z_0)$. Hence, by transforming equations (50) and (51) we obtain,

$$[y(t) - y_0]^2 + [z(t) - z_0]^2 = R(m, |q|)^2. \quad (52)$$

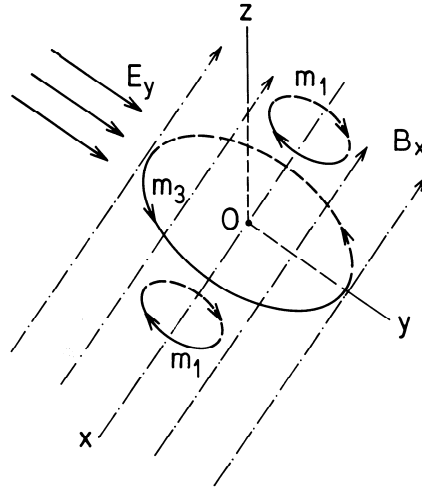


Figure 4. Electric field lines E_y and magnetic induction field lines B_x are depicted to illustrate the action of a Lorentz force on two different kinds of particle.

Therefore, the electrons move in one direction around the magnetic induction field \vec{B} , while the heavy particle (p , or d) moves in the opposite direction, as illustrated in Figure 4. Light particles (electrons) will describe smaller circles in such a way as to materialize a left - handed coordinate system with respect to the vector of the magnetic induction field. On the contrary, heavy particles (protons, deuterons) will describe larger circles, exactly $\eta = m_3/m_1$ times, in the opposite direction, whereby materializing the right - handed coordinate system with respect to the vector of the above mentioned field. At the origin, marked by O , the material cluster starts its simple spiralling, highly rhythmic dancing, along the magnetic induction field lines. Compared to heavy particles, electrons will perform their motions in the opposite direction. Also the circles are centered differently for the two kinds of particle. A similar problem was studied by Burghes and Downs (1975) in relation to the Hall drift, an effect coming from a classical theory of magnetoconductivity.

Having analyzed this situation it seems that there is a strong probability of having the three - particle cluster to collapse to a more profound bound state as predicted by the specifically geometric - structural model.

6. Discussion and conclusions

(1) Within quantum mechanics, the results of Sections 3., 4., and 5. can be visualized rather straightforwardly. If the heavy particle (proton, deuteron) should perform its orbital motion in a plane which is perpendicular to the line connecting the two electrons, as depicted in Figure 1, then we may associate an angular momentum operator \mathcal{L} , whose square is given by equation (35). In this sense the heavy particles (protons, deuterons) may perform rotational motions around the line A_1A_2 which joins the motionless electrons in Figure 1. By inserting into equations (8) to (10) $Z = 1$, $L = \hbar$, $m_3(2m_3)$ the mass of the proton (deuteron), we obtain the binding energy, according to a classical approximation,

$$E(Z, L) \Rightarrow |E_1(e^-pe^-)| \approx 22 \text{ keV}; \quad |E_1(e^-de^-)| \approx 44 \text{ keV}. \quad (53)$$

Also, we obtain the radius of the effective orbital motion for the two particles as follows,

$$a(Z, L) \Rightarrow a_1(e^-pe^-) \approx 30 \text{ fm}; \quad a_1(e^-de^-) \approx 15 \text{ fm}. \quad (54)$$

Similarly, using equations (46a,b) and (47) in the quantum - mechanical approximation, we arrive at the following result,

$$Z = 1; \quad \eta(p, d) = 1836(3672); \quad n_r = 0; \quad |m| = 1;$$

$$k = \frac{1}{2}(1 + \sqrt{5}); \quad \alpha = \frac{2\sqrt{2}}{1 + \sqrt{5}}; \quad (55a)$$

$$E = \eta e_a \epsilon = -\frac{\eta}{k^2} E_a = -\frac{4\eta}{(1 + \sqrt{5})^2} E_a; \quad (55b)$$

$$\frac{d}{d\rho} [\exp(-2\alpha\rho)\rho^{2k+1}] = 0 \quad \Rightarrow \quad \rho_0 = \frac{(2 + \sqrt{5})(1 + \sqrt{5})}{4\sqrt{2}}; \quad (55c)$$

$$r_0 = \eta^{-1} a_0 \rho_0. \quad (55d)$$

Having inserted the proper numerical values for E_a , a_0 , and η , we obtain the energies and separation distances in the quantum - mechanical approximation,

$$|E(e^- p(d)e^-)| \approx 19(38) \text{ keV}; \quad r_0(e^- p(d)e^-) \approx 70(35) \text{ fm}. \quad (56)$$

Our present numerical values (so far as the binding energies are concerned) seem to agree with measurements recently performed by Antanasijević *et al* (1993) on a cold - fusion plasma in connection with the Fleischmann - Pons experiment.

(2) Here one question arises that is related to the precise mechanism by which a three - particle cluster may generate a state considerably deeper than that predicted by the ordinary quantum mechanical lowest bound state. Using the usual vocabulary it is named the ground state whose numerical value for hydrogen and deuterium is approximately 13 eV. In view of the results of Section 3., it is obvious that there must exist an even lower bound state, in the 50 keV energy range, for which we have no explanation of how dynamically it may take place. Even if it does take place, its lifetime must be rather short compared to ordinary atomic or molecular time scales. Indeed, the latter quantity, according to Heisenberg's uncertainty relation connecting the energy (δE) and time (δt), may be written,

$$\delta E \cdot \delta t \approx \hbar. \quad (57)$$

Here the uncertainty δE must be identified with the quantity $|E_1|$ from equation (53). Therefore, a time duration associated with the above mentioned energy range is a quantity of the order $\delta t \approx 10^{-20}$ s. Immediately we notice that such a lifetime is rather close to a typical nuclear time scale.

If such a situation should take place, then the Hamiltonian derived in equations (25) to (33a,b) can be based on the assumption by which the operator \mathcal{B} must vanish identically, while the electron - electron interaction $1/r_{12}$ is expected to remain unaltered all the time. In other words, the two electrons may stay motionless along the $A_1 A_2$ straight line, Figure 1, whereas the heavy particles (proton, deuteron) become ready to perform a rotation in a plane that is placed perpendicular to this straight line. Although this rotation, according to Heisenberg's uncertainty principle, might be materialized for a very short time, nevertheless our present theoretical knowledge is insufficient to offer a proper explanation as to the full mechanism taking place.

(3) Just how the two kinds of particle, bound at the beginning as a linear triatomic molecule $e^- p e^-$, or $e^- d e^-$, like a helium atom, may achieve a very deep bound state is

observed from a series of very fundamental theoretical arguments presented in Section 5. Indeed, under the action of a couple of crossed electric and magnetic induction fields, the linear triatomic molecule becomes broken in such a way as to form a right angle (or, almost the right angle) as closed by the straight lines *electron*(e_1^-) – *proton*(p) and *proton*(p) – *electron*(e_2^-). According to equations (51) and (52) the electrons would stay almost motionless while the heavy particles (p , or d) would perform a spiralling, highly rhythmic dancing, in circles which are three orders of magnitude larger than those performed by the electrons. Using a proper vocabulary, this situation will greatly enhance the chance of generation of partially stable states, until the linear triatomic molecule collapses into a tightly bound state as studied and analyzed in detail in Sections 2., 3., and 4.

In order to gain a numerical insight into the physical mechanism we quote the following estimation. With a rather small initial velocity v_0 , which is obtained if the applied electric field is either weak or actually next to zero, we can investigate the order of magnitude of the magnetic induction field B_x to be applied to a triatomic linear molecule $e_1^-pe_2^-$ in order to enforce it to the process of collapsing. We obtain,

$$E_y = 0; \quad B_x = \frac{m_3v_0}{qR(m_3, q)}. \quad (58)$$

As a numerical illustration we quote the following example,

$$v_0 = 10^{-2} \text{ ms}^{-1}; \quad m_3 = 1.6725 \cdot 10^{-27} \text{ kg}; \quad (59a)$$

$$R(m_3, q) = 2a_0 = 1.06 \cdot 10^{-10} \text{ m}; \quad B_x = 1 \text{ T}. \quad (59b)$$

Here T designates one tesla. Under these conditions the shape of the linear triatomic molecule $e_1^-pe_2^-$ has a considerable chance to be transformed from a straight line to a triangle with a right angle at the point materialized by the proton. Depending on a specific experimental arrangement, one further step is required by this geometric - structural model to collapse into a profound bound state as predicted in Sections 3., 4., and 5. It should be emphasized that only the very slow particles are more favourable for a generation of the above mentioned material units, as compared to the fast particles.

Acknowledgments

I am deeply indebted to Professor Robert Blinc for his warm hospitality during my visits to the University of Ljubljana, Slovenia, in the period 1996 - 1998, where I completed the present manuscript.

References

1. R. Antanasijević, I. Lakićević, Z. Marić, D. Šević, A. Zarić, and J. P. Vigier, *Physics Letters* **A 180**, 25 (1993).
2. J. D. Baker, D. E. Freund, R. N. Hill, and J. D. Morgan III, *Physical Review* **A 41**, 1247 (1990).
3. R. S. Berry, *Contemporary Physics* **30**, 1 (1989).
4. D. I. Blokhintsev, *Osnovi kvantovoj mehaniki*, Chapter XXII, pp. 555 - 576, (Glavnaja redakcija fiziko - matematičeskoj literaturi izdateljstva "Nauka", Moskva, 1976).

5. D. N. Burghes and A. M. Downs, *Modern Introduction to Classical Mechanics and Control*, Chapter 5, (Ellis Horwood Limited, Coll House, Chichester, Sussex, England, 1975).
6. L. H. Davis, *Journal of Chemical Physics* **39**, 1827 (1963).
7. P. A. M. Dirac, *The Principles of Quantum Mechanics*, Section 38, (Clarendon Press, Oxford, 1962).
8. A. R. Edmonds, *Angular Momentum in Quantum Mechanics*, 2nd ed., (Princeton University Press, Princeton, 1960).
9. R. P. Feynman, R. B. Leighton, and M. Sands, *The Feynman Lectures on Physics, Mainly Electromagnetism and Matter*, Chapter 13, (Addison-Wesley Publishing Company, Reading, Massachusetts, 1964).
10. L. D. Landau and E. M. Lifshitz, (a) *Mechanics*, Section 48, (Pergamon Press, Oxford, 1987); (b) *Quantum Mechanics*, Section 36, Section 78, Appendix d, (Pergamon Press, Oxford, 1987).
11. Lj. Novaković, (a) *Kvantna teorijska fizika*, Chapter 7, (Naučna knjiga, Beograd, 1991); (b) Collection of Scientific Papers of the Faculty of Science Kragujevac, **19**, 67 (1997).
12. L. Pauling and E. B. Wilson Jr., *Introduction to Quantum Mechanics*, Section 29, Section 42, (McGraw-Hill Book Company Inc., London, 1935).
13. B. M. Yavorsky and A. A. Pinsky, *Fundamentals of Physics*, Volume I, Chapter 41, (Mir Publishers, Moscow, 1987).

Random Sequential Adsorption of Line Segments on Discrete Substrates with Quenched Impurities

Lj. Budinski-Petković, U. Kozmidis-Luburić and A. Mihailović

*Faculty of Technical Sciences, University of Novi Sad, Trg Dositeja Obradovića 6,
21000 Novi Sad, Yugoslavia*

Received: November 18, 1999

Abstract

Irreversible deposition of line segments on square and triangular lattices initially and randomly occupied with point-like impurities is studied by Monte Carlo simulation. At the late stage of deposition the approach to the jamming coverage is exponential with the same rate as in the case of initially clean lattice. The total jamming coverage decreases when the concentration of impurities p increases and reaches a minimum for the value of p which depends on the length of the line segments. A significant difference in the dependence of the jamming coverage on the concentration of impurities on the square and on the triangular lattice was found only for the deposition of dimers.

Key words: Adsorption, substrate, impurities, jamming coverage

1. Introduction

When particles are deposited onto a surface there are two characteristic time scales: the time between depositions, t_d , and the time taken for the particle reorganization on the surface, t_r . If $t_d \gg t_r$, particles have sufficient time to change their positions on the surface between depositions and the distribution of particles on the surface is an equilibrium distribution. On the other hand, if $t_d \ll t_r$, the particles are effectively fixed in a position once deposited, there is a non-equilibrium distribution of particles and the kinetics is described by the process of random sequential adsorption (RSA). A number of processes in physics, chemistry and biology, where events occur essentially irreversibly on the time scales of interest, can be studied as RSA or irreversible deposition.

RSA is a process in which objects of a specified shape are randomly and sequentially adsorbed onto a substrate. In real systems one needs to take into account the interaction between the bulk particles and the surface and also the interaction between the adsorbed and the bulk particles. We shall focus our attention on the case in which the particle-surface interaction disallows desorption from or diffusion on the surface and its range is small compared to the size of the particles. We shall also assume that the forces among the adsorbing particles are repulsive so they allow formation of only one layer. Since the diffusion of adsorbed objects is not allowed, once an object is placed it affects the geometry

of all later placements, even though each placement happens completely randomly. Thus, the dominant effect in RSA is the blocking of the available substrate area and the limiting ("jamming") coverage $\theta(\infty)$ is less than in close packing. The kinetic properties of a deposition process are described by the time evolution of the coverage $\theta(t)$ which is the fraction of the substrate area occupied by the adsorbed particles. For a review of RSA models, see [1].

Experimentally, RSA has for example been observed in oxidization of one-dimensional polymer chains [2], adhesion of colloidal particles on solid substrates [3], quenched chemisorption of proteins at specific two-dimensional solid surface sites (effectively producing bonds between two or more sites) [4], particles in biological membranes [5], spatial patterns in ecological systems [6], etc..

In the recent work [7] the kinetics of deposition of colloidal hematite particles on glass beads in the presence of cationic surfactant 1-dodecylpyridinium chloride (DPC) was studied at two different pH values: 10.5 and 4.0. At the high pH the surfactant was adsorbed both on particles and beads and depending on the surfactant concentration either monolayer or multilayer deposition was observed. At pH 4.0 only a monolayer of hematite was observed. Deposition of hematite particles occurs only on the surfactant-free collector sites, which is due to the electrostatic repulsion between the adhering particles and the sites of collector covered with surfactant. Thus, DPC adsorbed on glass beads makes a part of collector surface inaccessible for the adsorption of hematite particles.

Theoretical studies of RSA include some analytical results [8-10] (for one-dimensional systems), series expansions [11-13] and Monte Carlo simulations [14-19].

Depending on a system of interest, substrate can be continuum or discrete, and RSA models can differ in substrate dimensionality. The precise form of the long-time behavior of $\theta(t)$ depends also on the shape and orientational freedom of the adsorbing objects.

For lattice RSA models, approach to the jamming coverage is exponential [16], [18], [19]:

$$\theta(t) = \theta(\infty) - Ae^{-t/\sigma} \quad (1)$$

where A and σ are parameters which depend on the shape and orientational freedom of depositing objects. In Monte Carlo study [16] of deposition of line segments on a square lattice, it was found that A depends on the line length ℓ ($A \sim 1/\ell$), but σ is independent of ℓ with a numerical value $\sigma \simeq 0.5$. The jamming coverage decreases exponentially with the size of depositing objects, for small object sizes [18].

A lot of attention has been paid to the RSA on square lattices, but there are only a few studies of RSA on other types of lattices, such as triangular or hexagonal lattice [20, 21].

Here we present the results of Monte Carlo simulations of irreversible deposition on discrete substrates initially occupied with quenched point-like impurities. The results are given both for the square and for the triangular lattice.

2. Irreversible deposition on disordered substrates

For RSA of k -mers on a 1D lattice initially occupied with point-like impurities, an exponential approach to the jamming coverage of the form (1) was found. The value of the rate σ was found to be the same as in the case of initially non-occupied 1D lattice, that is $\sigma = 1$. This result was obtained analytically [10] and numerically [17]. The jamming coverage depends on the segment length and on the concentration of impurities. The total

jamming coverage, which includes deposited particles and point-like impurities, decreases as the relative concentration of impurities p increases and reaches a minimum value for $p = \frac{1}{2}$ in the case of dimer deposition [10]. For increased concentrations, jamming coverage grows and for $p = 1$ reaches unity. Exact results were also obtained for longer objects, covering three and four lattice sites, and the minimum is shifted towards lower impurity concentrations when the length of the objects increases.

In the present work disordered substrates are modeled by the square and by the triangular lattice with randomly distributed inaccessible sites. The depositing objects are line segments which can be placed along the lattice axis only. The size of the lattice is $L = 128$ in both cases and periodic boundary conditions are used in all directions.

Before each run through the system the lattice is initially and randomly occupied with point-like impurities at concentration p . At each deposition attempt we randomly select a lattice site and try to place the line segment of length ℓ (covering $\ell + 1$ lattice sites). On the square lattice a line segment can be placed in four possible orientations and on the triangular lattice in six possible orientations with one end at the selected lattice site. If the selected site is unoccupied, we try to deposit the object, i.e., we fix one end of the line at this site and try to place the segment in any of the possible orientations. If all successive ℓ sites are unoccupied, we occupy these $\ell + 1$ sites and deposit the segment. If the attempt fails, we randomly choose another orientation, and so on, until all possibilities are examined. In the case that the object cannot be placed in any of the possible directions (it is irrelevant whether it was because some of the ℓ sites were occupied by impurities or by an already deposited segment), this site is denoted as inaccessible. During the simulation we record the number of all inaccessible sites in the lattice. These include the occupied sites and the sites which are unoccupied but cannot be one end of the line segment. If we select an inaccessible site we do not attempt to deposit the object but increase the time by one unit. Jamming limit is reached when the number of inaccessible sites is equal to the total number of sites in the lattice. The time is counted by the number of attempts to place the objects and scaled by the total number of lattice sites. The data are averaged over 100 independent runs for each lattice, each length of the lines and each concentration of impurities.

Simulations are performed for a wide range of impurity concentrations and for objects of various lengths. The plots of $\ln(\theta(\infty) - \theta(t))$ vs. t are straight lines at the late stages of deposition, for all the cases, suggesting that the approach to the jamming coverage is exponential of the form (1). Moreover, the slopes of these lines are the same as in the case of initially clean lattice, $\sigma \simeq 0.57$. That means that in the presence of quenched impurities rapidity of the approach to the jamming limit does not change. The quantity which depends on the impurity concentration is the jamming coverage $\theta(\infty)$.

3. Jamming coverages on disordered substrates

The results of simulations of RSA on disordered substrates can be considered in two ways. If we are interested in total coverages, then the coverage includes deposited line segments and point-like impurities and it starts with value $\theta_p(0) \neq 0$. Simulations are performed for line segments of length $\ell = 1, 2, 3$ and 4 and for impurity concentrations up to 70% for the square lattice and up to 80% for the triangular lattice. The results for the total jamming coverages are given in Table 1 and Table 2 for the square and for the triangular lattice, respectively. As the relative concentration of impurities p increases,

$\theta_p(\infty)$ decreases, reaches a minimum value, and grows for increased concentrations as a consequence of high impurity concentrations. For $p = 1$ we have a trivial result $\theta(\infty) = 1$. When the line segments covering two lattice sites ($\ell = 1$) are deposited on the square lattice, the total jamming coverage reaches the minimum value for p between 55% and 60%. In the case of deposition of longer line segments, the minimum is reached at 50%, 45% and 40% of impurities for $\ell = 2, 3$ and 4, respectively. When the line segments of length $\ell = 1, 2, 3$ and 4 are deposited on the triangular lattice, the minimum is reached at 70, 50, 43 and 40 percent of impurities, respectively. The values from Table 1 and Table 2 are plotted in Figure 1. We can see that the minimum is shifted towards lower concentrations of impurities when ℓ increases.

Table 1. The total jamming coverages for line segments of length $\ell = 1, 2, 3, 4$ and for impurity concentrations up to 70% on the square lattice.

p [%]	$\theta_p(\infty)$			
	$\ell = 1$	$\ell = 2$	$\ell = 3$	$\ell = 4$
0	0.9191	0.8541	0.8145	0.7877
2	0.9163	0.8470	0.8021	0.7694
4	0.9131	0.8402	0.7903	0.7528
6	0.9112	0.8334	0.7791	0.7375
8	0.9091	0.8280	0.7690	0.7230
10	0.9068	0.8219	0.7592	0.7092
15	0.9018	0.8088	0.7377	0.6789
20	0.8974	0.7979	0.7203	0.6558
25	0.8931	0.7881	0.7050	0.6377
30	0.8898	0.7809	0.6932	0.6234
35	0.8870	0.7744	0.6848	0.6145
40	0.8843	0.7685	0.6799	0.6102
45	0.8817	0.7657	0.6770	0.6114
50	0.8804	0.7648	0.6793	0.6180
55	0.8797	0.7659	0.6854	0.6314
60	0.8797	0.7699	0.6967	0.6512
65	0.8811	0.7778	0.7139	0.6784
70	0.8842	0.7898	0.7382	0.7131

Table 2. The total jamming coverages for line segments of length $\ell = 1, 2, 3, 4$ and for impurity concentrations up to 80% on the triangular lattice.

p [%]	$\theta_p(\infty)$			
	$\ell = 1$	$\ell = 2$	$\ell = 3$	$\ell = 4$
0	0.9243	0.8456	0.7960	0.7636
2	0.9243	0.8415	0.7878	0.7506
4	0.9246	0.8382	0.7783	0.7355
6	0.9244	0.8342	0.7710	0.7238
8	0.9245	0.8311	0.7634	0.7124
10	0.9244	0.8277	0.7572	0.7013
15	0.9241	0.8203	0.7428	0.6810
20	0.9241	0.8156	0.7315	0.6635
25	0.9239	0.8105	0.7229	0.6525
30	0.9235	0.8077	0.7175	0.6447
35	0.9230	0.8043	0.7128	0.6396
40	0.9226	0.8025	0.7097	0.6382
45	0.9223	0.8011	0.7096	0.6404
50	0.9214	0.8000	0.7104	0.6446
55	0.9206	0.8005	0.7139	0.6538
60	0.9200	0.8029	0.7218	0.6690
65	0.9196	0.8061	0.7337	0.6910
70	0.9194	0.8142	0.7527	0.7209
75	0.9204	0.8259	0.7781	0.7574
80	0.9230	0.8443	0.8113	0.8006

In order to see how the arrangement of the impurities affects the jamming coverage, we performed some additional simulations for the square lattice. In these simulations the impurities were distributed only before the first run through the system and this distribution remained unchanged for all 100 runs. The results of these simulations are in Figure 1a plotted with open symbols, while the results for the simulations in which the impurities are distributed before each run through the system are plotted with corresponding closed symbols. The difference in the total jamming coverage in these two cases can be observed only for large values of impurity concentrations and it is always less than 0.5%.

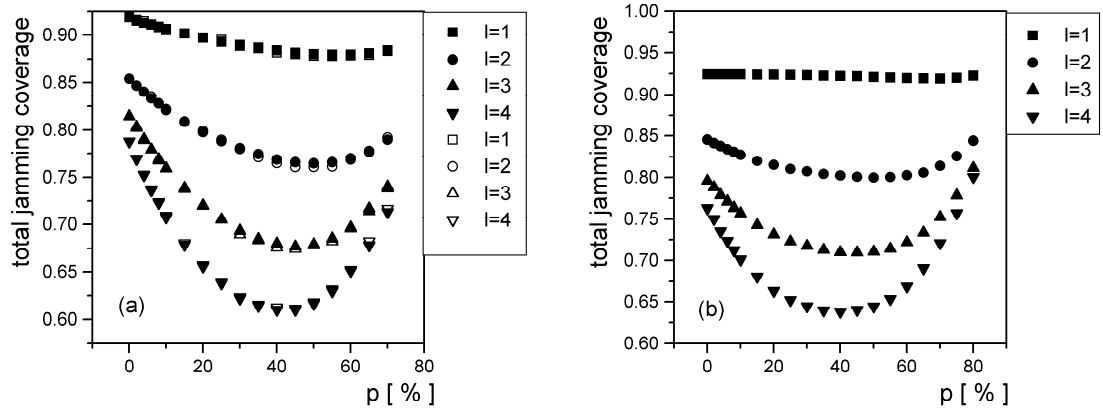


Figure 1. Dependence of the total jamming coverage on impurity concentration for $\ell = 1, 2, 3, 4$: a) for the square lattice; b) for the triangular lattice.

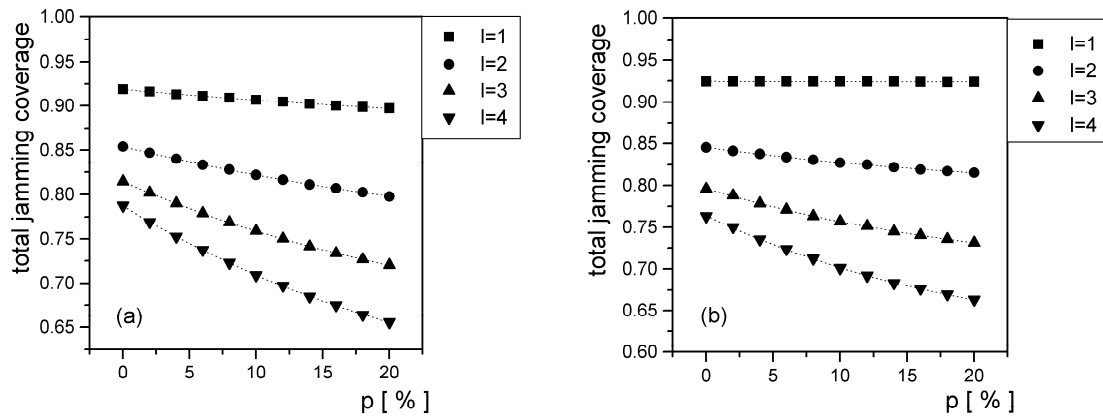


Figure 2. The total jamming vs. impurity concentration for $\ell = 1, 2, 3, 4$ and $p \leq 20\%$: a) for the square lattice; b) for the triangular lattice. The dotted lines represent the exponential fit of the form: $\theta_p(\infty) = C_0 + C_1 e^{-p/\beta}$

In Figure 2 the total jamming coverage is given as a function of impurity concentration p for $p \leq 20\%$. The dotted lines represent the exponential fit of the form:

$$\theta_p(\infty) = C_0 + C_1 e^{-p/\beta} \quad (2)$$

where C_0 , C_1 and β are parameters which depend on the length of the lines, and they are given in Table 3 for the square lattice and in Table 4 for the triangular lattice. As the length of the depositing objects gets larger, β decreases, i.e., the total jamming coverage decreases more rapidly with impurity concentration. For higher concentrations of impurities domains available for deposition are smaller and deposition of longer line segments is more affected by this fact. The decrease of β with ℓ is more prominent in the case of the triangular lattice than in the case of the square lattice. In Figure 3 the same data are shown on a semi-log scale.

On the other hand, the quantity of interest can also be the fraction of substrate area covered with depositing objects (line segments only). In Figure 4 the jamming coverages due to the line segments of lengths $\ell = 1, 2, 3, 4$ are plotted vs. impurity

concentration for $p \leq 20\%$. These plots are nearly straight lines for low values of impurity concentration and their slope increases with the length of depositing objects.

Table 3. Parameters C_0 , C_1 and β for $\ell = 1, 2, 3, 4$ in the case of the square lattice.

ℓ	C_0	C_1	β
1	0.8676	0.0514	36.390
2	0.7304	0.1237	33.250
3	0.6256	0.1891	28.756
4	0.5350	0.2526	26.985

Table 4. Parameters C_0 , C_1 and β for $\ell = 1, 2, 3, 4$ in the case of the triangular lattice.

ℓ	C_0	C_1	β
1	0.8971	0.0275	940.764
2	0.7847	0.0610	29.097
3	0.6825	0.1138	23.760
4	0.6012	0.1633	20.687

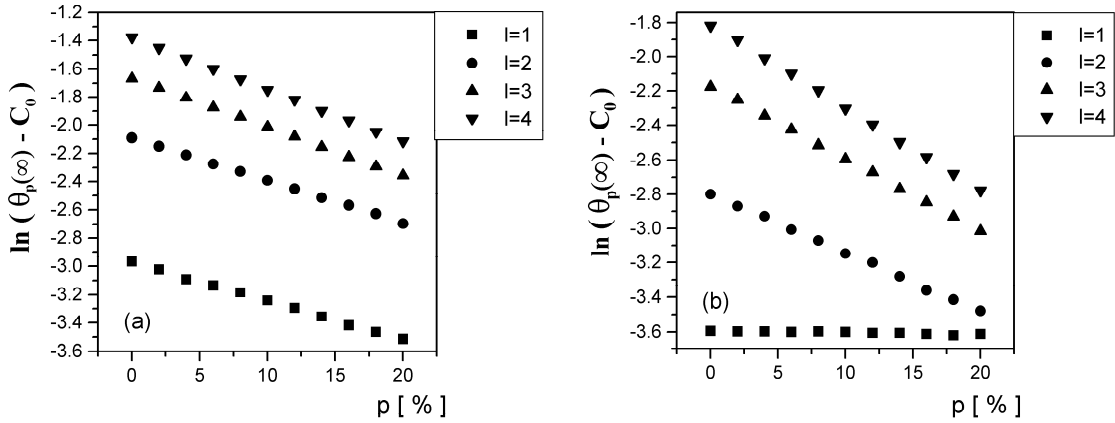


Figure 3. As Figure 2 on semi-log scale: a) for the square lattice; b) for the triangular lattice.

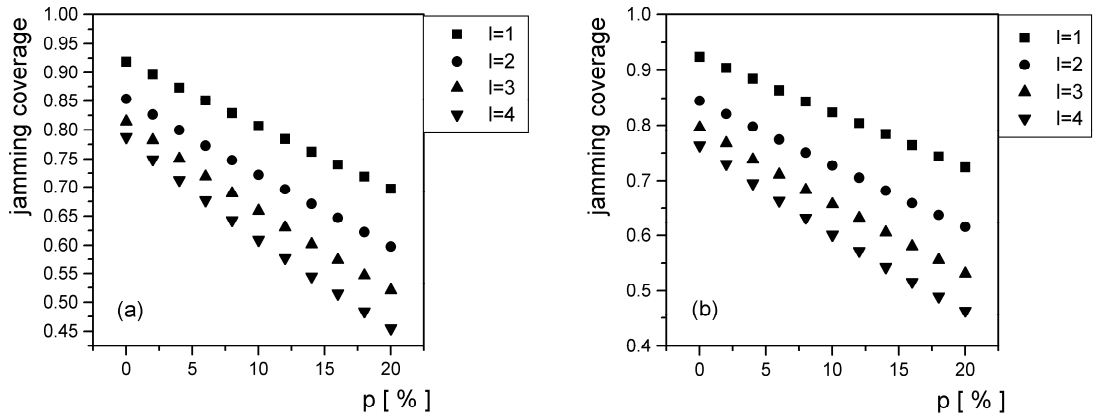


Figure 4. Dependence of the jamming coverage (due to the depositing line segments only) on impurity concentration for $\ell = 1, 2, 3, 4$: a) for the square lattice; b) for the triangular lattice.

4. Conclusion

The deposition of line-segments on discrete substrates initially occupied with point-like impurities has been studied by Monte Carlo simulation. The simulations were performed

for the square and for the triangular lattice. The approach to the jamming coverage is exponential with the same rate as in the case of initially clean lattice.

The total jamming coverage decreases with impurity concentration p for low values of p , reaches a minimum, and increases for high impurity concentrations. The minimum is shifted towards lower values of p for longer objects. A similar behavior is obtained analytically for one-dimensional deposition of k -mers [10]. The total jamming coverage decays exponentially with p for low values of impurity concentration and this decay is more rapid for longer objects.

If we compare these results for the square and the triangular lattice, we can see that there is a significant difference in the case of dimer deposition ($\ell = 1$): the minimum values of the total jamming coverage are reached at higher values of impurity concentration and the total jamming coverage exhibits only a slight decay in the case of the triangular lattice. This difference is due to the orientational freedom of depositing objects, i.e., on a triangular lattice there is a greater number of possible orientations and enhanced possibility for avoiding the point-like impurities, so the deposition of dimers is almost not affected by the presence of impurities. On the other hand, the deposition of longer line segments is more influenced by the domain sizes available for the deposition, i.e., by the impurity concentration, and this influence produces similar effects in the cases of the square and the triangular lattice.

The jamming coverage due to the depositing objects only, decreases almost linearly with p for low values of p . This decrease is also more rapid for longer line segments.

Acknowledgments

This work was supported by the Serbian Ministry of Science and Technology under project "Dynamical and Thermodynamical Properties of Strongly Correlated Systems with Complex Structures" (No 1895).

References

1. J. W. Evans, Rev. Mod. Phys. **65**, 1281 (1993).
2. J. J. Gonzalez, P. C. Hemmer and J. S. Hoye, Chem. Phys. **3**, 228 (1974).
3. N. Kallay, M. Tomić, B. Biskup, I. Kunjašić and E. Matijević, Colloids Surf. **29**, 185 (1987).
4. J. Feder and I. Giaever, J. Coll. Interface Sci. **78**, 144 (1980).
5. L. Finegold and J. T. Donnell, Nature **278**, 443 (1979).
6. M. Hasegawa and M. Tanemura, in *Recent Developments in Statistical Interference and Data Analysis*, edited by K. Matusita, (North-Holland, Amsterdam, 1980).
7. A. Zelenev, *Effects of Surfactants on Particle Adhesion*, Dissertation, (Clarkson University, 1997).
8. R. Swendsen, Phys. Rev. **A 24**, 504 (1981).
9. M. C. Bartelt and V. Privman, J. Chem. Phys. **93**, 6820 (1990).
10. E. Ben-Naim and P. L. Krapivsky, J. Phys. A: Math. Gen. **27**, 3575 (1994).

11. J. Evans and R. S. Nord, *J. Stat. Phys.* **38**, 681 (1985).
12. M. Nakamura, *Phys. Rev.* **A 36**, 2384 (1987).
13. P. Schaaf, J. Talbot, H. M. Rabeony and H. Reiss, *J. Phys. Chem.* **92**, 4826 (1988).
14. P. Nielaba, V. Privman and J. S. Wang, *J. Phys.* **A 23**, L1187 (1990), and *Phys. Rev.* **B 43**, 3366 (1991).
15. J. D. Sherwood, *J. Phys.* **A 23**, 2827 (1990).
16. S. S. Manna and N. M. Švrakić, *J. Phys.* **A 24**, L671 (1991).
17. D. Milošević and N. M. Švrakić, *J. Phys.* **A 26**, L1061 (1993).
18. Lj. Budinski-Petković and U. Kozmidis-Luburić, *Physica* **A 236**, 211 (1997).
19. Lj. Budinski-Petković and U. Kozmidis-Luburić, *Physica* **A 245**, 261 (1997).
20. S. Caser and H. J. Hilhorst, *J. Phys. A: Math. Gen.* **27**, 7969 (1994).
21. Lj. Budinski-Petković and U. Kozmidis-Luburić, *Phys. Rev.* **E 56**, 6904 (1997).

Fiber-Optical Compressor Based on Consequent Using of Fiber of Positive and Negative Dispersion

N. I. Kaymakanova, L. M. Ivanov*, P. P. Branzalov*, L. I. Pavlov*

Plovdiv University, 24 Tzar Asen street, 4000 Plovdiv, Bulgaria

** Institute of Electronics, 72 Tzarigradsko chaussee, 1784 Sofia, Bulgaria*

Received: December 2, 1999

Abstract

A simple all-optical fiber compressor, based on an idea of dispersion management using a fiber of positive dispersion in the first part and of negative dispersion in the second one at the working wavelength, is investigated. The method allows a combination of the advantages of the classic fiber-grating and of the multisoliton compression. It is possible to improve substantially the quality of the compressed pulse compared to the multisoliton compression. The compression factor could be increased up to 2-2.5 times when the fraction of the input pulse energy appearing within the compressed pulse enhances more than 2 times. Thus, the peak power of the compressed pulse is able to increase about 5 times and the quality of the obtained pulses should be comparable with those obtained by the fiber-grating compressor.

Key words: Laser pulse compression, optical fiber, dispersion of light

1. Introduction

Fiber-optical methods are one of the most powerful techniques for laser pulse compression. So-called "fiber-grating compressor" is used within the spectral range of positive dispersion of the group velocity in quartz fibers. The input pulses are first spectrally broadened when passing through an optical waveguide with a positive velocity dispersion of the quartz fiber, as a result of the self phase modulation. After that, the pulse is compressed up to the time duration determined by its spectral bandwidth by pair gratings which consist of an optical line of negative dispersion. The method is quite efficient [1,2] and it allows obtaining of pulses without a pedestal because of the possibility to realize linear chirp J practically over the entire pulse duration. The main disadvantage is namely the pulse passing through two qualitatively different optical media which complicates its practical realization.

The method of "multisoliton compression" [1,3] is used within the range of negative dispersion of the group velocity and the compression is performed due to the mutual influence of the self-phase modulation and of the negative dispersion of the fiber. The disadvantage of this method is the appearance of a broad pedestal, where most of the energy is concentrated. In that, the energy within the pedestal grows with the enhancement

of the input pulse energy. The reason for that is that the chirp is linear only within the central part of the pulse and as a result only a small part of the full energy remains within the compressed pulse and the other goes to the pedestal.

Contemporary progress in technology and performances of fibers, especially of fibers with a shifted dispersion allows the production a fiber of positive as well as of negative dispersion at the same fixed wavelength (for example $\lambda = 1.4 \mu\text{m}$) [1].

Such a combination of both techniques was first applied in [4] and then improved in [5,6], where the pulse is first compressed by a fiber-grating compressor in an up-shifted fiber and after that the same is additionally compressed by the multisoliton compression in a dispersion down-shifted fiber. This technique allows a higher degree of compression (up to 5000 times) but it is complicated for realization and the obtained pulses are of very bad quality. The possibility of one after another use of fibers with positive and negative dispersion for a fixed wavelength is shown and experimentally demonstrated for the first time in [7].

Recently, the idea of using an optical waveguide of positive as well as of negative dispersion is broadly applicable in order to realize the so-called "dispersion management" in optical communication lines, i.e. a compensation of the dispersion pulse broadening is possible.

In this paper we consequently apply fibers of positive and negative dispersion in order to compress the pulses of energy exceeding essentially that of the fundamental soliton. As a matter of fact, this is a combination of both methods: the fiber grating compressor and the 0 multisoliton compression. Thus, the compression degree increases up to 2-3 times and the pulse quality improves substantially, when more than half of the energy from the pedestal is transferred to the compressed pulse. Such scheme realization is simpler, which allows its application in the production of solid-state lasers with $a \sim 20$ times compression.

2. Model

Analysis of the nonlinear dynamics of the pulse propagation in single mode optical fibers is performed by the standard split-step Fourier method in numerical solving of the nonlinear Schrodinger equation [8]. It is taken into account that the dispersion for both fibers differs by its module and not only by the sign. Normalization is made concerning the initial pulse parameters and the dispersion module of the second fiber which is of negative dispersion. We should note that the effects of cubic dispersion, self-steepening and the delayed nonlinear response in optical fibers are neglected, since we assume that the interaction is far from the zero dispersion point, and a compression of relatively long pulses ($\sim 50 - 100$ ps) is realized which is typical for solid-state cw lasers. As a results, we will write the equation for an evolution of temporal and of frequency pulse parameters in the first fiber:

$$i \frac{du}{d\xi} - \beta^* \frac{1}{2} \frac{d^2u}{d\tau^2} + |u|^2 u = 0 \quad (1)$$

Also, for the second optical waveguide we have

$$i \frac{du}{d\xi} + \frac{1}{2} \frac{d^2u}{d\tau^2} + |u|^2 u = 0, \quad (2)$$

where

$$u = \sqrt{\frac{\gamma\tau_0^2}{|\beta_2^-|}}A; \quad \xi = \frac{z}{L_D}; \quad L_D = \frac{\tau_0^2}{|\beta_2^-|}; \quad \tau = \frac{t - z/v_g}{\tau_0}; \quad \beta^* = \frac{|\beta_2^+|^*}{|\beta_2^-|}; \quad (3)$$

Here A is the slowly varying amplitude of the pulse envelope, γ is the coefficient of nonlinearity, τ_0 is the initial pulse width, β_2^+ , β_2^- are group velocity dispersion parameters in the first and second fiber respectively, L_D is the dispersion length, v_g is the group velocity.

Such manner of normalization of the equation allows easier comparison of the compression quality for one and the same pulse using either the multisoliton compression or the method proposed in this paper. We neglect the optical losses in both fibers. Besides, we assume that the transition between both fibers is realized without any changes of the transverse size of the radiation.

The initial pulse shape is assumed to be $u(0, \tau) = N \operatorname{sech}(\tau)$. If N - the soliton's number is an integer, the last expression is the precise solution of the nonlinear Schrodinger equation. Our research is done till $N < 15$. Such an expression of the shape allows us to compare our obtained results with those from multisoliton compression studied by other authors. The case of $N \leq 15$ is also analyzed in order to avoid the appearance of the effect of modulation instability in a fiber of negative dispersion [9], since such an effect is not taken into account in equations we use. We should note, that the pulse shape $\operatorname{sech}(\tau)$ and the integer N are not obvious for the proposed method, since such a technique allows a pulse compression of arbitrary shape (for example a Gaussian or Lorentz shape), whose amplitude and duration do not correspond to the integer number of solitons. The expressions by $\operatorname{sech}(\tau)$ and the N integer are used only because of comparison of our results obtained by the proposed method with those following the method of multisoliton compression.

3. Results

Several configurations of various ratios of the dispersion module of both fibers $\beta^* = 1.25, 1.00, 0.75$ and 0.50 , are investigated. The quality of the compressed pulse is determined by the compression factor and the quality factor. The compression factor $F_c = T_0/T_{comp}$, where T_0 and T_{comp} are the full width at half maximum (FWHM) measured to the impulse intensity of the initial as well as of the compressed pulse. The quality factor Q_c is defined as a fraction of the input pulse energy appearing in the compressed pulse.

In order to optimize the compression in every version (we fix the pulse energy and the dispersion of the first fiber), we vary the length of the first part which is of positive dispersion and we determine the second length which gives a maximum compression degree. The results of numerical modeling show that we can approximate the optimal length of the first part of the fiber as $z_{opt} = 0.46L_D/N$. At such a length of the fiber with positive dispersion and optimizing the fiber's length with negative dispersion, we achieve the highest quality dispersion. This result substantially differs from the optical length of the fiber usable in the "fiber grating compressor" which gives $z_{opt} = 2.5L_D/N$. This fact leads to less spectral broadening and to an essentially smoother temporal pulse shape compared to the case of the fiber-grating compressor. Probably this is connected with a substantial difference between our proposed method and the fiber grating compressor. As a distinction of the pair diffraction gratings, the fiber of negative dispersion is an

essentially nonlinear medium and there is a strong nonlinear impact on the pulse, besides the compression. The edges of the spectrally-broadened pulse are steep and they lead to strong fluctuations, due to the nonlinearity during compression, and to the worse quality of this process.

We also studied the variation of the optimal length of the second fiber when the first fiber length is optimized and this allows achievement of the most qualitative compression. The results show that when fixing the number of solitons N , the second fiber length z_D depends weakly on the ratio of both fiber dispersions. For example at $N = 10$, the $z_{2,opt}/z_D = 8.7 - 9.7$ when β^* changes from 1.25 to 0.5. We can explain such a weak dependence as follows. If $L = z_{opt}$ in the first fiber and the energy (the number N of solitons) is fixed, then the pulses obtain one and the same frequency broadening which does not depend on the dispersion. This determines the same dynamics of propagation through the fiber of negative dispersion, and as a result its optimal length depends weakly on the dispersion of the first fiber.

Advantages of the studied method are shown by comparison of the compression dynamics for the 10-soliton pulse at $\beta^* = 1.25$ (Fig. 1a) with the compression dynamics of the 10-soliton pulse for the multisoliton compression (Fig. 1b). It is evident that the pulse in the first fiber acquires a nearly rectangular shape. This is due to the spectral broadening and to the linearization of the chirp of the whole pulse. We do not give results

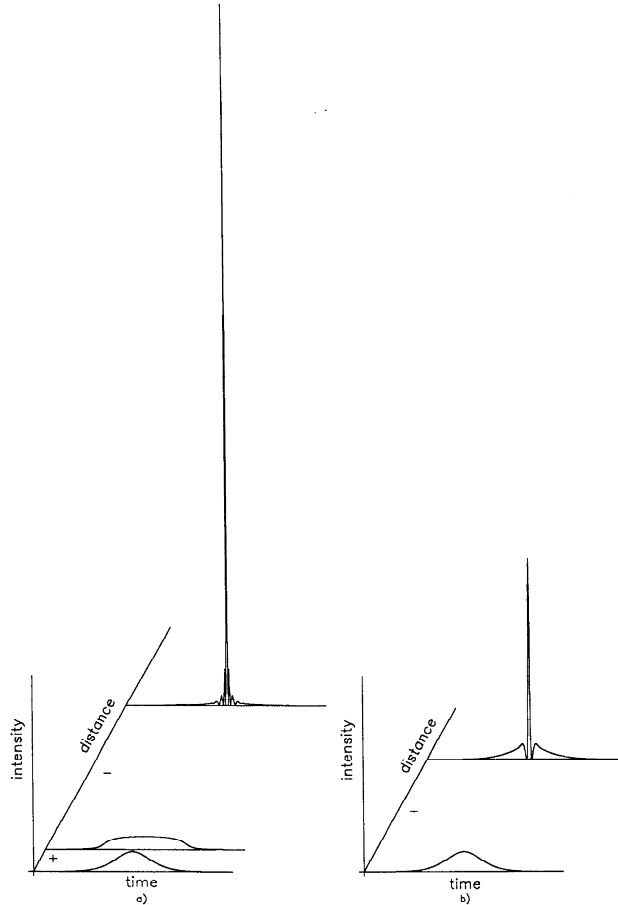


Figure 1. Compression dynamics for the 10-soliton pulse following the here proposed method (a) and the multisoliton compression (b).

from the spectral dynamics study, since they are not new compared to the well known effect of phase self-modulation in a fiber of positive dispersion. When the chirped and spectrally broadened pulse passes through the fiber of negative dispersion, it compresses much more with great quality compared to the case of multisoliton compression. The improving of the compression degree and the introducing of more energy within the compressed pulse leads to a substantial increase of the peak power, which in particular is nearly five times greater when compared to the multisoliton compression.

Results for a dependence of the F_c compression degree versus the soliton number and the dispersion ratio module for both pieces of fibers, are given in Fig. 2. Enhancement of the compression degree is achieved more than 2 times compared to the multisoliton compression (curve 5 in Fig. 2). As an example for 10-soliton pulse, the compression degree is: 74 at $\beta^* = 1.25$, 78 at $\beta^* = 1$ and 88 at $\beta^* = 0.75$, when the multisoliton compression gives only 38. We should also note the increase of the compression degree with the growth of the soliton number and with the β^* reduction. Anomalous behavior takes place at high values of N . We can obtain a sharp reduction of the compression degree with the increase of the pulse energy. Such a reduction appears, as earlier, as smaller in value for β^* . The explanation is connected with the fact that for small values of β^* and N , the model is close to the model of the fiber-grating compressor because of stronger impact of the dispersion than that of the nonlinearity. For fixed β^* at the high soliton number, the nonlinearity becomes essential and its influence is comparable with that of the dispersion, then, the model is closer to the model of multisoliton compression. Nevertheless, we think that the clarification of this problem needs some further studies.

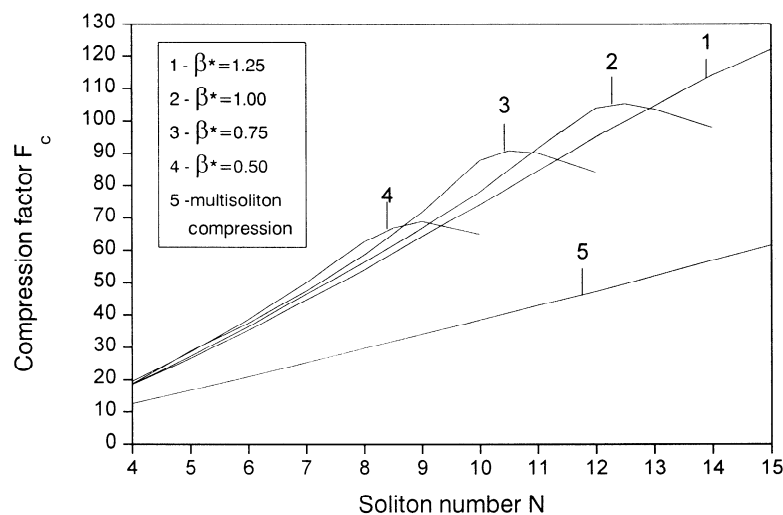


Figure 2. Compression factor F_c versus the soliton number corresponding to: 1,2,3,4 according to our proposed method with $\beta^* = 1.25$, $\beta^* = 1$, $\beta^* = 0.75$, $\beta^* = 0.5$, 5 - multisoliton compression.

Results for a variation of the quality factor Q_c depending on the soliton number and the ratio of dispersion modules of both pieces of fibers, are given in Fig. 3. We obtain substantial increase of the pulse energy compared with the multisoliton compression (curve 5 in Fig. 3) and the results are improved with the soliton number increase and with the growth of the dispersion module in the second fiber. As an example, the energy of the compressed pulse is only 30% of the input pulse energy for the pure multisoliton

compression at $N = 10$, while our method gives 53% for the compressed pulse energy at $\beta^* = 1.25$, 56% for $\beta^* = 1$, 64% at $\beta^* = 0.75$. Thus, about a 2 times improvement of the compressed pulse quality is demonstrated. The deviation from this dependence is observed at a great soliton number and at small β^* values. Anomalous behavior is obtained exactly at the same values of N , when it appears, if taking into account the compression degree. The reason is the same as for the variation of the compression degree versus N and β^* . In order to avoid the anomalous behavior, we should choose the second fiber of greater dispersion.

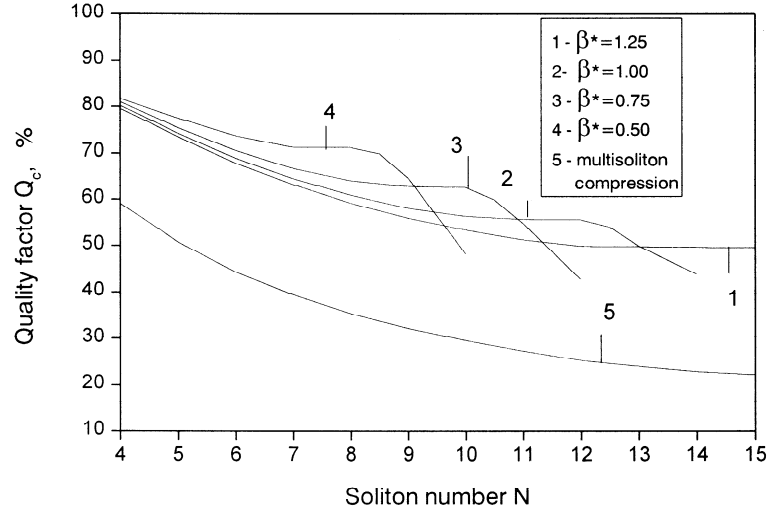


Figure 3. Quality factor Q_c versus the soliton number corresponding to: 1,2,3,4 according to our proposed method with $\beta^* = 1.25$, $\beta^* = 1$, $\beta^* = 0.75$, $\beta^* = 0.5$, 5 - multisoliton compression.

4. Conclusion

A scheme of optical pulse compression is investigated when it is based on an idea of the "dispersion management" i.e. on the consequent using of a fiber of positive and of negative dispersion. This all-optical fiber compressor combines the advantages of the classic fiber-grating compressor and of multisoliton compression. Such a scheme allows an improvement of the compression degree as well as of the quality factor. This improvement depends on the soliton number of the input pulse as well as the dispersion of the used fibers. Thus, we have obtained about a 2.5 times increase of the compression degree compared with the multisoliton compression and more than double increase of the percent-content of the compressed pulse energy. As a result, we achieve a more than about 5 times growth of the peak power of the compressed pulse compared to the classic multisoliton compression.

The proposed method is suitable for pulse compression within the spectral range 1.3 – 1.5 μm , where, using one and the same material, we are able to produce a fiber of positive or negative dispersion only by change of the optical waveguide diameter.

Acknowledgments

This study was done under contract F-807 of the National Foundation of the Bulgarian Ministry of Education and Technology.

References

1. Govind P. Agrawal, *Nonlinear fiber optics*, 2nd ed. (Academic press, San Diego, 1995).
2. R. L. Fork, C. H. Brito Cruz, P. C. Becker and C. V. Shank, *Opt. Lett.* **12**, 483 (1987).
3. L. F. Mollenauer, R. H. Stolen, J. P. Gordon and W. J. Tomlinson, *Opt. Lett.* **8**, 289 (1983).
4. K. Tai and A. Tomita, *Appl. Phys. Lett.* **48**, 1033 (1986).
5. A. S. Gouveia-Neto, A. S. L. Gomes, J. R. Taylor, *Opt. Lett.* **12**, 395 (1987).
6. A. S. Gouveia-Neto, A. S. L. Gomes, J. R. Taylor, *J. Mod. Opt.* **35**, 7 (1988).
7. K. J. Blow, N. J. Doran, B. P. Nelson, *Opt. Lett.* **10**, 393 (1985).
8. R. H. Fisher and W. K. Bischel, *Appl. Phys. Lett.* **23**, 661 (1973).
9. A. Hasegawa and Brinkman, *IEEE J. Quantum Electron.* **QE-16**, 694 (1980).

The Possibility of Phase Transition Temperature Shift in Some Ferroelectric Liquid Crystalline Mixtures

D. Ž. Obadović¹, A. Vajda², M. Stančić³, K. Fodor-Csorba² and L. Bata²

¹*Institute of Physics, Faculty of Sciences, Trg D. Obradovića 4, Novi Sad, Yugoslavia*

²*Res. Inst. for Solid State Physics and Optics of the Hungarian Academy of Sciences, H-1525 Budapest, P.O.B.49, Hungary*

³*High Technical School, Dj. Stratimirovića 23, Zrenjanin, Yugoslavia*

E-mail: obadovic@unsim.ns.ac.yu

Received: May 31, 2000

Abstract

The article describes a study of the possibility of phase transition temperature shift in binary mixtures of *4'-n-heptyloxyphenyl-4-n-octyloxy benzoate* and *4'-n-pentylphenyl-4-n-decyloxy thiobenzoate*. Using the method of optical microscopy, it was established that the phase transition temperatures of binary mixtures are shifted significantly towards the lower temperatures with respect to their components. The mixtures exhibited smectic C and smectic G phase in a broader temperature range than that of the individual compounds. We have identified the presence of enantiotropic smectic G and smectic C phase close to room temperature. X-ray diffraction data of non-oriented samples have enabled the characterization of the structure and calculation of the molecular parameters: the layer spacings (d) and the average intermolecular distances (D) in N, SmA, SmC, and SmG phases.

Key words: New ferroelectric mixture, phase transition, X-ray diffraction, molecular parameters.

1. Introduction

The peculiarities of the molecular arrangement in the mesophase of ferroelectric mixtures have been studied intensively by various authors [1,2]. In these mixtures smectic G (SmG), smectic C (SmC), smectic A (SmA), nematic N (N) and isotropic (I) phase sequence is preferable.

In this paper we have investigated binary mixtures of *4'-n-heptyloxyphenyl-4-n-octyloxy benzoate* (Comp. 1) with *4'-n-pentylphenyl-4-n-decyloxy thiobenzoate* (Comp. 2). The molecular structures of the investigated compounds are given in Figure 1:

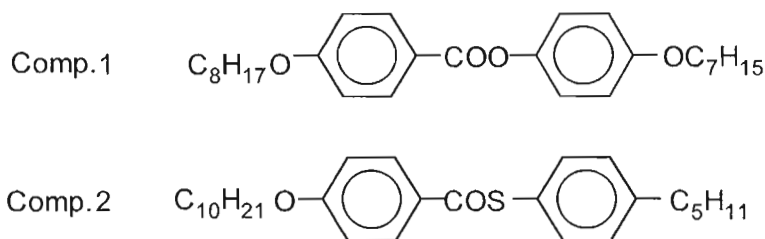


Figure 1. The molecular structures of the investigated compounds.

The phase sequences of investigated substances are given in Table 1. The addition of *Comp. 1* to *Comp. 2* in different concentrations resulted in the formation of liquid crystal mixtures (*Mix. 1* and *Mix. 2*) with the SmC phase in a wide temperature range (77°C - room temperature) and in *Mix. 1* with the enantiotropic SmG phase. In both of the mixtures, a shift of the temperature of the phase transition N → SmA by 3 – 6°C was noticed. The synthesis of the investigated compounds was reported in [3,4].

Table 1. The phase sequence of investigated substances.

Substances	Phase sequence (°C)	Concentration Wt (%)	
		<i>Comp. 1</i>	<i>Comp. 2</i>
<i>Comp. 1</i>	I 85 N 82 SmA 65 SmC 50 SmG 30 Cr	100	
<i>Comp. 2</i>	Cr 65.5 SmA 82 N 85 I		100
<i>Mix. 1</i>	I 82.5 N 78.1 SmA 64.7 SmC 47 SmG 24 Cr	40	60
<i>Mix. 2</i>	I 85.4 N 83 SmA 77 SmC 24 Cr	50	50

The phase transition temperatures determined by polarization microscopy were the basis for the investigation of unoriented samples by X-ray diffraction. The detailed structural studies of these mixtures allowed the determination of the molecular arrangement, conformation and packing as well as the molecular parameters: average lateral distance between the long axes of neighbouring parallel molecules (D) and the thickness of smectic layer (d). The calculation of these values was performed using the Bragg law: $n\lambda = 2x\sin\theta$, where $x = d$ and D respectively.

2. Experimental

The optical study was performed using a polarization microscope Carl Zeiss (Jena) in the transparent light with a special additional facility for the controlled heating and cooling of the sample, Mettler FP 5.

Unoriented samples were investigated by X-ray diffraction in a transmission geometry by means of a conventional powder diffractometer, Seifert V-14, $\text{CuK}\alpha$ radiation at 0.154 nm, with an automatical high temperature kit Paar HTK-10.

3. Results and discussion

X-ray diffraction studies were carried out on the investigated mixtures in all phases they exhibited. Figure 2 and 3 show the X-ray diagrams of the non-oriented sample as

a function of the temperature. In the case of *Mix. 1* at the transition of the nematic (N) into the smectic A (SmA) phase, besides the diffuse outer scattering ($2\theta \sim 17.7^\circ$) a strong reflection of small angles ($2\theta \sim 2.7^\circ$) appears, indicating the layer structure. Below 64.7°C the position of the strong reflection at a small diffraction angle is somewhat shifted to the highest angle, and here the small diffraction peak also appears at 5.7° , indicating the SmC layer structure. The transition SmA \rightarrow SmC is connected with a small jump in the layer thickness. Smectic G phase was characterized by an additional strong peak at ($2\theta \sim 20.3^\circ$). That peak corresponds to the hexagonal molecular packing of the centres of mass of the molecules along the smectic layers.

In the case of *Mix. 2* the calculation of average intermolecular distance between the long axes of the neighbouring parallel molecules for the isotropic (I) and nematic (N) phase indicates highest packing density of the molecules in the nematic phase, giving the value $D = 4.79 \text{ \AA}$, 4.66 \AA respectively. The SmA phase of *Mix. 2* appearing at 83°C is characterized by two small angle diffraction peaks (2.7° and 3.5°) and by the broad diffuse peak at larger angles (Fig. 3, Table 2). The calculation of effective layer thickness d , on the basis of the 2θ values by the small angle value of 32.68 \AA and the other one by the large angle gave the values of the lateral intermolecular spacing $D = 4.81 \text{ \AA}$.

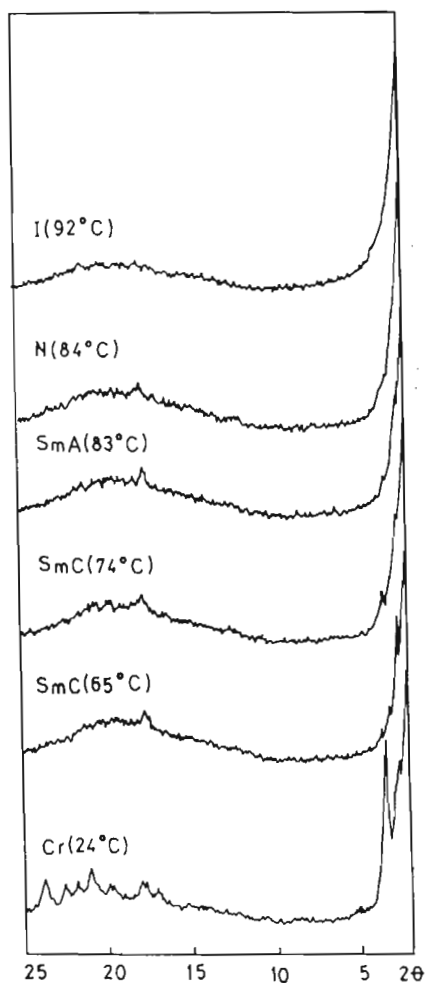
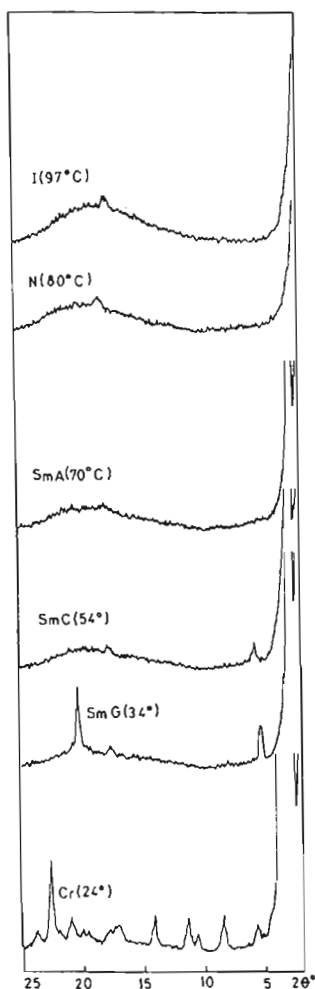


Figure 2. X-ray diffraction profiles for *Mix.1*.

Figure 3. X-ray diffraction profiles for *Mix.2*.

The SmC phase appeared in the wide temperature range 77 – 24°C on cooling. If we assume that $d \sim l$ (length of the molecule) in the SmA phase and the calculated value $d(\text{SmC}) = 32.68 \text{ \AA}$, then considering that $d = l \cos \beta$, where β is the tilt angle of the molecule with respect to the layer plane, we have $\beta = 10.9^\circ$ in the case of *Mix. 2* and also in the case of *Mix. 1*. In the SmC phase of both binary mixtures the diffraction pattern at small angles shows the presence of some clearly pronounced peaks, where the first one characterized the width of smectic layers d and the other depending on the temperature dependent flexibility of the spacers and the packing of the terminal alkyl chains of the molecules. The high percentage of *Comp. 2* in *Mix. 1* caused the appearance of enantiotropic the SmG phase stabilizing its existence. The temperature range of the SmC phase in *Mix. 2* is larger compared to the temperature range of the SmC in *Mix. 1*. Mixtures have shortened the N phase, compared to the original compounds.

Table 2. Molecular parameters of investigated mixtures.

Mixture	t (°C)	2 θ	d (Å)	δ_d (Å)	D (Å)	δ_D (Å)
<i>Mix. 1</i>	97 (I)	18.8			4.714	0.002
	80 (N)	3.9	22.63	0.06		
		18.6		4.765	0.003	
	70 (SmA)	2.7	32.68	0.09		
		17.7			5.055	0.003
	54 (SmC)	2.75	32.09	0.09		
		5.7	15.49	0.03		
	34 (SmG)	17.6			5.033	0.003
		2.6	33.94	0.13		
		5.3	16.65	0.03		
<i>Mix. 2</i>	92 (I)	20.3			4.37	0.002
		18.5			4.790	0.003
	84 (N)	3.25	27.15	0.08		
		19.0			4.665	0.002
	83 (SmA)	2.7	32.68	0.09		
		3.5	25.21	0.07		
		18.4			4.816	0.003
	74 (SmC) ^a	2.75	32.09	0.09		
		3.4	25.96	0.03		
	65 (SmC)	17.8			4.977	0.003
2.75		32.68	0.09			
3.25		27.15	0.08			
3.7		23.85	0.06			
		17.65			5.019	0.003

^ahomeotropic

4. Conclusion

We have performed optical microscopy and X-ray diffraction investigations on the crystalline powder of unoriented samples of binary mixtures *Mix. 1* and *Mix. 2* composed of *Comp. 1* and *Comp. 2*. We have concluded that the higher concentration of *Comp. 2* in

Mix. 1 caused the appearance of the enantiotropic SmG phase having a stabilizing effect on this phase, and shifted the temperature transition of the SmC \rightarrow SmG phase to the lower temperature. The temperature range of the SmC phase in Mix. 2 is larger compared to the temperature range SmC in Mix. 1. The tilt angle in the SmC phase was calculated by equation $\beta = \arccos d/l$ and we found $\beta = 10.9^\circ$ for Mix. 1 and Mix. 2. The intermolecular distance D for all investigated substances increased with the rise of temperature, which means the decrease of the packing density of the molecules perpendicular to the long axes.

References

1. R. Dabrowski, J. Szulc and B. Sosnovska, *Mol. Cryst. Liq. Cryst.* **215**, 13 (1991).
2. A. Fukuda, Y. Takanishi, T. Isozaki, K. Ishikawa and H. Takezoe, *J. Mater. Chem.* **4**, 997 (1994).
3. D. Ž. Obadović, L. Bata, K. Fodor-Csorba, A. Vajda and T. Tóth-Katona, *Rev. Res. Fac. Sci. Univ. of Novi Sad*, **26**, 47 (1996).
4. D. Ž. Obadović, L. Bata, T. Tóth-Katona, A. Bóta, K. Fodor-Csorba, A. Vajda and M. Stančić, *Mol. Cryst. Liq. Cryst.* **303**, 85 (1997).

Considerations Concerning the Pseudoharmonic Oscillator Model

Dušan Popov

*University "Politehnica" of Timișoara, Department of Physics,
Piața Regina Maria No.1, Of. Postal 5, 1900 Timișoara, Romania
E-mail: dpopov@etv.utt.ro, dpopov@edison.et.utt.ro*

Received: April 5, 2001

Abstract

Even if the harmonic oscillator potential has its advantages, it is unrealistic in several aspects, when compared to the real interaction potentials involved in the many branches of physics. As an intermediate potential between the harmonic (an "ideal" potential) and the anharmonic potentials, in the present article we deal with the so-called "pseudoharmonic potential". We have calculated the expected values of some thermodynamical functions, which characterize the quantum ideal gas of pseudoharmonical oscillators and some thermal moments of the internuclear distance, generally and for two approximations related to the internuclear distance r_0 .

Key words: Pseudoharmonic oscillator, thermal average, Hellmann-Feynman

1. Introduction

In many branches of physics, even if the harmonic oscillator (HO) potential certainly has its advantages and applications, it is unrealistic in several aspects. First, the HO potential is used for its mathematical solvability, i.e. it allows the exact mathematical solution of the Schrödinger equation. When compared to the real interaction potentials involved e.g. in diatomic molecule physics, then these disadvantages become more evident. The HO potential is a good theoretical model, but comparison with the experimental spectroscopic data shows that this model is often unsatisfactory, because many properties of real physical systems are not harmonical but anharmonical. So, it is necessary to use one of the anharmonic potentials.

As an intermediate potential between the HO potential (an "ideal" potential) and the anharmonic potentials (such as the Morse potential, the more "realistic" potential), in the present article we deal with the so-called *pseudoharmonic oscillator* (PHO) potential.

We consider that the physical system is a quantum ideal gas of the diatomic molecules, which fulfil the conditions of the quantum canonical distribution. The PHO potential, which describes the molecular vibrations, is a spherically symmetric potential, with the effective potential defined as in Ref.[1]:

$$V_J^{(p)}(r) = \frac{m\omega^2}{8}r_0^2 \left(\frac{r}{r_0} - \frac{r_0}{r} \right)^2 + \frac{\hbar^2}{2m} \frac{J(J+1)}{r^2}, \quad (1)$$

where r_0 is the equilibrium distance between the nuclei of the diatomic molecule.

This potential admits, also, the exact analytical solution for the Schrödinger equation and this is one of the reasons we deal with it. The radial eigenfunctions and eigenvalues have been calculated in Ref.[1] and the final expressions are:

$$R_{vJ}^{(p)}(r) \equiv \frac{1}{r} u_v^\alpha(r) = \left[\frac{B^3 v!}{2^\alpha \Gamma(\alpha + v + 1)} \right]^{\frac{1}{2}} (Br)^{\alpha - \frac{1}{2}} \exp\left(-\frac{B^2}{4} r^2\right) L_v^\alpha\left(\frac{B^2}{2} r^2\right), \quad (2)$$

$$E_{vJ}^{(p)} = \hbar\omega \left(v + \frac{1}{2}\right) + \frac{\hbar\omega}{2} \alpha - \frac{m\omega^2}{4} r_0^2 \equiv \hbar\omega v + E_0, \quad (3)$$

where v and J are the vibrational and the rotational quantum numbers. We observe that the vibrational and the rotational degrees of freedom are uncoupled, which offers some mathematical advantages in the calculations related to the PHO potential. This will become more evident in the next sections. Also, we have used the notations:

$$B = \left(\frac{m\omega}{\hbar}\right)^{\frac{1}{2}}; \quad \alpha = \left[\left(J + \frac{1}{2}\right)^2 + \left(\frac{m\omega}{2\hbar} r_0^2\right)^2 \right]^{\frac{1}{2}}. \quad (4)$$

2. Density matrix

In Ref.[2] we have deduced the expression for the whole (total) density matrix for PHO in the position representation:

$$\rho^{(p)}(\vec{r}, \vec{r}'; \beta) = \frac{1}{4\pi} \sum_{J=0}^{\infty} (2J+1) P_J(\cos \gamma) \rho_J^{(p)}(r, r'; \beta), \quad (5)$$

where $P_J(\cos \gamma)$ is the Legendre polynomial and γ - the angle between the vectors \vec{r} and \vec{r}' .

The radial density matrix in the position representation $\rho_J^{(p)}(r, r'; \beta)$ was deduced as the solution of the Bloch equation and it is [2]:

$$\begin{aligned} \rho_J^{(p)}(r, r'; \beta) &= \exp\left(\beta \frac{m\omega^2}{4} r_0^2\right) \frac{m\omega}{2\hbar} \frac{1}{\sinh \beta \frac{\hbar\omega}{2}} \times \\ &\times \frac{1}{(rr')^{\frac{1}{2}}} \exp\left[-\frac{m\omega}{4\hbar} (r^2 + r'^2) \coth \beta \frac{\hbar\omega}{2}\right] I_\alpha\left(\frac{m\omega}{2\hbar} \frac{1}{\sinh \beta \frac{\hbar\omega}{2}} rr'\right), \end{aligned} \quad (6)$$

where $I_\alpha(x)$ is the modified Bessel function.

The trace of the whole density matrix is the whole partition function:

$$Z^{(p)}(\beta) = \int d\vec{r} \rho^{(p)}(\vec{r}, \vec{r}; \beta) = \sum_{J=0}^{\infty} (2J+1) Z_J^{(p)}(\beta), \quad (7)$$

while the trace of the radial density matrix is the rotational partition function:

$$Z_J^{(p)}(\beta) = \int_0^\infty dr r^2 \rho_J^{(p)}(r, r; \beta) = \frac{1}{2 \sinh y} e^{\beta \frac{m\omega}{4} r_0^2} e^{-\beta \frac{\hbar\omega}{2} \alpha}. \quad (8)$$

Finally, we obtain:

$$Z^{(p)}(\beta) = \frac{1}{2 \sinh y} e^{\beta \frac{m\omega}{4} r_0^2} T_\alpha(y), \quad (9)$$

where we have used the following notations:

$$y = \beta \frac{\hbar\omega}{2}; \quad T_\alpha(y) = \sum_{J=0}^{\infty} (2J+1) e^{-y\alpha}. \quad (10)$$

The partition function $Z^{(p)}(\beta)$ is a quantity of maximal informational importance because, by means of the partition function, it is possible to express all the characteristic observables of the PHO quantum gas.

So, the internal energy of the system of quantum PHO gas is:

$$U_{syst}^{(p)} = NU^{(p)} = -N \frac{\partial}{\partial \beta} \ln Z^{(p)} = -N \frac{m\omega^2}{4} r_0^2 + N \frac{\hbar\omega}{2} \left[\coth y - \frac{\partial}{\partial y} (\ln T_\alpha) \right], \quad (11)$$

where N is the whole number of the PHO in the quantum gas.

Using the expression of the internal energy, the specific heat for one mole (i.e. the molar heat capacity) of the PHO-s quantum ideal gas is:

$$C_V^{(p)} = \frac{1}{\nu} \frac{\partial U_{syst}^{(p)}}{\partial T} = N_A \frac{\partial U^{(p)}}{\partial T} = -R\beta^2 \frac{\partial U^{(p)}}{\partial \beta}. \quad (12)$$

For the PHO-s system, it is useful to write this expression with respect to the variable y and, then, it becomes:

$$\frac{C_V^{(p)}}{R} = \left(\frac{y}{\sinh y} \right)^2 + \frac{\hbar\omega}{2} \beta^2 \frac{\partial^2}{\partial \beta \partial y} (\ln T_\alpha) = \left(\frac{y}{\sinh y} \right)^2 + y^2 \frac{\partial^2}{\partial y^2} (\ln T_\alpha). \quad (13)$$

On the other hand, the free energy of the PHO quantum gas, which corresponds to one molecule (one PHO) is:

$$F^{(p)} = -\frac{1}{\beta} \ln Z^{(p)} = -\frac{1}{\beta} \ln \frac{1}{2 \sinh y} - \frac{m\omega^2}{4} r_0^2 - \frac{1}{\beta} \ln T_\alpha. \quad (14)$$

In the previous equations we have used the superscript (p) for the observables concerning the PHO, while the superscript (0) will be used for similar observables concerning the HO.

3. Quantum-statistical averages

The quantum-statistical average or the thermal average for an observable A , which characterize the quantum gas of pseudoharmonical oscillators obeying the quantum canonical distribution can be calculate as follows:

$$\begin{aligned} \langle A \rangle^{(p)} &= \frac{Tr A \rho^{(p)}}{Tr \rho^{(p)}} = \frac{1}{Z^{(p)}} \sum_{J=0}^{\infty} (2J+1) Z_J^{(p)} \langle A \rangle_J^{(p)} = \\ &= \frac{1}{T_\alpha} \sum_{J=0}^{\infty} (2J+1) e^{-y\alpha} \langle A \rangle_J^{(p)}, \end{aligned} \quad (15)$$

where we have used the corresponding expressions for the whole density matrix in the position representation and the whole partition function.

The free energy is connected with the position thermal moments, that is, with the quantum-statistical averages of the powers of displacement from the equilibrium position operator. The formalism of the moments of the spectral density distribution has already been applied in the case of spectra of oscillators coupled by kinetic terms (see, Ref.[3] and references therein), though we use here not the spectral but the thermal moments. For this reason, we consider that the free energy of the PHO-s gas is a function of some parameters \hbar, m, ω and r_0 , generically denoted by λ_i , so that:

$$dF^{(p)} = \sum_i \frac{\partial F^{(p)}}{\partial \lambda_i} d\lambda_i. \quad (16)$$

On the other hand, in Ref.[4], we have extended the quantum virial and Hellmann-Feynman theorems to the quantum-statistical averages in the case of the central field potentials. As a consequence, we have obtained the following equation involving the quantum-statistical averages:

$$\frac{\partial F^{(p)}}{\partial \lambda_i} = \left\langle \frac{\partial H^{(p)}}{\partial \lambda_i} \right\rangle = \frac{1}{2} \left(\frac{\partial}{\partial \lambda_i} \ln \frac{\hbar^2}{2m} \right) \left\langle r \frac{\partial V^{(p)}}{\partial r} \right\rangle + \left\langle \frac{\partial V^{(p)}}{\partial \lambda_i} \right\rangle. \quad (17)$$

By using Eq.(4), the effective potential of the PHO (1) can be written in the following manner:

$$V_J^{(p)}(r) = \frac{m\omega^2}{8} r^2 - \frac{m\omega^2}{4} r_0^2 + \frac{\hbar^2}{2m} \left(\alpha^2 - \frac{1}{4} \right) \frac{1}{r^2}. \quad (18)$$

After straightforward calculations, by performing the partial derivatives of the free energy expression (14) on the one hand and by applying Eq.(17) to the effective potential (18) on the other hand, we obtain successively:

$$\frac{\partial F^{(p)}}{\partial \hbar} = \frac{\omega}{2} \coth y - \frac{\omega}{2} \frac{\partial}{\partial y} T_\alpha - \frac{\omega}{2} T_\alpha^{(-1)} = \frac{m\omega^2}{4\hbar} \langle r^2 \rangle - \frac{\hbar}{m} \left(\frac{m\omega}{2\hbar} r_0^2 \right)^2 \left\langle \frac{1}{r^2} \right\rangle, \quad (19)$$

$$\frac{\partial F^{(p)}}{\partial m} = -\frac{\omega^2}{4} r_0^2 + \frac{\hbar\omega}{2m} \left(\frac{m\omega}{2\hbar} r_0^2 \right)^2 T_\alpha^{(-1)} = -\frac{\omega^2}{4} r_0^2 + \frac{\hbar^2}{m^2} \left(\frac{m\omega}{2\hbar} r_0^2 \right)^2 \left\langle \frac{1}{r^2} \right\rangle, \quad (20)$$

$$\begin{aligned} \frac{\partial F^{(p)}}{\partial \omega} &= \frac{\hbar}{2} \coth y - \frac{m\omega}{2} r_0^2 - \frac{\hbar}{2} \frac{\partial}{\partial y} T_\alpha + \frac{\hbar}{2} \left(\frac{m\omega}{2\hbar} r_0^2 \right)^2 T_\alpha^{(-1)} = \\ &= \frac{m\omega}{4} \langle r^2 \rangle - \frac{m\omega}{2} r_0^2 + \frac{\hbar^2}{m\omega} \left(\frac{m\omega}{2\hbar} r_0^2 \right)^2 \left\langle \frac{1}{r^2} \right\rangle, \end{aligned} \quad (21)$$

$$\frac{\partial F^{(p)}}{\partial r_0} = -\frac{m\omega^2}{2} r_0 + \frac{\hbar\omega}{r_0} \left(\frac{m\omega}{2\hbar} r_0^2 \right)^2 T_\alpha^{(-1)} = -\frac{m\omega^2}{2} r_0 + 2 \frac{\hbar^2}{mr_0} \left(\frac{m\omega}{2\hbar} r_0^2 \right)^2 \left\langle \frac{1}{r^2} \right\rangle, \quad (22)$$

where we have used the following notation:

$$T_\alpha^{(-1)} = \frac{1}{T_\alpha} \sum_{J=0}^{\infty} (2J+1) \frac{1}{\alpha} e^{-y\alpha}. \quad (23)$$

By combining these relations, we obtain the following quantum-statistical or thermal averages for the position variable:

$$\langle r^2 \rangle = \frac{2\hbar}{m\omega} \left(\coth y - \frac{\partial}{\partial y} \ln T_\alpha \right), \quad (24)$$

$$\left\langle \frac{1}{r^2} \right\rangle = \frac{m\omega}{2\hbar} T_\alpha^{(-1)}. \quad (25)$$

In order to verify the above obtained relations concerning the PHO we must apply the harmonic limit defined as [2]:

$$\begin{aligned} \lim_{\substack{\omega \rightarrow 2\omega_0 \\ r_0 \rightarrow 0 \\ \alpha \rightarrow J + \frac{1}{2}}} A &\equiv \lim_{HO} A = A^0, \end{aligned} \quad (26)$$

i.e. when we apply the harmonic limit to a certain observable $A^{(p)}$ concerning the PHO, if the relation is proper, we must obtain the corresponding observable $A^{(0)}$ concerning the HO-3D (the 3-dimensional isotropic harmonic oscillator) which has the frequency ω_0 .

Before performing this limiting operation, it is useful to point out the harmonic limit for the following expressions, which are obtained after straightforward calculations:

$$\lim_{HO} T_\alpha = T_{J+\frac{1}{2}} = \frac{1}{2} \frac{1}{\sinh^2 \beta \frac{\hbar\omega_0}{2}} \cosh \beta \frac{\hbar\omega_0}{2}, \quad (27)$$

$$\lim_{HO} \frac{\partial}{\partial y} T_\alpha = -\coth \beta \frac{\hbar\omega_0}{2} + \frac{1}{2} \frac{1}{\coth \beta \frac{\hbar\omega_0}{2}}, \quad (28)$$

$$\lim_{HO} T_\alpha^{(-1)} = 2 \tanh \beta \frac{\hbar\omega_0}{2}. \quad (29)$$

Therefore we obtain [2]:

$$\lim_{HO} Z^{(p)} = \left(\frac{1}{2 \sinh \beta \frac{\hbar\omega_0}{2}} \right)^3 = Z^{(0)}, \quad (30)$$

$$\lim_{HO} U^{(p)} = 3N \frac{\hbar\omega_0}{2} \coth \beta \frac{\hbar\omega_0}{2} = U^{(0)}, \quad (31)$$

$$\lim_{HO} F^{(p)} = \frac{1}{\beta} \ln 2 \sinh \beta \frac{\hbar\omega_0}{2} = F^{(0)}, \quad (32)$$

$$\lim_{HO} \frac{C_V^{(p)}}{R} = 3 \left(\frac{\beta \frac{\hbar\omega_0}{2}}{\sinh \beta \frac{\hbar\omega_0}{2}} \right)^3 = \frac{C_V^{(0)}}{R}. \quad (33)$$

$$\lim_{HO} \langle r^2 \rangle = 3 \frac{\hbar}{2m\omega_0} \coth \beta \frac{\hbar\omega_0}{2} = \langle r^2 \rangle^{(0)}, \quad (34)$$

$$\lim_{HO} \left\langle \frac{1}{r^2} \right\rangle = \frac{2m\omega_0}{\hbar} \tanh \beta \frac{\hbar\omega_0}{2} = \left\langle \frac{1}{r^2} \right\rangle^{(0)}. \quad (35)$$

4. Two approximations

It is easy to observe that the sum T_α^{-1} can be written in the following manner:

$$T_\alpha^{-1} = \frac{1}{T_\alpha} \sum_{J=0}^{\infty} (2J+1) \frac{1}{\alpha} e^{-y\alpha} = \frac{1}{T_\alpha} \int_y^{\infty} T_\alpha(y) dy. \quad (36)$$

Because of the presence of an infinite series (like T_α and their derivatives), the above obtained quantum-statistical averages for the PHO can be calculated only numerically, i. e. with limited precision. So, it is useful to simplify the expression of the sum denoted by T_α , taking into account the possible values of the equilibrium distance r_0 .

We examine two approximations concerning these values: the approximation of small values of r_0 (called *m-approximation*) and the approximation of large values of r_0 (called *M-approximation*). The corresponding observables and thermal moments will be denoted by the *m*, respectively *M*-index.

In the *m*-approximation, i. e. if r_0 is small, by performing the power series development of the expression of α up to the power two, we obtain:

$$\alpha_m = \left[\left(J + \frac{1}{2} \right)^2 + C \right]^{\frac{1}{2}} \approx J + \frac{1}{2} + \frac{C}{2} \frac{1}{J + \frac{1}{2}}, \quad (37)$$

where we have denoted:

$$C = \left(\frac{m\omega}{2\hbar} r_0^2 \right)^2. \quad (38)$$

For such values of temperature T for which the variable y is small, the sum T_α can be written as the following integral:

$$T_m = 2 \sum_{J=0}^{\infty} \left(J + \frac{1}{2} \right) e^{-y\alpha_m} = 2 \int_0^{\infty} dx x e^{-yx - \frac{1}{2}yC\frac{1}{x}}, \quad (39)$$

where we have denoted $x = J + \frac{1}{2}$.

This integral is of the following kind [7]:

$$\int_0^{\infty} dx x^{\nu-1} e^{-\gamma x - \frac{\beta}{x}} = 2 \left(\frac{\beta}{\gamma} \right)^{\frac{\nu}{2}} K_\nu(2\sqrt{\beta\gamma}), \quad [\text{Re}\beta > 0, \text{Re}\gamma > 0], \quad (40)$$

where $K_\nu(z)$ is the Bessel function of the second kind. This function becomes, for $\nu > 0$ fixed and $z \rightarrow 0$ [6]:

$$K_\nu(z) \approx \frac{1}{2} \Gamma(\nu) \left(\frac{2}{z} \right)^\nu, \quad (41)$$

where $\Gamma(\nu)$ is the Euler's gamma function.

In this manner we obtain:

$$T_m = \frac{2}{y^2} \quad (42)$$

and, consequently:

$$T_m^{-1} = y. \quad (43)$$

By using these last two equations and also Eqs.(9), (11)-(14), (24) and (25), after straightforward calculations, we obtain successively:

$$Z_m = \frac{1}{y^2} \frac{1}{\sinh y} e^{y \frac{m\omega}{2\hbar} r_0^2}, \quad (44)$$

$$F_m = -\frac{m\omega^2}{4} r_0^2 + \frac{\hbar\omega}{2} \frac{1}{y} \ln \sinh y + \hbar\omega \frac{1}{y} \ln y, \quad (45)$$

$$U_m = -\frac{m\omega^2}{4} r_0^2 + \frac{\hbar\omega}{2} \left(\coth y + 2\frac{1}{y} \right), \quad (46)$$

$$\frac{C_{V;m}}{R} = \left(\frac{y}{\sinh y} \right)^2 + 2, \quad (47)$$

$$\langle r^2 \rangle_m = \frac{2\hbar}{m\omega} \left(\coth y + 2\frac{1}{y} \right), \quad (48)$$

$$\left\langle \frac{1}{r^2} \right\rangle_m = \frac{m\omega}{2\hbar} y. \quad (49)$$

The M -approximation, i.e. the case of large values of r_0 is more interesting. We can transform the expression for α from Eq.(4) and perform the power series development of the square root up to the power of order two:

$$\alpha_M = \frac{m\omega}{2\hbar} r_0^2 \left[1 + \left(\frac{J + \frac{1}{2}}{\frac{m\omega}{2\hbar} r_0^2} \right)^2 \right]^{\frac{1}{2}} \approx \frac{m\omega}{2\hbar} r_0^2 + \frac{1}{2} \left(\frac{J + \frac{1}{2}}{\frac{m\omega}{2\hbar} r_0^2} \right)^2. \quad (50)$$

In this approximation, the sum T_α becomes:

$$T_M = 2 \exp \left(-\beta \frac{m\omega^2}{4} r_0^2 \right) \sum_{J=0}^{\infty} \left(J + \frac{1}{2} \right) \exp \left[-\beta \frac{\hbar^2}{2mr_0^2} \left(J + \frac{1}{2} \right)^2 \right]. \quad (51)$$

As it is usual (see, e.g. Refs.[7], [8]), the last sum may be replaced by an integral. The motivation is simple: if we again denote $J + \frac{1}{2} = x$, then the quantity before x into the exponential (i.e. $-\beta \frac{\hbar^2}{2mr_0^2} \equiv \frac{\Theta_{rot}}{T}$, where Θ_{rot} is the rotational constant) is very small for more gases and for all temperatures for which these gases are not in the liquid state. In other words, the separation between the rotational energy levels is so small that this replacement is wholly possible. So, the last equation becomes:

$$\begin{aligned} T_M &= 2 \exp \left(-\beta \frac{m\omega^2}{4} r_0^2 \right) \int_0^{\infty} dx x \exp \left(-\beta \frac{\hbar^2}{2mr_0^2} x^2 \right) = \\ &= \frac{m\omega}{\hbar} r_0^2 \frac{1}{y} \exp \left(-y \frac{m\omega}{2\hbar} r_0^2 \right). \end{aligned} \quad (52)$$

Consequently, the sum T_M^{-1} is:

$$T_M^{-1} = \frac{1}{T_M} \int_y^{\infty} T_M(y) dy = y e^{y \frac{m\omega}{2\hbar} r_0^2} \int_y^{\infty} dy \frac{1}{y} e^{-y \frac{m\omega}{2\hbar} r_0^2}. \quad (53)$$

This integral leads to the integral exponential function ($\text{Ei}(z)$) [5]:

$$\int_x^\infty dx \frac{1}{x} e^{-ax} = -\text{Ei}(-ax), \quad (54)$$

which has the following series development [5]:

$$\begin{aligned} \text{Ei}(-z) &= e^{-z} \sum_{k=1}^n (-1)^k \frac{(k-1)!}{z^k} + R_n, \\ |R_n| &< \frac{n!}{|z|^{n+1} \cos \frac{\varphi}{2}}, \quad z = |z|e^{i\varphi}, \quad \varphi^2 < \pi^2. \end{aligned} \quad (55)$$

For the M -approximation are relevant the first two terms of the series development and so, we obtain:

$$T_M^{-1} = \frac{2\hbar}{m\omega} \left[\frac{1}{r_0^2} - \frac{1}{y} \frac{2\hbar}{m\omega} \left(\frac{1}{r_0^4} \right) + \dots \right]. \quad (56)$$

By using the above obtained expressions for T_M and T_M^{-1} , after straightforward calculations, Eqs.(9), (11)-(14), (24) and (25) lead to the following relations:

$$Z_M = \frac{m\omega}{2\hbar} r_0^2 \frac{1}{y} \frac{1}{\sinh y}, \quad (57)$$

$$F_M = \frac{\hbar\omega}{2} \frac{1}{y} \ln 2 \sinh y + \frac{\hbar\omega}{2} \frac{1}{y} \ln y + \frac{\hbar\omega}{2} \frac{1}{y} \ln \frac{\hbar}{m\omega} \frac{1}{r_0^2}, \quad (58)$$

$$U_M = \frac{\hbar\omega}{2} \left(\coth y + \frac{1}{y} \right), \quad (59)$$

$$\frac{C_{V;M}}{R} = \left(\frac{y}{\sinh y} \right)^2 + 1, \quad (60)$$

$$\langle r^2 \rangle_M = r_0^2 + \frac{2\hbar}{m\omega} \left(\coth y + \frac{1}{y} \right), \quad (61)$$

$$\left\langle \frac{1}{r^2} \right\rangle_M = \frac{1}{r_0^2} - \frac{1}{y} \frac{2\hbar}{m\omega} \frac{1}{r_0^4}. \quad (62)$$

The expression of the potential practically is the same in both representations, i.e.:

$$V_{J;m}^{(p)}(r) \approx V_{J;M}^{(p)}(r) \approx V_J^{(p)}(r), \quad (63)$$

since:

$$\alpha_m^2 \approx \alpha_M^2 \approx \alpha^2, \quad (64)$$

if we neglect the term containing $(r_0^2)^4$, respectively $(r_0^2)^{-4}$. As a consequence, the quantum-statistical averages for r^2 and r^{-2} in both approximations can be obtained also by the moment methods, i.e. by the method based on the application of hypervirial and Hellmann-Feynman theorems, in the same manner as in Section 3. This fact shows that both approximations are suitable.

This method allows the possibility also to obtain the quantum-statistical averages of the other observables which characterize the quantum system (the PHO-s quantum ideal gas). It is well known that, in these calculations, the partition function (i.e. the trace

of the density matrix) is a very important quantity because this function contains all statistical-thermodynamical information about the quantum system.

5. Conclusion

In the present article we try to present an alternative anharmonic potential confronted by the harmonic oscillator (HO) potential. This potential is the so-called pseudoharmonic oscillator (PHO) potential, which is a central field potential and a more realistic potential in comparison with the HO potential. It becomes infinite at the origin of the internuclear coordinate r and it extends only in the physical region ($0 < r < \infty$). Due to the mathematical facilities in the approach of the PHO (it admits an exact solution of the Schrödinger equation and the exact expression of the expected values), the PHO is useful, for instance, for the examination of molecular vibrations.

In the article we have calculated some thermodynamical functions, which characterize the PHO-s quantum ideal gas (i.e. partition function, free energy, internal energy, specific heat) and some thermal moments of the internuclear distance. Due to the fact that these expressions contain the infinite sum (T_α and T_α^{-1}), we have tried to obtain the corresponding expressions for two approximations: m -approximation (for small internuclear equilibrium distance r_0) and M -approximation (for large r_0). In these expressions the contribution of the anharmonicity is evinced in an analytical manner.

All these results (Eqs.(9), (11)-(14), (24) and (25)) can be obtained also if we use the density matrix in coherent states representation. It is easy to demonstrate that the PHO agrees with the Barut-Girardello coherent states. This question is the subject matter of our other article [9]. Moreover, the connection between PHO and the Barut-Girardello coherent states leads to the idea that the pseudoharmonical oscillator may have some applications in quantum optics.

References

1. M. Sage, Chem. Phys. **87**, 431 (1984).
2. D. Popov, Acta Phys. Slovaca **45**, 1557 (1995).
3. M. Banczewicz, Chem. Phys. **203**, 93 (1996).
4. D. Popov, Int. J. Quant. Chem. **69**, 159 (1998).
5. I. S. Gradshteyn, I. M. Ryzhik, *Table of Integrals, Series and Products*, (Academic Press, London, New York, 1980).
6. A. Nikiforov, V. Ouvarov, *Elements de la theorie des fonctions speciales*, (Mir, Moscou, 1976).
7. A. S. Kompaneets, *A Course of Theoretical Physics*, Vol. 2, (Mir Publishers, Moscow, 1978).
8. O. Gherman and L. Saliu, *Fizica statistica*, (Editura Tehnica, București, 1976).
9. D. Popov, J. Phys. A: Math. and Gen. **34**, 5283 (2001).

Is $\text{Sm}_3\text{Fe}_5\text{O}_{12}$ Really Cubic at Room Temperature ?

D. Rodić, M. Mitrić and R. Dimitrijević*

*Institute of Nuclear Sciences "Vinča", Laboratory of Solid State Physics, P.O.Box 522,
11001 Belgrade, Yugoslavia*

**Faculty of Mining and Geology, Djusina 6, 11000 Belgrade, Yugoslavia*

Received: May 11, 2001

Abstract

A sample of $\text{Sm}_3\text{Fe}_5\text{O}_{12}$ was sintered from corresponding mixed hydroxides that were obtained by coprecipitation of mixed nitrates. The x-ray diffraction experiment was done with monochromatized CuK_α radiation at room temperature. The sample crystallizes in the garnet structure type. The iron ions occupy both the tetrahedral and octahedral positions, while the samarium cations occupy the dodecahedral position. The refinements were done in the cubic space group $\text{Ia}\bar{3}\text{d}$ and the rhombohedral space group $\text{R}\bar{3}\text{c}$ with a hexagonal axis. Note that the group $\text{R}\bar{3}\text{c}$ is a subgroup of the symmetry group of the magnetic moment and subgroup of the $\text{Ia}\bar{3}\text{d}$ group. The transformation of the refined atomic coordinates from the group $\text{Ia}\bar{3}\text{d}$ into the group $\text{R}\bar{3}\text{c}$ gives the same values, within the sum of standard deviations, as the values obtained from the refinement in the rhombohedral space group. The Debye temperatures, obtained from thermal displacement B -factors, are 320 and 560 K from the refinements in the cubic and the rhombohedral space group, respectively. The later temperature agrees with the Debye temperature obtained by independent measurements.

Key words: Garnets, x-ray diffraction, symmetry, Debye temperature

1. Introduction

Since their discovery, magnetic garnets have played an important role in basic and applied science [1]. Their importance is based on their applicability for different magnetic media. On the other hand, these compounds are a test for Neel's theory of ferrimagnetism.

$\text{Sm}_3\text{Fe}_5\text{O}_{12}$ (SmIG) belongs to the family of rare earth magnetic garnets whose prototype is the ferrimagnetic $\text{Y}_3\text{Fe}_5\text{O}_{12}$ [1]. In the garnet structure, the space group $\text{Ia}\bar{3}\text{d}$ in the paramagnetic phase, the yttrium or rare earth ions occupy the special position 24c, with dodecahedral coordination, the iron ions occupy the special 24d sites, with tetrahedral coordination and the 16a position with octahedral coordination, and all oxygen ions are in the general 96h position [1]. The unit cell contains eight formula units.

From the theoretical point of view, there is no doubt that the garnet structure below the Curie point, about 560 K for all rare earth iron garnets (REIG) and yttrium iron garnet (YIG), can not be cubic. Namely, the existence of the ordered magnetic phase requires

a lowering of symmetry, according to the Curie principle [2]. However, the YIG and REIG structures are described in the cubic system at room temperature [3]. Only at low temperatures some REIG structures, which exhibit additional reflections in comparison with Ia3d reflections, are described in the rhombohedral space group [4]. It has been recently shown that, even if the new reflections do not appear as in the case of the YIG and yttrium aluminum iron garnet, only description in the rhombohedral space group gives the magnetic moment and Debye temperature in agreement with independent experiments [5,6].

In this work our intention is to check whether the SmIG is really cubic at room temperature. SmIG cannot be investigated by neutron diffraction, due to the giant absorption of neutrons by Sm. For that reason we have performed x-ray diffraction measurements.

2. Experimental

A powder sample of $\text{Sm}_3\text{Fe}_5\text{O}_{12}$ was sintered from corresponding mixed hydroxides that were obtained by coprecipitation of mixed nitrates. The presintering was done at temperature 950°C for 24 hours. The sample was cooled and subsequently pressed to a pressure of 1.5 t/cm^2 and refired at 1350°C for 8 hours in order to get samples of higher density.

The x-ray diffraction data for the Rietveld analysis of $\text{Sm}_3\text{Fe}_5\text{O}_{12}$ sample were collected by a Philips PW1710 powder diffractometer with graphite monochromatized $\text{CuK}\alpha$ radiation at ambient temperature. The scanning 2θ range was $9 - 135^\circ$, with the scanning time of 15 s per step and a step width of 0.02° . This experiment confirmed the garnet phase without impurities.

3. Results

The crystal structure was refined by the Rietveld profile method with the use of the Fullprof program [7]. At first the crystal reflections were indexed in the space group Ia3d. In this space group all cations occupy special positions: the yttrium ions are in the 24c positions whose local symmetry is 222, the iron ions are in the 16a and 24d positions with site symmetries -3 and -4, respectively. Only the oxygen ions in the general 96h positions, local symmetry 1, have three degrees of freedom.

The starting model for the refinement procedure was the refined crystal structure of $\text{Tb}_{2.5}\text{Y}_{0.5}\text{Fe}_5\text{O}_{12}$ [8]. The assumed peak shape corresponded to the pseudo-Voigt function.

In the last cycle of the refinement of $\text{Sm}_3\text{Fe}_5\text{O}_{12}$, total of 19 parameters were varied: one scale factor, one zero point, one mixing parameter, one asymmetry and one preferred orientation parameter, three parameters for the description of the background, three parameters for the halfwidths description and the lattice constant parameter. The atomic parameters were three free coordinates of the oxygen anion and four displacement B factors - one for each ion at four different crystallographic positions. 152 reflections were used in the refinement.

The space group R-3c was also used for the refinement. In this space group, the starting lattice constants and coordinates were obtained by transforming refined lattice parameters and coordinates from the space group Ia3d. Two hexagonal axes of the rhombohedral cell are the face diagonals of the cubic cell and the third is one half of the body diagonal. In the group R-3c, samarium ions occupy two dodecahedral 18e sites, iron ions occupy 6b

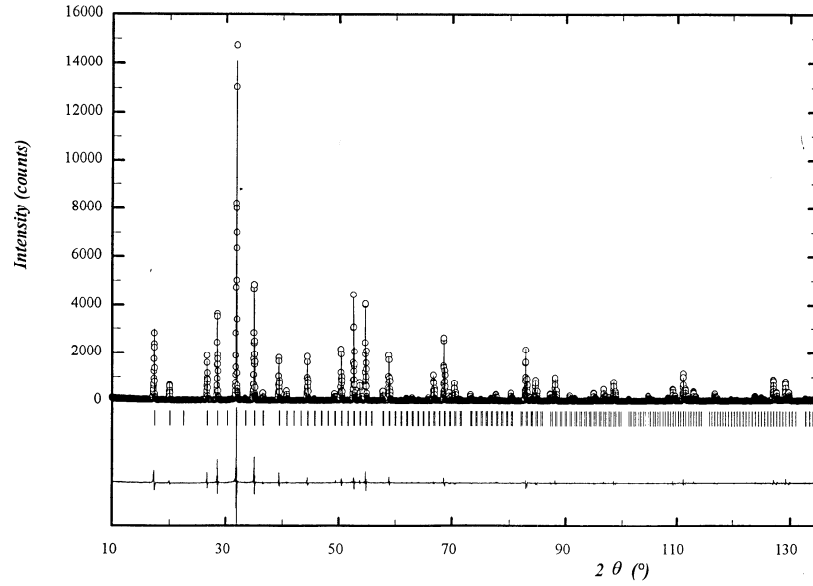


Figure 1. Observed (points) and calculated (line) x-ray diffraction pattern of $\text{Sm}_3\text{Fe}_5\text{O}_{12}$ by using space group R-3c. The line at the bottom represents the difference between observed and calculated values.

and 18d octahedral positions as well as 36f positions. The oxygen ions are in four 36f sites. In the last cycle of the refinement in this space group, a total of 32 parameters were varied: one scale factor, one zero point, one mixing parameter one asymmetry and one preferred orientation parameter, three parameters for the description of the background, three parameters for the halfwidths description and two lattice constant parameters. The atomic parameters were three free coordinates of iron in 36f positions, altogether 12 free coordinates of the oxygen anions for four oxygens in 36f sites, and four displacement B factors - one for samarium cations in dodecahedral positions, one for iron in tetrahedral sites, one for iron in octahedral positions and one for oxygen ions. 626 reflections were used in this refinement.

The parameters of the crystal structure are listed in Tables 1. and 2.

Table 1. The atomic parameters from the Rietveld refinement of $\text{Sm}_3\text{Fe}_5\text{O}_{12}$ by using space group Ia3d.

a [Å]	12.53255(9)
O_x	-0.0303(6)
O_y	0.0529(9)
O_z	0.1494(7)
$B_{Fe,octa}$ [Å ²]	0.24(7)
$B_{Fe,tetra}$ [Å ²]	0.45(6)
B_{Sm} [Å ²]	0.34(3)
B_O [Å ²]	1.0(2)
R_B [%]	6.94
$R_{Exp.}$ [%]	10.03
R_P [%]	17.4
R_{WP} [%]	22.5

Table 2. The atomic parameters from the Rietveld refinement of $\text{Sm}_3\text{Fe}_5\text{O}_{12}$ by using space group R-3c.

a [Å]	17.7250(3)			
c [Å]	10.8519(4)			
atom	x	y	z	B [Å ²]
Fe, octa	0	0	0	0.23(6)
Fe, octa	0.5	0	0	0.23(6)
Fe, tetra	0.209(2)	0.166(2)	0.419(3)	0.38(8)
Sm	0.625	0	0.25	0.35(3)
Sm	0.125	0	0.25	0.35(3)
O1	0.337(4)	0.566(3)	0.776(6)	0.2(2)
O2	0.747(3)	0.817(4)	0.415(7)	0.2(2)
O3	0.748(4)	0.715(5)	0.617(6)	0.2(2)
O4	0.149(5)	0.884(6)	0.184(6)	0.2(2)
R _B [%]	7.02			
R _{Exp.} [%]	10.56			
R _P [%]	17.8			
R _{WP} [%]	22.6			

4. Discussion

The atomic coordinates obtained in the space group Ia3d can be transformed into the atomic coordinates in the group R-3c. The transformed coordinates are the same, within the sum of standard deviations, as the refined coordinates in the group R-3c.

The samarium ion is coordinated with four oxygen ions at 2.41 Å and four oxygen ions at 2.52 Å. If one takes an oxygen radius of 1.40 Å, the radius of the samarium ion is 1.01 Å. The tetrahedral iron is surrounded with four oxygens at the distance of 1.85 Å. This distance corresponds to the oxygen radius of 1.40 Å and high spin radius of Fe³⁺ of 0.47 Å in tetrahedral position. There are 6 oxygens around the octahedral site at 2.02 Å. This distance corresponds to the high spin ferri radii of 0.62 Å. The literature values of ionic radii in the garnet structure for Sm³⁺ and Fe³⁺ in tetrahedral and octahedral sites are 1.04 Å, 0.49 Å and 0.64 Å, respectively [9]. Note that the here obtained values of radii are somewhat smaller than those from literature which indicates a small presence of the covalent bond.

In the space group Ia3d, the *B* factors for the oxygen anions are always larger than the *B* factors for the cations, as expected. The *B* factor for the heaviest Sm ion is not the smallest, unexpectedly. This means that in this compound the strength of the bonds affects the *B* factors. By using expression for the mass averaged *B* factor [10]:

$$\bar{B} = \frac{6h^2}{m_a k_B \theta_D} \left[\frac{\Phi(x)}{x} + \frac{1}{4} \right] \quad (1)$$

where *h* represents Planck's constant, *m_a* average atomic weight, *k_B* Boltzmann's constant, *θ_D* the characteristic Debye's temperature, *x* the ratio of *θ_D* to absolute temperature and $\Phi(x)$ is Debye's integral, the characteristic Debye's temperature is found to be 320(40) K.

This result is in big disagreement with independent determination of θ_D , from thermal expansion of lattice parameters, which gives the value of 540 ± 30 K [11].

In the space group R-3c the B factor of oxygen ions is the smallest one. However, this can be true if the oxygen ions are strongly bonded to metallic ions. For this case θ_D is also calculated from equation (1). It was found that θ_D is 560(60) K. This result is in full agreement with the already mentioned result: 540 ± 30 K [11].

All R factors are slightly better for the refinement in the cubic space group. Also note that refinement in the Ia3d space group was done with less parameters than in the group R-3c.

An attempt was also made to refine crystal structure of magnetically ordered $\text{Sm}_3\text{Fe}_5\text{O}_{12}$ in the space group R-3. Note that the crystal and magnetic structure of $\text{Y}_3\text{Fe}_5\text{O}_{12}$ has been already refined in this space group [5], which is a subgroup of the group R-3c. However, these attempts were not successful, after many cycles the refinements did not reach a convergence.

5. Conclusion

There is no doubt that refinement in the cubic space group, characterized by smaller R factors and a less number of parameters, is better than the refinement in the rhombohedral space group. However, the refinement in the rhombohedral space group cannot be rejected from two reasons. The first is that theoretically the magnetically ordered sample can not be cubic [2]. In this case the magnetic moments oriented along the body diagonal in the cubic system require a rhombohedral space group. The other reason is agreement of the Debye's characteristic temperature from independent measurements only with the refinements in the rhombohedral space group. This temperature is between 500 and 600 K for all REIG and YIG [11]. The neutron diffraction measurements of mixed yttrium aluminum iron garnet showed that this sample, which is rhombohedral at low temperatures approaches cubic symmetry with an increase of temperature [6]. In the case of SmIG it seems that the cubic model better fits the experimental x-ray diffraction data but the rhombohedral model better describes Debye's temperature, i.e. a coarse description of lattice dynamics is better in the rhombohedral model.

References

1. M. Guillot, *Electronic and Magnetic Properties of Metals and Ceramics*, vol. 3B, part II, p. 1, (ed. K.H.J.Buschow, VCH Weinheim, 1994).
2. B. A. Tavger, *Kristallografiya* **3**, 339 (1958).
3. *Inorganic Crystal Structure Data Base*, Gmelin, (FIZ, Karlsruhe, 1997).
4. R. Hock, H. Fuess, T. Vogt, M. Bonnet, *J. Solid State Chem.* **84**, 39 (1990).
5. D. Rodić, M. Mitrić, R. Tellgren, H. Rundlof, A. Kremenović, *J. Magn. Magn. Mat.* **191**, 137 (1999).
6. D. Rodić, M. Mitrić, R. Tellgren, H. Rundlof, *J. Magn. Magn. Mat.* (2001).
7. J. Rodriguez-Carvajal, *Collected Abstracts of Powder Diffraction Meeting*, p. 127 (Toulouse, 1990).

8. D. Rodić, R. Tellgren, M. Guillot, *J. Magn. Magn. Mat.* **94**, 260 (1991).
9. M. A. Gilleo, *E.P. Wohlfarth (Ed.) Ferromagnetic Materials*, vol. 2., p. 1, (North Holland, Amsterdam, 1980).
10. *International Tables for X-ray Crystallography*, vol. II, p. 241, (The Kynoch Press, Birmingham, 1959).
11. F. Sayetat, *J. Magn. Magn. Mat.* **58**, 334 (1986).

Compensation Temperatures in Systems with Three and Four Sublattices and Superlattices

Milica Pavkov, Milan Pantić, Marijana Kirćan and Tatjana Tošić
*Institute of Physics, Faculty of Sciences, Trg Dositeja Obradovića 4,
21000 Novi Sad, Yugoslavia
E-mail: milica@im.ns.ac.yu*

Received: September 20, 2001

Abstract

Mean-Field theory is developed for the system of magnetic ions located on three or four sublattices, described by the Heisenberg Hamiltonian with all the exchange integrals different. It is shown that for a certain ratio of exchange parameters, the system with all antiferromagnetic interactions can manifest two compensation temperatures. On the other hand, the same theory applied to the superlattices with three or four planes in the unit indicates that there can occur two compensation points with all possible choices of interaction signs.
PACS: 75.10.Jm, 75.50.Ee, 75.50.Gg

Key words: Heisenberg ferro- and antiferromagnet, compensation temperature, Mean-Field approximation, several sublattice system, magnetic superlattices

1. Introduction

Recent advances in the theoretical prediction and synthesis of materials with complicated structures have enabled the production of a material with two compensation temperatures [1]. Ohkoshi *et al.* have first developed a Mean-Field (MF) theory for the random material $(\text{Ni}_a^{\text{II}}\text{Mn}_b^{\text{II}}\text{Fe}_c^{\text{II}})_{1.5} [\text{Cr}^{\text{III}}(\text{CN})_6] \cdot z\text{H}_2\text{O}$ and predicted the existence of two compensation points for the system: $a = 0.20$, $b = 0.61$, $c = 0.19$. They continued with the synthesis and succeeded experimentally to obtain this behaviour for the material with $a = 0.22$, $b = 0.60$, $c = 0.18$.

The structure proposed was the system of four sublattices where the Cr ion is surrounded in a random manner by Ni and Fe with ferromagnetic coupling and Mn with antiferromagnetic coupling.

In order to extend their studies theoretically, we looked in the literature for similar complex systems. We noticed the work of Herbst [2] and del Moral [3] who studied the systems with several sublattices. Herbst [2] reviews the properties of the compounds of the general formula $\text{R}_2\text{Fe}_{14}\text{B}$ where R is the rare-earth atom. It is noticed that light rare-earth members of the series are coupled ferromagnetically with iron, while heavy rare-earth atoms are coupled antiferromagnetically (or ferrimagnetically). At the moment

when this report was prepared, no compensation points were recorded in any of the pure materials, although such behaviour was known in some other rare-earth compounds, so it seems plausible to start looking for compensation temperatures in the systems with several sublattices. Our aim here is to study such systems. The next step is the choice of the theoretical formalism. It seems that, however simple it may be, the MF approximation leads to results which agree with experimental data, where available. The very success of the work [1], is one of the arguments, yet the results of some other papers dealing with Heisenberg superlattices [4,5], also encourage us in this choice. For this reason, we shall study such systems within the framework of the MFA theory, as the first step of the study.

In this paper we shall first formulate the MF theory for the system with three and four sublattices, where one can obtain interesting behaviour of the total and sublattice magnetization at finite temperatures. The model is presented in Section 2 where MF theory is formulated. The results of the numerical studies are discussed. In Section 3, MF theory is developed for the superlattices. Some final remarks are given in the Conclusion.

2. The Model and Mean Field Equations

The model of a bulk crystal with several sublattices is formulated in the following way: the underlying lattice of sites is a simple cubic one and interpenetrating sublattices are distributed among these sites.

In the case of three sublattices, an ion of the given sublattice (say a) is surrounded by an equal number (three) of sites belonging to other two sublattices (b and c), and none of its own. Furthermore, along each direction (x coinciding with crystallographic a - axis, y with b and z with c), the neighbours always belong to different lattices. The possible configuration which provides translational invariance is presented in Figure 1a.

This configuration can most easily be described by looking at the alternating ion distribution along any direction. The same principle can be applied for the construction of the four sublattice system. One can see that the repeating configuration of all four types of ions along any direction, as given in Figure 1b, can assure the translational invariance.

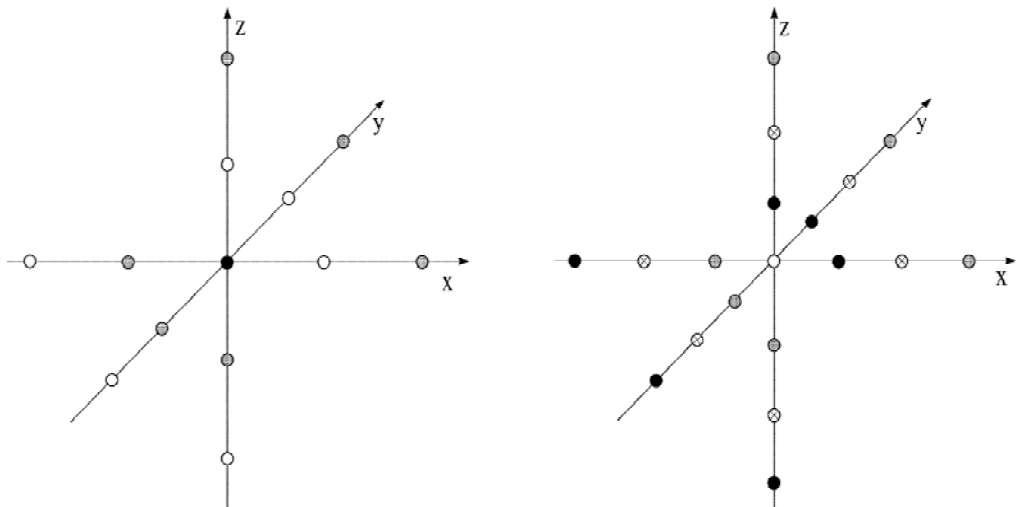


Figure 1. The system of three sublattices (a) and four sublattices (b) treated in this paper.

Such a complicated structure obviously demands certain simplification. The basic simplification here is that we shall assume the interaction between the nearest neighbours only. We shall also assume that we are dealing with the system of localized spins, so it can be described by the Heisenberg Hamiltonian:

$$H = -\frac{1}{2} \sum_{\vec{n}_\alpha, \vec{m}_\beta} J_{\vec{n}_\alpha, \vec{m}_\beta} \vec{S}_{\vec{n}_\alpha} \cdot \vec{S}_{\vec{m}_\beta} \quad \alpha, \beta = a, b, c, d \quad (1)$$

Here \vec{n}_α is the symbolic description concerning the position of the ion within the sublattice. We shall now write down the explicit form assuming that all spins are different: $S_a \neq S_b \neq S_c \neq S_d$ and all exchange integrals are different: $J_{ab} \neq J_{bc} \neq J_{cd} \neq J_{da}$ and each one can be either ferromagnetic (> 0) or antiferromagnetic (< 0).

$$H = -\frac{1}{2} \sum_{\vec{n}_a, \vec{n}_a + \vec{\lambda}_a^b} J_{ab} \vec{S}_{\vec{n}_a} \cdot \vec{S}_{\vec{n}_a + \vec{\lambda}_a^b} - \frac{1}{2} \sum_{\vec{n}_a, \vec{n}_a + \vec{\lambda}_a^d} J_{ad} \vec{S}_{\vec{n}_a} \cdot \vec{S}_{\vec{n}_a + \vec{\lambda}_a^d} - \frac{1}{2} \sum_{\vec{n}_b, \vec{n}_b + \vec{\lambda}_b^a} J_{ab} \vec{S}_{\vec{n}_b} \cdot \vec{S}_{\vec{n}_b + \vec{\lambda}_b^a} - \frac{1}{2} \sum_{\vec{n}_d, \vec{n}_d + \vec{\lambda}_d^a} J_{ad} \vec{S}_{\vec{n}_d} \cdot \vec{S}_{\vec{n}_d + \vec{\lambda}_d^a} + (bc + cb) + (cd + dc) \quad (2)$$

Here \vec{n}_a denotes the particular site in the a - sublattice and $\vec{n}_a + \vec{\lambda}_a^b$ denotes three sites which are occupied by the neighbouring sites of b lattice and so on. The meaning of the last two terms is obvious.

2.1. Mean-Field Approximation

In order to apply the standard Mean-Field Approximation [6], we shall assume that an external field \mathcal{H} in z - direction, is added:

$$H_{ZEM} = -g\mu_B \mathcal{H} \sum_{\vec{n}_\alpha} S_{\vec{n}_\alpha}^z \quad (3)$$

This introduces an Ising symmetry into the problem, so the decoupling can be performed in the following manner:

$$\vec{S}_{\vec{n}_\alpha} \cdot \vec{S}_{\vec{n}_\beta} \approx \langle S_{\vec{n}_\alpha}^z \rangle S_{\vec{n}_\beta}^z + S_{\vec{n}_\alpha}^z \langle S_{\vec{n}_\beta}^z \rangle - \langle S_{\vec{n}_\alpha}^z \rangle \langle S_{\vec{n}_\beta}^z \rangle \quad (4)$$

Assuming the translational invariance $\langle S_{\vec{n}_\alpha}^z \rangle = \langle S_\alpha^z \rangle = \sigma_\alpha$ ($\alpha = a, b, c, d$), we can write down the MFA Hamiltonian :

$$H_{MFA} = H_0 - 1/2 \langle H_0 \rangle_{\mathcal{H}=0} \quad (5)$$

$$H_0 = \sum_{\alpha=a,b,c,d} \sum_{\vec{n}_\alpha} \tilde{\mathcal{H}}_\alpha S_{\vec{n}_\alpha}^z \quad (6)$$

The effective fields are given as:

$$\tilde{\mathcal{H}}_a = \frac{z}{2} (J_{ab}\sigma_b + J_{ad}\sigma_d) + g\mu_B \mathcal{H} \quad (7)$$

$$\tilde{\mathcal{H}}_b = \frac{z}{2} (J_{ab}\sigma_a + J_{bc}\sigma_c) + g\mu_B \mathcal{H} \quad (8)$$

$$\tilde{\mathcal{H}}_c = \frac{z}{2} (J_{bc}\sigma_c + J_{cd}\sigma_d) + g\mu_B\mathcal{H} \quad (9)$$

$$\tilde{\mathcal{H}}_d = \frac{z}{2} (J_{ad}\sigma_a + J_{cd}\sigma_c) + g\mu_B\mathcal{H} \quad (10)$$

Here $z = 6$ equals to the number of the nearest neighbours. If we introduce the number of sites per sublattice $N = N_{tot}/4$, we can write:

$$H_0 = -N \sum_{\alpha=a,b,c,d} \tilde{\mathcal{H}}_\alpha S_\alpha^z \quad (11)$$

Using the standard procedure, we obtain the free energy as

$$\mathcal{F} = \frac{F}{N} = -\theta \sum_{\alpha=1}^4 \ln Z_\alpha \quad (12)$$

$$Z_\alpha = \sum_{\nu=-S_\alpha}^{S_\alpha} \exp[-\beta\tilde{\mathcal{H}}_\alpha\nu] = \frac{sh(S_\alpha + 1/2) x_\alpha}{shx_\alpha/2} \quad (13)$$

where $x_\alpha = \beta\tilde{\mathcal{H}}_\alpha$ and

$$\sigma_\alpha = S_\alpha B_{S_\alpha}(S_\alpha x_\alpha) \quad \alpha = a, b, c, d \quad (14)$$

and B_{S_α} is the standard Brillouin function [4]. In order to unify the notation, we shall use the following convention $J_{ab} = J_1$, $J_{bc} = J_2$, $J_{cd} = J_3$, $J_{da} = J_4$ and for spin $S_a = S_1$, $S_b = S_2$, $S_c = S_3$, $S_d = S_4$.

The system of four equations (14) must be solved in a self-consistent manner. It will be discussed numerically in the following section for some particular choices of interaction, although an estimate of the transition temperature θ_c can be obtained by a simple linearization. We shall solve the equation for sublattice magnetization and plot the total magnetization (simply "magnetization" further on) obtained as the algebraic sum of all sublattice magnetizations.

Working in an identical manner, we can obtain the system of Mean-Field equations for the system with three sublattices, which explicit form need not be quoted here.

2.2. Numerical Results

Let us now analyze numerically some relevant examples. We treated first the following configuration ($\uparrow \uparrow \downarrow \uparrow$) described by the exchange parameters: $J_1 = 1.5 \text{ cm}^{-1}$, $J_2 = -3 \text{ cm}^{-1}$, $J_3 = -2 \text{ cm}^{-1}$, $J_4 = 1 \text{ cm}^{-1}$ and following spin values $S_1 = 1$, $S_2 = 1/2$, $S_3 = 5/2$, $S_4 = 3/2$. The behaviour of the magnetization is given at Figure 2 .

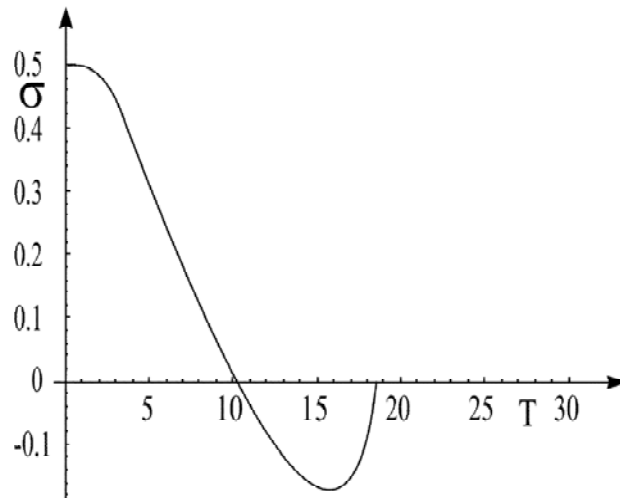


Figure 2. The magnetization of the system with four sublattices with the following parameters: $J_1 = 1.5 \text{ cm}^{-1}$, $J_2 = -3 \text{ cm}^{-1}$, $J_3 = -2 \text{ cm}^{-1}$, $J_4 = 1 \text{ cm}^{-1}$, $S_1 = 1$, $S_2 = 1/2$, $S_3 = 5/2$, $S_4 = 3/2$.

We see that there occurs a single compensation point. Some other choice of parameters may lead to none or a single compensation temperature, but never to two, for this configuration. Of course, one should be careful with this conclusion, since it follows purely from our numerical experience, while we were not able to prove it in an analytical manner.

However, a "zig-zag" structure described by completely antiferromagnetic couplings $J_1 = -1 \text{ cm}^{-1}$, $J_2 = -10 \text{ cm}^{-1}$, $J_3 = -7 \text{ cm}^{-1}$, $J_4 = -2 \text{ cm}^{-1}$, $S_1 = S_2 = S_4 = 1$, $S_3 = 3/2$ happens to have two compensation temperatures, although the reverse magnetization is rather low, as seen in Figure 3.

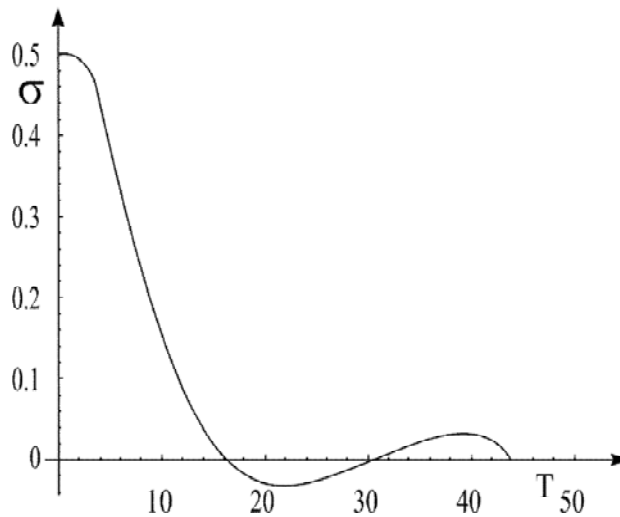


Figure 3. The magnetization of the system with four sublattices with the following parameters: $J_1 = -1 \text{ cm}^{-1}$, $J_2 = -10 \text{ cm}^{-1}$, $J_3 = -7 \text{ cm}^{-1}$, $J_4 = -2 \text{ cm}^{-1}$, $S_1 = S_2 = S_4 = 1$, $S_3 = 3/2$

Finally, we have not managed to obtain any set of parameters leading to two compensation points in the three sublattice structure.

Now we can comment on these results. The values of exchange integrals are chosen in the range as proposed in [1]. However, they have shown that the results are very sensitive even to small changes of the stoichiometry. The fact that we managed to find a set of parameters which predicts the occurrence of two compensation temperatures even at ordered structures can be formulated as our basic result: disorder (non-stoichiometry) is not a prerequisite for the phenomenon.

In our case that would mean that the system is sensitive to small changes of the ratios of parameters. Yet, once the ratios of the parameters allowing two compensation temperatures are established, one can vary their numerical values and obtain two compensation points again. The compensation temperatures obtained in this way lie in a broad range of values, which offers some good perspective for the possible "construction" of such materials. We present here an example (Figure 4.) where the parameters from Figure 3. are all multiplied by a factor of five. The compensation points and critical temperature all rise by the same factor of five, since the magnetizations (14) are functions of the ratios r_α (for instance $r_\alpha = \frac{J_\alpha}{J_1}$) and reduced temperature $\beta = J_1\beta$ only .

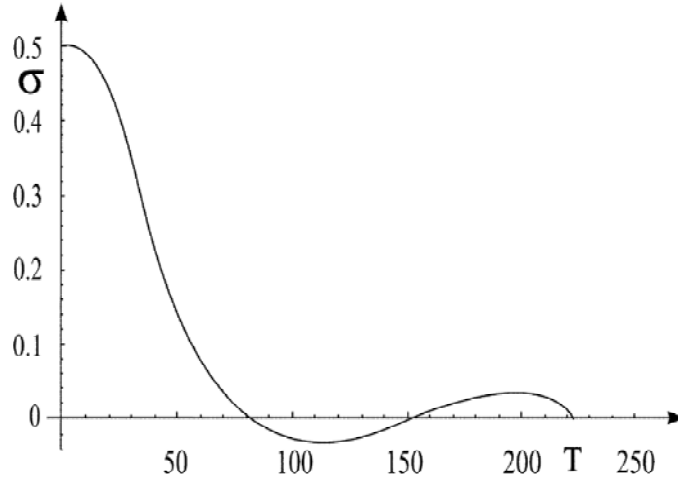


Figure 4. The magnetization of the system with four sublattices with the following parameters: $J_1 = -5 \text{ cm}^{-1}$, $J_2 = -50 \text{ cm}^{-1}$, $J_3 = -35 \text{ cm}^{-1}$, $J_4 = -10 \text{ cm}^{-1}$, $S_1 = S_2 = S_4 = 1$, $S_3 = 3/2$.

We are now going to show that in the case of superlattices, the conditions for the occurrence of two compensation points are much more favorable.

3. Mean-Field Approximation for the Superlattices

The basic underlying lattice can also support the superlattices. The superlattices are assumed to consist of ferromagnetically ordered layers (yz - planes) and the group of 3 or 4 layers is the unit repeated along the x - axis. Interlayer coupling can be either ferromagnetic or antiferromagnetic, which will be explained in each particular case.

The system of MF equations can be written in the completely general form irrespective of coupling. The Hamiltonian of the system can be written as

$$H = -\frac{1}{2} \sum_{\vec{n}_\alpha, \vec{n}_\alpha + \vec{\delta}_l} I_\alpha \vec{S}_{\vec{n}_\alpha} \cdot \vec{S}_{\vec{n}_\alpha + \vec{\delta}_l} - \frac{1}{2} \sum_{\vec{n}_\alpha, \vec{n}_\alpha + \vec{\delta}_\beta^x} J_{\alpha\beta} \vec{S}_{\vec{n}_\alpha} \cdot \vec{S}_{\vec{n}_\alpha + \vec{\delta}_\beta^x} \quad \alpha, \beta = a, b, c(d) \quad (15)$$

The first term describes the interaction of spins within each layer, so that α enumerates the layer, \vec{n} is the 2D vector within the layer and $\vec{\delta}_l$ connects each spin with all its neighbours within the layer. The spins within the layer interact ferromagnetically, so that all $I_\alpha > 0$.

The second term describes the coupling between the layers α and β , so that $\vec{n}_\alpha + \vec{\delta}_\beta^x$ connects the spin at the site \vec{n}_α with the spin in the neighbouring plane β , positioned directly "above" it along the x -axis. The sum over $\vec{n}_\alpha + \vec{\delta}_\beta^x$ always includes both neighbours and the factor $1/2$ takes care of the proper number of interactions.

We assume that the spins within the layer are equal, but need not be equal among the layers ($S_a \neq S_b \neq S_c \neq S_d$). In order to preserve the translational invariance along all directions, we assume periodic boundary conditions in all directions.

The notation is the following: $J_{ab} = J_1$, $J_{bc} = J_2$ and for three superlattices $J_{ca} = J_3$, while for four superlattices $J_{cd} = J_3$, $J_{da} = J_4$. As for in-plane interactions, $I_a = I_1$ etc.

We allow J to be either positive or negative, since it is possible nowadays to produce such superlattices depending on the layer width and non-magnetic ions inserted in the space between the layers.

Taking into account the translational invariance of the spins within the layer and the cells along the x -axis, we can use: $\langle S_{\vec{n}_\alpha}^z \rangle = \langle S_\alpha^z \rangle = \sigma_\alpha$ ($\alpha = 1, 2, 3, 4$). The basic set of equations is again of the type (14), and the effective fields are given by:

a) four layer unit:

$$\tilde{\mathcal{H}}_1 = z_2 I_1 \sigma_1 + \frac{z_1}{2} (J_1 \sigma_2 + J_4 \sigma_4) + g \mu_B \mathcal{H} \quad (16)$$

$$\tilde{\mathcal{H}}_2 = z_2 I_2 \sigma_2 + \frac{z_1}{2} (J_1 \sigma_1 + J_2 \sigma_3) + g \mu_B \mathcal{H} \quad (17)$$

$$\tilde{\mathcal{H}}_3 = z_2 I_3 \sigma_3 + \frac{z_1}{2} (J_2 \sigma_2 + J_3 \sigma_4) + g \mu_B \mathcal{H} \quad (18)$$

$$\tilde{\mathcal{H}}_4 = z_2 I_4 \sigma_4 + \frac{z_1}{2} (J_3 \sigma_3 + J_4 \sigma_1) + g \mu_B \mathcal{H} \quad (19)$$

b) three layer unit:

$$\tilde{\mathcal{H}}_1 = z_2 I_1 \sigma_1 + \frac{z_1}{2} (J_1 \sigma_2 + J_3 \sigma_3) + g \mu_B \mathcal{H} \quad (20)$$

$$\tilde{\mathcal{H}}_2 = z_2 I_2 \sigma_2 + \frac{z_1}{2} (J_1 \sigma_1 + J_2 \sigma_3) + g \mu_B \mathcal{H} \quad (21)$$

$$\tilde{\mathcal{H}}_3 = z_2 I_3 \sigma_3 + \frac{z_1}{2} (J_2 \sigma_2 + J_3 \sigma_1) + g \mu_B \mathcal{H} \quad (22)$$

Here $z_1 = 2$ denotes the number of out-of-layer neighbours while $z_2 = 4$ is the number of the neighbours within the layer.

The superlattices are of more practical interest since it seems possible to influence the interaction between the planes in a more efficient way by adding non-magnetic materials between the planes, similar to sandwich structures. It turns out that it is much easier to find a set of parameters for which two compensation temperatures occur. In fact, for each configuration of superlattices, it is possible to obtain such a phenomenon. (Figures 5.-6.)

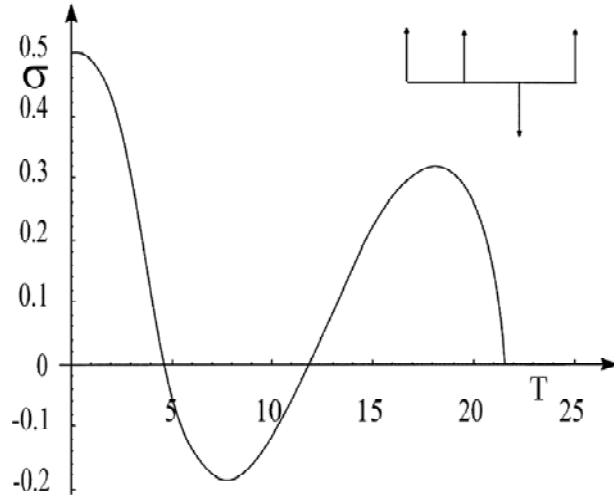


Figure 5. The magnetization of the superlattice with four-layer unit with the following parameters: $J_1 = 0.5 \text{ cm}^{-1}$, $J_2 = -3 \text{ cm}^{-1}$, $J_3 = -2 \text{ cm}^{-1}$, $J_4 = 0.4 \text{ cm}^{-1}$, $I_1 = 1 \text{ cm}^{-1}$, $I_2 = 3 \text{ cm}^{-1}$, $I_3 = 0.5 \text{ cm}^{-1}$, $I_4 = 3 \text{ cm}^{-1}$, $S_1 = 1$, $S_2 = 1/2$, $S_3 = 5/2$, $S_4 = 3/2$ (Unit configuration is shown in the insert).

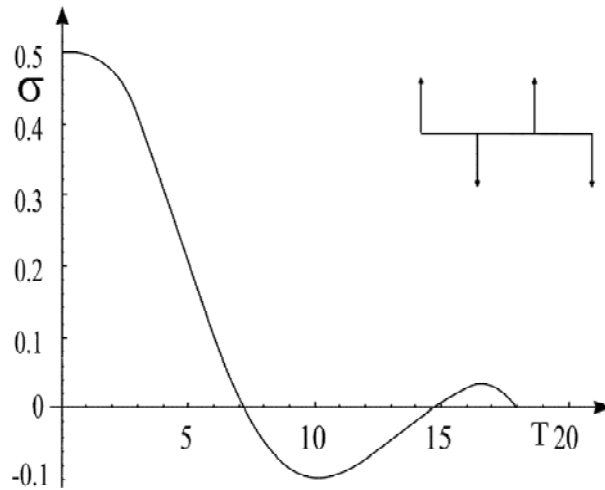


Figure 6. The magnetization of the superlattice with four-layer unit with the following parameters: $J_1 = -1 \text{ cm}^{-1}$, $J_2 = -10 \text{ cm}^{-1}$, $J_3 = -4 \text{ cm}^{-1}$, $J_4 = -2 \text{ cm}^{-1}$, $I_1 = 0.5 \text{ cm}^{-1}$, $I_2 = 1.5 \text{ cm}^{-1}$, $I_3 = 3 \text{ cm}^{-1}$, $I_4 = 2 \text{ cm}^{-1}$, $S_1 = 3/2$, $S_2 = S_3 = S_4 = 1$ (Unit configuration is shown in the insert).

Obviously, the manipulation is facilitated by the larger number of parameters which can be fitted. Also, even here one can increase the values of exchange parameters retaining their ratios and it will lead to the similar behaviour again. Examples are given in Figure 7. (parameters of Figure 5. multiplied by a factor of 5) and Figure 8. (parameters of Figure 6. multiplied by a factor of 10).

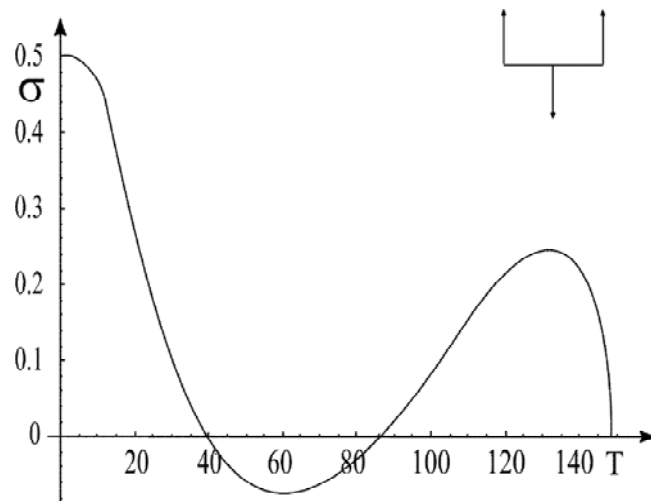


Figure 7. The magnetization of the superlattice with three-layer unit with the following parameters: $J_1 = -5 \text{ cm}^{-1}$, $J_2 = -10 \text{ cm}^{-1}$, $J_3 = -2.5 \text{ cm}^{-1}$, $I_1 = 2.5 \text{ cm}^{-1}$, $I_2 = 6 \text{ cm}^{-1}$, $I_3 = 12.5 \text{ cm}^{-1}$, $S_1 = 1$, $S_2 = 5/2$, $S_3 = 2$ (Unit configuration is shown in the insert).

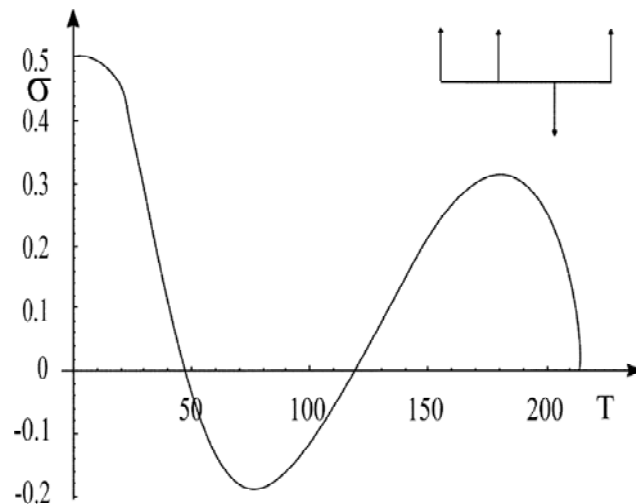


Figure 8. The magnetization of the superlattice with four-layer unit with the following parameters: $J_1 = 5 \text{ cm}^{-1}$, $J_2 = -30 \text{ cm}^{-1}$, $J_3 = -20 \text{ cm}^{-1}$, $J_4 = 4 \text{ cm}^{-1}$, $I_1 = 10 \text{ cm}^{-1}$, $I_2 = 30 \text{ cm}^{-1}$, $I_3 = 5 \text{ cm}^{-1}$, $I_4 = 30 \text{ cm}^{-1}$, $S_1 = 1$, $S_2 = 1/2$, $S_3 = 5/2$, $S_4 = 3/2$ (Unit configuration is shown in the insert).

It is instructive to follow the behaviour of particular layer magnetizations and see how the compensation arises in one particular case for three and four-layer superlattices (Figure 9.a i 9.b) (Similar calculation for sublattices also shows why it is so difficult to reach the compensation in that case.)

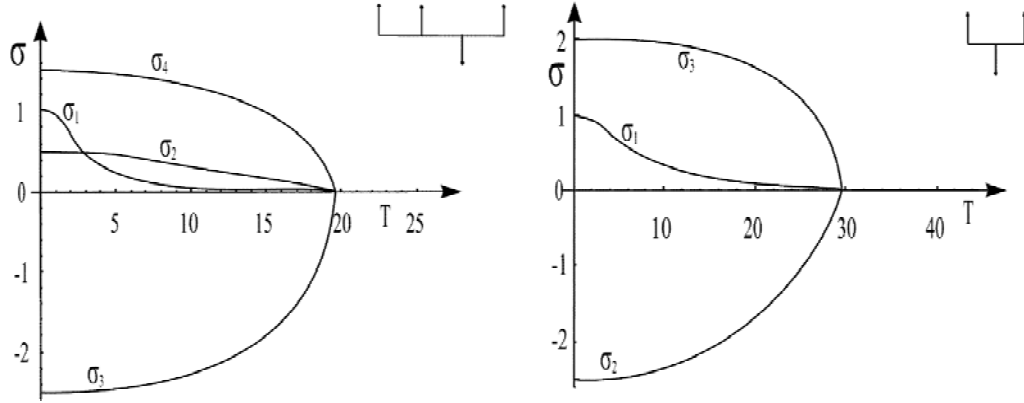


Figure 9. The magnetization of the layers in the superlattice with (a) four-layer unit with the following parameters: $J_1 = 0.5 \text{ cm}^{-1}$, $J_2 = -3 \text{ cm}^{-1}$, $J_3 = -2 \text{ cm}^{-1}$, $J_4 = 0.4 \text{ cm}^{-1}$, $I_1 = 1 \text{ cm}^{-1}$, $I_2 = 3 \text{ cm}^{-1}$, $I_3 = 0.5 \text{ cm}^{-1}$, $I_4 = 0.4 \text{ cm}^{-1}$, $S_1 = 1$, $S_2 = 1/2$, $S_3 = 5/2$, $S_4 = 3/2$, and (b) three-layer unit with the following parameters: $J_1 = -1 \text{ cm}^{-1}$, $J_2 = -2 \text{ cm}^{-1}$, $J_3 = 0.5 \text{ cm}^{-1}$, $I_1 = 0.5 \text{ cm}^{-1}$, $I_2 = 1.2 \text{ cm}^{-1}$, $I_3 = 2.5 \text{ cm}^{-1}$, $S_1 = 1$, $S_2 = 5/2$, $S_3 = 2$ (Unit configuration is shown in the insert).

4. Concluding Remarks

We have shown within the Mean-Field approximation that even the ordered systems with several sublattices can be made to possess two compensation temperatures by a suitable choice of components (i.e. system parameters), while there are much more possible combinations in the case of superlattices. When it comes to the practical realization of these systems, we do not have experimental facilities to produce them, but the success of the Japanese team [1] indicates that one could obtain such materials based on our models, especially since we have shown that such a possibility appears in a wide range of temperatures.

One should finally address the justification of the application of MF theory. There is no problem with the system with several sublattices (study [1] clearly shows that), since these are typical three-dimensional samples where MFA leads to plausible results (except in the vicinity of T_c , which is not of interest in this study). The problem may arise in the study of superlattices, since we have assumed that we deal with ferromagnetically ordered (two-dimensional) layers which are then coupled either ferromagnetically or antiferromagnetically. It is well-known that there is no purely two-dimensional ferromagnetism [7], but it is precisely the interlayer coupling in these models (however small it may be) that makes long range order in each layer possible.

One should, however stress, that in the limit of strong interlayer antiferromagnetic coupling ($|J_\alpha| \gg I_\alpha$), the long range ferromagnetic ordering may be also destroyed due to the possibility of creation of singlets in the neighbouring sites of two layers. (These results will be published elsewhere.) We do not consider such extreme cases here, so from the theoretical point of view, we think that this is an indication that the materials proposed by our models here might be constructed, although some more, both, theoretical and experimental effort is necessary.

Acknowledgments

This work was supported by the Serbian Ministry of Science and Technology under project: "Dynamical and Thermodynamical Properties of Strongly Correlated Systems with Complex Structures" (No.1895).

References

1. S. Ohkoshi, Y. Abe, A. Fujishima and K. Hashimoto, *Physical Review Letters* **82**, 1285 (1999).
2. F. Herbst, *Review of Modern Physics* **63**, 819 (1991).
3. A. del Moral, *Journal of Physics: Condensed Matter* **4**, 4687 (1992).
4. R. E. Camley and D. R. Tiley, *Phys. Rev.* **B 37**, 3413 (1988).
5. R. E. Camley, *Phys. Rev.* **B 39**, 12 316 (1989).
6. H. E. Stanley, *Introduction to Phase Transitions and Critical Phenomena*, (Clarendon Press, Oxford, 1971).
7. N. Mermin, H. Wagner, *Physical Review Letters* **17**, 1133 (1966).

Magnetic Properties of Cr(III) and Fe(III) Ions in Hexaaqua-Nitrate-Trihydrates

M. Vučinić¹, M. Mitrić², V. Kusigerski², A. Kapor¹, A. Szytula³

¹ *Institute of Physics, University of Novi Sad,*

Trg Dositeja Obradovića 4, 21000 Novi Sad, Yugoslavia

² *Laboratory for Theoretical Physics and Condensed Matter Physics,*

INN "Vinča", PP522, 11001 Beograd, Yugoslavia

³ *Jagellonian University, Institute of Physics, 30-059 Krakow 16, Poland*

Received: September 24, 2001

Abstract

The manuscript contains new measurements and calculations of magnetic susceptibility of Cr(III) and Fe(III) ions in hexaaqua-nitrate-trihydrate. The magnetic properties of the ion M=Cr(III), Fe(III) in hexaaqua-nitrate-trihydrate $M(\text{H}_2\text{O})_6(\text{NO}_3)_3 \cdot 3\text{H}_2\text{O}$ were studied from the temperature dependence of magnetic susceptibility determined using the SQUID susceptometer, within the temperature range $4 \text{ K} \leq T \leq 290 \text{ K}$. The detected deviation from the Curie-Weiss law is explained by the splitting of the ground state energies of the magnetic ions under the influence of the crystalline field (splitting in the zero field) and the contribution of the temperature independent Van-Vleck paramagnetism.

Key words: Magnetic susceptibility, Cr(III) and Fe(III) ions, crystalline field

1. Introduction

It is known that magnetic ions in crystals are exposed to the influence of the crystal surrounding (named "ligand" or "crystalline" field). The crystalline field can change the magnetic properties of ions in relation to free ion properties. The systems, which contain isolated magnetic ions, are close to an ideal paramagnetic substances and they are very convenient for research of the crystalline field effect. The absence of magnetic interaction between ions, gives an opportunity to observe only the crystalline field effect. The hexaaqua-nitrate-trihydrate $M(\text{H}_2\text{O})_6(\text{NO}_3)_3 \cdot 3\text{H}_2\text{O}$, M=Cr(III), Fe(III), which is the object of this research is a very good example of such systems.

The single crystals of Cr(III) and Fe(III) hexaaqua-nitrate-trihydrates were obtained by slow crystallization from a saturated aqueous solution of pure compounds $\text{Cr}(\text{NO}_3)_3 \cdot 9\text{H}_2\text{O}$ and $\text{Fe}(\text{NO}_3)_3 \cdot 9\text{H}_2\text{O}$. The crystal structures of Cr(III) and Fe(III) hexaaqua-nitrate-trihydrates were solved using a single crystal X-ray diffraction method. It was confirmed that the samples are isostructural. These materials crystallize in monoclinic system, space

group $P2_1/c$ (No 14) [1,2]. Cations Cr(III) and Fe(III) occupy two distinct unequivalent special positions [(a) 0,0,0; 0,0.5,0.5; (d) 0.5,0.5,0.5; 0.5,0.5,0] local symmetry $\bar{1}$. Coordinated polyhedra of cations are distorted octahedra. The distortion can be considered as an axial symmetric and equal for both special positions. The electron structure of $\text{Cr}(\text{NO}_3)_3 \cdot 9\text{H}_2\text{O}$ was analyzed using diffusion-reflection and UV spectra of powder sample [3].

It is known that the free ion Cr(III) ground state is 4F ($S = 3/2$, $L = 3$). The regular octahedra crystalline field splits this state into three orbital multiplets. The ground level is orbital singlet $^4A_2(g)$ with spin $S = 3/2$ (Figure 1(a)). Because of axial distortion of the octahedral surrounding, this ground state splits (zero field effect) into two doublets $S = \pm 3/2$, $S = \pm 1/2$ [4]. The energy level distance between these doublets is D (Figure 1(a)). The energy level distances between ground multiplet and excited multiplets $^4T_2(g)$ and $^4T_1(g)$ are approximately 17000 cm^{-1} and 24000 cm^{-1} , respectively [3].

The free ion Fe(III) ground state is an orbital singlet 6S ($S = 5/2$, $L = 0$). The regular octahedral crystalline field does not split the ground state of free Fe(III) ion. The distorted octahedral surrounding (zero field effect) splits this ground state into three doublets with energy level distances D_1 and D_2 , as shown in Figure 1(b). The energy level distances formed by zero field effect could be determined using magnetic measurements.

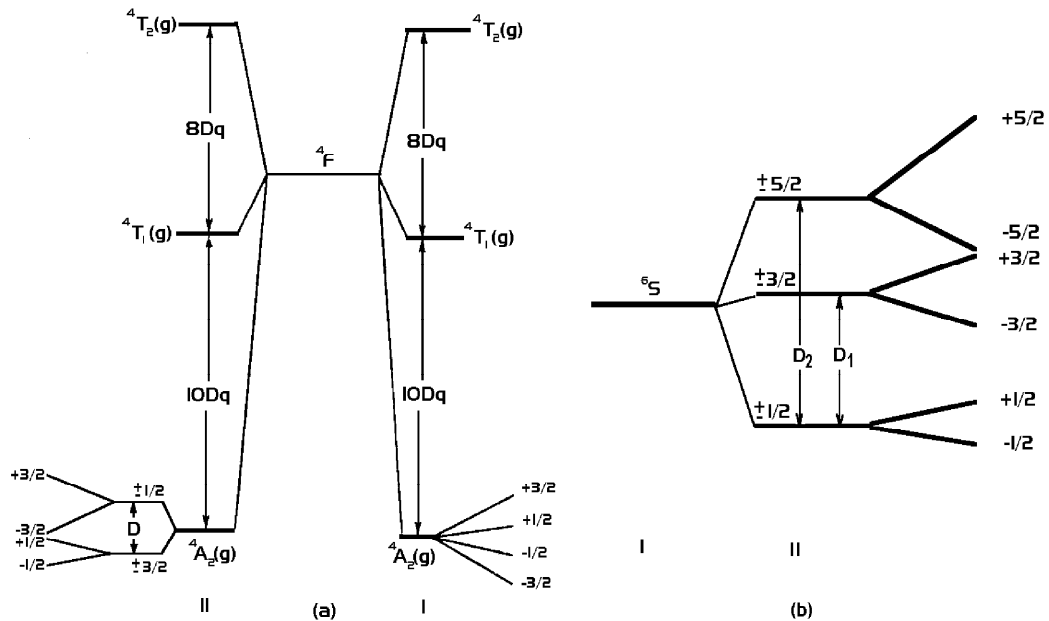


Figure 1. Orbital singlet splitting in regular (I) and distorted (II) crystalline field for: (a) Cr(III) ion, (b) Fe(III) ion.

Generally, the magnetic susceptibility of isolated ions in the crystalline field could be described by Van-Vleck equation [4]:

$$\chi = \frac{N \sum_n [(E_n^{(1)})^2/kT - 2E_n^{(2)}] \exp\{-E_n^0/kT\}}{\sum_n \exp\{-E_n^0/kT\}} \quad (1)$$

In the previous equation, the energy level is developed into a series in terms of the applied

magnetic field - H : $E_n = E_n^0 + HE_n^{(1)} + H^2E_n^{(2)}$

2. Results and discussion

We wanted to connect the physical properties of Cr(II) and Fe(III) hexaaqua-nitrate-trihydrates with the known crystal structure. For this purpose, we additionally performed magnetic measurements. The temperature dependence of the magnetic susceptibility of the examined materials was determined using the SQUID susceptometer, within the temperature range $4 \text{ K} \leq T \leq 290 \text{ K}$ in magnetic field 1T. The experimental data of the inverse magnetic susceptibility, per gram-ion are shown in Figures 2 and 3. We concluded that both samples are in paramagnetic phase in a whole measurement temperature range. It can be clearly seen that the experimental data show deviation from the Curie-Weiss law, so we can describe the experimental data with Van-Vleck equation (1) applied to 3d ions in crystalline field, with energy spectra as it is shown in Figures 1(a) and 1(b).

In both cases of ions Cr(III) and Fe(III) we can ignore the excited level population due to the great energy splitting. The only levels, which are populated, are formed from the ground state splitting in the crystalline field. The influence of excited multiplets, are taken into consideration only as the temperature independent Van-Vleck contribution (second order Zeeman effect) χ_{TIP} , in case of Cr(III) ions. In the case of Fe(III) ions, there is no ground state splitting in the regular crystalline field, so we can ignore the temperature independent Van-Vleck paramagnetism. Taking into account the above explained, as well as the fact that the zero field effect exists in case of both ions, Van-Vleck equation obtain forms:

$$\chi = \frac{Ng^2\mu_B^2}{4kT} \left[\frac{1 + 9 \exp\{-D/kT\}}{1 + \exp\{-D/kT\}} \right] + \chi_{TIP} \quad (2)$$

$$\chi = \frac{Ng^2\mu_B^2}{4kT} \left[\frac{1 + 9 \exp\{-D_1/kT\} + 25 \exp\{-D_2/kT\}}{1 + \exp\{-D_1/kT\} + \exp\{-D_2/kT\}} \right] \quad (3)$$

for Cr(III) and Fe(III) ions, respectively.

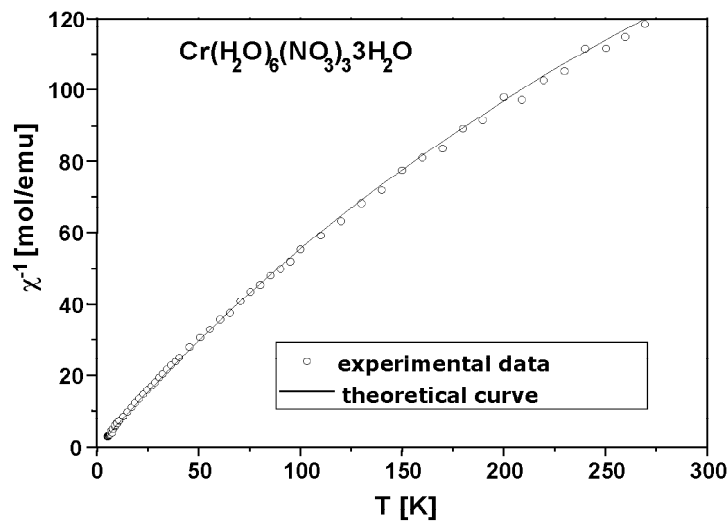


Figure 2. Inverse magnetic susceptibility for Cr(III) ions in hexaaqua-nitrate-trihydrate. Theoretical curve is obtained using equation 2 for fitting experimental data.

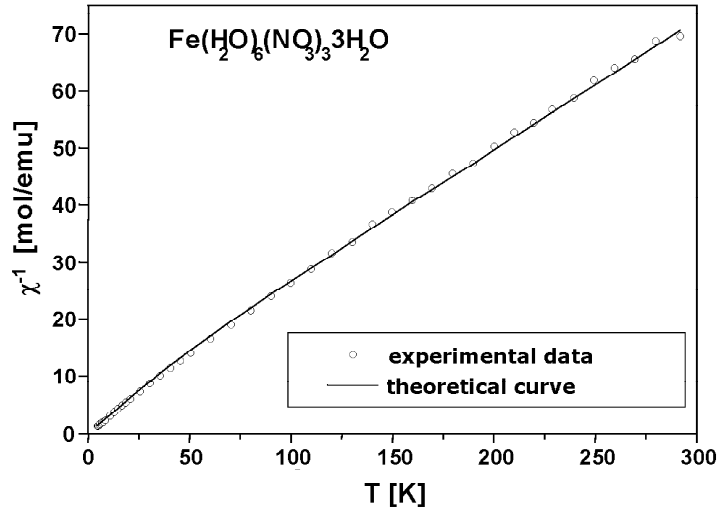


Figure 3. Inverse magnetic susceptibility for Fe(III) ions in hexaaqua-nitrate-trihydrate. Theoretical curve is obtained using equation 3 for fitting experimental data.

The experimental data for Cr(III) and Fe(III) ions in hexaaqua-nitrate-trihydrates were fitted using expressions (2) and (3) respectively. In the case of Cr(III) ions, the fitted parameters were energy level distance D , temperature independent Van-Vleck paramagnetism χ_{TIP} and Lande splitting factor g . Including the Lande splitting factor as the fitted parameter, we considered the contribution of spin-orbit interaction as a result of orbital momentum incomplete freezing. The fitted parameters in the case of Fe(III) ions were energy level distances D_1 and D_2 . In this case, we treated the Lande splitting factor as constant value. The calculated values of inverse susceptibility are shown in Figures 2 and 3. Calculated values of fitted parameters are given in Table 1.

Table 1. Calculated values of fitted parameters.

ion	calculated values of fitted parameters
Cr(III)	$D = (1.6 \pm 0.2) \text{ cm}^{-1}$; $g = 1.9 \pm 0.05$; $\chi_{TIP} = (8 \pm 2) \cdot 10^{-4} \text{ emu/mol}$
Fe(III)	$D_1 = (80 \pm 3) \text{ cm}^{-1}$; $D_2 = (12 \pm 1) \text{ cm}^{-1}$

3. Conclusion

We performed the measurements of the temperature dependence of the magnetic susceptibility of Cr(III) and Fe(III) hexaaqua-nitrate-trihydrates samples. The results of the measurements show that the samples are in a paramagnetic phase in whole measurement temperature range. The results also show deviation from the Curie-Weiss law. On the basis of identified crystal and electron structure, we calculated zero field splitting parameters in the case of both ions. In the case of Cr(III) ions, we calculated the temperature independent Van-Vleck contribution and the Lande splitting factor value.

The calculated value D for the Cr(III) ion is close to the values from literature [5]. The level with $S = \pm 1/2$ is the lowest in energy level arrangement, inverse from Figure 1(a).

The calculated Lande splitting factor value differs slightly from spin only value. This fact shows a partial orbital momentum "unfreezing" as a result of spin-orbital coupling. The calculated value for χ_{TIP} agrees with literature data [6].

The level with $S = \pm 3/2$ is the lowest in the energy level arrangement of Fe(III) ion, the level with $S = \pm 1/2$ comes next.

Obtained results show that the used model of axial distorted crystalline field is a good approximation for observed materials. It should also be mentioned that the energy level splitting is more frequently determined by spectroscopic methods, since magnetic measurements are unsatisfactorily sensitive.

Acknowledgments

This work was supported by a research grant No.2022-OI: "Physical Properties of Bulk and Nanoparticled Rare Earths and Transition Metal Based Magnetic Materials" from the Ministry of Science, Technologies and Development of the Republic of Serbia.

References

1. N. J. Hair and J. K. Beattie, *Inorg. Chem.* **14**, 245 (1977).
2. D. Lazar, B. Ribar, V. Divjaković and C. S. Meszaros, *Acta Cryst.* **C 47**, 1060 (1991).
3. M. Vučinić, A. Petrović, S. Skuban and A. Kapor, *J. Res. Phys.* **27**, 45 (1998).
4. R. L. Carlin, *J. Chem. Educ.* **43**, 521 (1966).
5. W. Low, *Paramagnetic Resonance in Solids* (Academic, New York, 1960).
6. R. L. Carlin, *Magnetic Properties of Transition Metal Compounds* (Springer-Verlag, New York, 1977).

Journal of Research in Physics

INFORMATION FOR CONTRIBUTORS

This Journal is devoted to the publication of original papers in **fundamental and applied physics**. The papers are in principle Articles, while Review Articles will be published by invitation only.

Contributors should send their manuscripts to Professor M. Škrinjar, Editor, Department of Physics, Faculty of Sciences, University of Novi Sad, Trg Dositeja Obradovića 4, 21000 Novi Sad, Serbia. (Fax #: +381-(21)-459-367; E-mail: fizika@uns.ns.ac.yu).

All manuscripts must be submitted in English. Manuscripts should be submitted in duplicate and should be typewritten and double spaced with wide margins. Only one side of each sheet should be used.

Manuscripts should consist of the title, followed by author(s) name(s) and adresse(s), abstract, key words, body of the text and the list of the references. Authors should *not* include references in Abstracts.

References must be numbered in the order in which they are referred to in the text: e.g. S. Wagner [1] or [1]. In the text, such abbreviations as Ref. [4] or Refs. [7-10] may be used.

The full references should be listed in the numerical order of citation in the text at the end of the article. Examples:

1. S. Autler and C. H. Townes, Phys. Rev. A **10**, 489 (1982). – for articles
2. E. U. Shirley, *The Theory of Molecules*, p. 399, (The University Press, Cambridge, 1954). – for books
3. C. E. Moore, "Selected Tables of Atomic Spectra", NSRDS-NBS3, Setion 5, National Bureau of Standards, Washington, DC 20025 (1975). – for reports.

Tables and figures should be sent with the paper on the separate pages. All photographs, graphs, and diagrams should be numbered consecutively. The legends should be typed on a separate page at the end of the article. The author's name, the figure number, and an indication of its proper orientation should be written on the back of each figure.

Line drawings must be submitted in camera-ready form and should be drawn in india ink on stiff white paper or printed on quality laser printer. The letters and symbols should be drawn so as to be clearly legible when reduced.

Authors are asked to suggest at least three referees who may revise their manuscript.

Page proofs will be sent to the author (or the first-mentioned author in a paper of multiple authorship) for checking. **Corrections to the proofs must be restricted to printer's errors.** Authors are particularly requested to return their corrected proofs as quickly as possible. Please note that **authors are urged to check their proofs carefully before return, since late corrections cannot be guaranteed for inclusion in the printed journal.**

The first-named author of each paper will receive 25 reprints free of charge.

Journal of Research in Physics

Volume 29 Number 1 October 2002

CONTENTS

N. Žikić-Todorović, I. Bikit, J. Slivka, M. Vesković, M. Krmar and Lj. Čonkić	<i>The $(0\nu+2\nu)$ Double Beta Decay of ^{50}Cr</i>	1
V. Babović and M. Kovačević	<i>Evaluating the Dispersion Relation of Surface Electron Plasma Waves by the Fixed-Point Method</i>	5
Ljubisav Novaković	<i>A Three-Particle Cluster and the Problem of Binding Energies</i>	13
Lj. Budinski-Petković, U. Kozmidis-Luburić and A. Mihailović	<i>Random Sequential Adsorption of Line Segments on Discrete Substrates with Quenched Impurities</i>	29
N. I. Kaymakanova, L. M. Ivanov, P. P. Branzalov and L. I. Pavlov	<i>Fiber-Optical Compressor Based on Consequent Using of Fiber of Positive and Negative Dispersion</i>	37
D. Ž. Obadović, A. Vajda, M. Stančić, K. Fodor-Csorba and L. Bata	<i>The Possibility of Phase Transition Temperature Shift in Some Ferroelectric Liquid Crystalline Mixtures</i>	45
Dušan Popov	<i>Considerations Concerning the Pseudoharmonic Oscillator Model</i>	51
D. Rodić, M. Mitrić and R. Dimitrijević	<i>Is $\text{Sm}_3\text{Fe}_5\text{O}_{12}$ Really Cubic at Room Temperature ?</i>	61
M. Pavkov, M. Pantić, M. Kirčan and T. Tošić	<i>Compensation Temperatures in Systems with Three and Four Sublattices and Superlattices</i>	67
M. Vučinić, M. Mitrić, V. Kusigerski, A. Kapor and A. Szytula	<i>Magnetic Properties of Cr(III) and Fe(III) Ions in Hexaaqua-Nitrate-Trihydrates</i>	79